

**The Canadian Hydrogen Intensity Mapping
Experiment Fast Radio Burst Project:
Monitoring the Interference Environment and
Studying the Bursting Behaviour of SGR**

1935+2154

Alice Curtin



Department of Physics

McGill University
Montréal, Québec, Canada

August 15, 2021

A thesis presented for the degree of Masters of Physics

©2021 Alice Curtin

Abstract

Fast radio bursts are highly energetic, \sim millisecond long bursts of radio emission originating from extragalactic locations. When combined with their unknown initial sky positions, their transient nature and cosmological origins makes them difficult to discover, and requires novel telescope designs and detection pipelines. In this thesis, we focus on one such telescope, the Canadian Hydrogen Intensity Mapping Experiment (CHIME) and its Fast Radio Burst (FRB) Project. Since its commissioning in 2018, CHIME/FRB has detected over two thousand FRBs, orders of magnitude more than any other telescope. Here, I present a new pipeline to characterize the radio frequency interference at CHIME/FRB. I also present a determination of upper limits on radio emission from the magnetar SGR 1935+2154, famous for producing an FRB-like burst. For seven different high-energy X-ray bursts from SGR 1935+2154, I constrain simultaneous radio emission to less than a few kJy. I also find that the FRB-like burst produced by SGR 1935+2154 is distinct from other magnetar-like bursts in its spectral properties, and its radio to X-ray flux ratio.

Abrégé

Les sursauts radio rapides (FRB pour fast radio bursts en anglais) sont des émissions radio hautement énergétiques, d'une durée de quelques millisecondes, d'origines extragalactiques. Quand combinés avec leur position dans le ciel inconnue, leur nature transoïre et leur origine les rendent difficiles à découvrir et requièrent de nouveaux types de télescopes et de nouveaux pipelines de détection. Dans cette thèse, nous allons nous concentrer sur un de ces télescopes, le Canadian Hydrogen Intensity Mapping Experiment (CHIME) et son projet de FRB. Depuis sa mise en fonction, CHIME/FRB a détecté plus de deux mille FRBs, des ordres de grandeur de plus que tout autre télescope. Ici, je démontre un nouveau pipeline pour caractériser l'interférence de fréquence radio au CHIME/FRB. Je présente la détermination d'une limite supérieure des émissions radio produites par le magnétar SGR 1935+2154, connu pour produire des sursauts radio semblables à des FRBs. Pour sept différents sursauts rayon X de haute énergie provenant du SGR 1935+2154, j'ai limité les émissions radio simultanées à moins de quelques kJy. J'ai aussi découvert que les émissions ressemblant à des FRBs produites par SGR 1935+2154, sont

distinctes des autres sursauts typiques provenant de magnétars par leur propriétés spectrales et leur rapport radio/rayon X.

Acknowledgements

Before anyone else, I need to thank my advisor Vicky for constantly encouraging me to follow my interests, answering all of my trivial questions, and being a fantastic role model. Three years ago, at the AAS conference, I ran into Vicky at 10pm on the streets of Seattle. She bought me a milkshake and I talked her ear off about my work (which was totally irrelevant to CHIME/FRB). I am so thankful she took a chance on me after that. This work would also not be possible without the entire CHIME/FRB collaboration. With little to no knowledge of telescope fundamentals prior to joining the team, I would not be where I am without the many people who took the time to teach me even the most basic material (most of which I could have probably found online). I especially want to thank Shiny for his help and patience as I undertook my first large-scale technical project. This MSc would not have been possible without him.

I want to thank my friends in the US for staying in touch and providing remote support during the closure of the US-Canada border, along with my friends in Canada who listened, related, and provided support throughout my ups and downs. I would especially like to

thank Bridget and Marcus for their mentorship within the CHIME/FRB collaboration and for their friendship (in the kitchen, on the trails of Mont Royal, and in the MSI).

Lastly, I want to thank my parents and my grandmother. My dad stayed up-to-date on all popular science articles in order to send them to me every week. My grandmother constantly asked me “How is the telescope doing?” and my mom was my reliable sounding board for good (and bad) ideas.

Contributions

The construction and maintenance of the CHIME telescope and the CHIME/FRB software, described in detail in Chapter 2, would not be possible without the work of numerous different members. While a current list of all CHIME and CHIME/FRB members is not readily accessible, the collaborating institutions can be found on CHIME’s website, chime-experiment.ca, and the majority of the CHIME/FRB software referenced in Chapter 2 was developed by the contributing authors of CHIME/FRB Collaboration (2018) [1]. Additionally, most (although not all) current CHIME/FRB members can be found in the author list of CHIME/FRB Collaboration (2021) [2].

Chapters 3 and 4 largely contain original work of the author. The majority of the *rfi-scout* pipeline was written by the author except for a portion which was written by Shiny Brar. Some of the metrics used in Chapter 3 were also queried using software written by Dustin Lang. The metrics that are queried in Chapter 3 are generated through software written by Kendrick Smith and Masoud Rafiei-Ravandi.

In Chapter 4, while the pipeline is the original work of the author, many components of

the pipeline are not. The data used to map the primary beam model was supplied by Dallas Wolf, and the formed beam model has largely been the work of Paul Scholz and Cherry Ng. The system sensitivity metrics were generated by Pragya Chawla, and the fluxes and fluences of the FRBs were calculated using a pipeline written by Chitrang Patel and Bridget Anderson.

Contents

Abstract	i
Abrégé	ii
1 Pulsars, Magnetars, and Fast Radio Bursts	1
1.1 Pulsars	2
1.1.1 Discovery and Radio Emission	2
1.1.2 Observational Properties	3
1.1.3 Pulsar as Tools	6
1.2 Magnetars	6
1.2.1 Discovery	6
1.2.2 Persistent Emission Magnetars	8
1.2.3 Transient Emission Magnetars	9
1.2.4 Lower Frequency Emission	11
1.2.5 Additional Details	12
1.3 Fast Radio Bursts	12

1.3.1	What are they?	12
1.3.2	Large-scale View of the Population	16
1.3.3	A Few Specific FRBs	23
1.3.4	Possible Progenitor Models	25
2	The Canadian Hydrogen Intensity Mapping Experiment	27
2.1	The Telescope	27
2.2	The CHIME/FRB Backend	32
2.2.1	L1	32
2.2.2	L2/L3	36
2.2.3	L4	37
3	The <i>rfi-scout</i> Pipeline	38
3.1	Radio Frequency Interference at Radio Telescopes	38
3.1.1	Challenge of Radio Frequency Interference	38
3.1.2	Radio Frequency Interference at CHIME	40
3.1.3	Previous CHIME/FRB RFI Pipeline	47
3.2	Pipeline: <i>rfi-scout</i>	50
3.2.1	Objectives	50
3.2.2	Structure	51
3.2.3	Benefits Achieved by <i>rfi-scout</i>	55

3.3	Future Work for <i>rfi-scout</i>	56
3.3.1	Remaining Work	56
3.3.2	Areas for Improvement	57
4	Radio Limits for SGR 1935+2154	63
4.1	Introduction to SGR 1935+2154	63
4.2	Initial CHIME/FRB Detection of SGR 1935+2154	65
4.3	Non-detections by CHIME/FRB of SGR 1935+2154 Bursts Detected by <i>Swift</i> /BAT	67
4.3.1	Upper Limits on Radio Emission	67
4.3.2	Analysis of High-Energy Emission	73
4.3.3	Comparison of Bursts	80
4.4	Non-detections by CHIME/FRB of SGR 1935+2154 Bursts Detected by <i>Fermi</i> /GBM	81
4.4.1	<i>Fermi</i> /GBM Telescope	81
4.4.2	Searching the CHIME/FRB Database for Radio Counterparts	83
4.4.3	Upper Limits on Radio Emission	86
4.5	Summarizing Non-Detections by CHIME/FRB of X-ray and High-energy SGR 1935+2154 Bursts	89
5	Conclusion	92

A	Testing the <i>rft-scout</i> Pipeline	94
A.1	Querying from L1	94
A.2	Initial Data Storage	96
A.3	Downsampling in Frequency	97
A.4	Downsampling Across E-W columns	98
A.5	Polynomial Fit	100
A.6	Final Data Storage	105
A.7	Computational Cost of <i>rft-scout</i>	105

List of Figures

1.1	Example of Emission from a Pulsar	5
1.2	First Detected FRB	13
1.3	Comparing the Radio Luminosities of Different Astrophysical Objects	15
1.4	Example of Downward Drifting Emission from an FRB	19
2.1	Photograph of CHIME	28
2.2	Approximate Mapping of CHIME/FRB N-S Beams to Declination	30
2.3	Schematic of the CHIME Pipeline	31
2.4	Schematic of the CHIME/FRB Backend	33
3.1	CHIME/FRB RFI as a Function of Frequency	42
3.2	CHIME/FRB RFI as a Function of N-S Beam	44
3.3	CHIME/FRB RFI as a Function of Both Beam and Frequency	45
3.4	Comparing Different L1 RFI Sampling Rates	49
3.5	Flowchart of the <i>rfi-scout</i> Pipeline	52

3.6	Averaging RFI Metrics Over the E-W CHIME Cylinders	58
3.7	Fitting a Polynomial to CHIME/FRB's RFI Metrics for N-S Beam 3	59
3.8	Fitting a Polynomial to CHIME/FRB's RFI Metrics for N-S Beam 108	60
3.9	Fitting a Polynomial to CHIME/FRB's RFI as a Function of All N-S Beams	61
3.10	Fitting a Polynomial to CHIME/FRB's RFI as a Function of Select N-S Beams	62
4.1	Dynamic Spectra and Band-averaged Time-Series of the SGR 1935+2154 Burst Detected by CHIME/FRB	66
4.2	BAT's FOV During a Burst From SGR 1925+2154 at UTC 00:08:58 on 5 November 2019	75
4.3	BAT's FOV During a Burst From SGR 1925+2154 at UTC 01:36:25 on 5 November 2019	76
4.4	X-ray Burst from SGR 1935+2154 Detected by <i>Swift</i> /BAT on 5 November 2019 at UTC 00:08:58	78
4.5	X-ray burst from SGR 1935+2154 detected by <i>Swift</i> /BAT on 5 November 2019 at UTC 01:36:25	79
4.6	CHIME/FRB Events that are Temporally Close to the <i>Fermi</i> /GBM Detections of SGR 1935+2154	85
A.1	Comparing the L1 RFI Masking on Different Days	103
A.2	Final Data Format for RFI metrics	104

List of Tables

3.1	Data Reduction Achieved by <i>rfi-scout</i>	56
4.1	Parameters for Upper Limits on Radio Emission for SGR 1935+2154 Burst Detected by <i>Swift</i> /BAT	69
4.2	Parameters for High-Energy Emission for SGR 1935+2154 Bursts Detected by <i>Swift</i> /BAT	77
4.3	High-energy and Radio Fluxes for the <i>Swift</i> /BAT SGR 1935+2154 bursts . .	81
4.4	Parameters for Upper Limits on Radio Emission for SGR 1935+2154 Bursts Detected by <i>Fermi</i> /GBM	87
A.1	Data Sets for Testing <i>rfi-scout</i>	95
A.2	Data Reduction Achieved through E-W Downsampling of RFI Metrics . . .	99

List of Acronyms

BB	Blackbody.
CCSNe	Core-Collapse Supernova Explosion.
CHIME	Canadian Hydrogen Intensity Mapping Experiment.
DM	Dispersion Measure.
FOV	Field of View.
FRB	Fast Radio Burst.
LOS	Line of Sight.
PL	Power-Law.
RFI	Radio Frequency Interference.
S/N	Signal to Noise.
SNR	Supernova Remnant.

Chapter 1

Pulsars, Magnetars, and Fast Radio

Bursts

In 1967, the first pulsar was detected by accident [3]. Ten years later, a highly magnetized neutron star, now known as a magnetar, was discovered [4], [5], [6]. Thirty years after that, a fast radio burst (FRB) was found in archival pulsar data [7]. The three share many similarities – a magnetar emitted an FRB-like burst (e.g. CHIME/FRB Collaboration (2020) [8]), pulsars have emitted magnetar-like bursts (e.g. Archibald et al. (2016) [9]), and the same instruments can be used to detect all three. Pulsars, magnetars, and FRBs are relevant when discussing the Canadian Hydrogen Intensity Mapping Experiment (CHIME)/FRB Project, which is the main topic of this thesis.

1.1 Pulsars

1.1.1 Discovery and Radio Emission

The first pulsar was detected, by accident, in 1967 by Jocelyn Bell. A graduate student at the time, Bell had been using the Interplanetary Scintillation Array to study radio emission from quasars. She found several mysterious signals in her data, which her research group called the “Little Green Men.” She spent the next year studying the objects, with a publication in *Nature* that suggested they might be neutron stars or white dwarfs [3]. The “Little Green Men” are now known as pulsars, a class of rotating neutron stars. While pulsars can emit radiation across the entire electromagnetic spectrum (e.g. see Kaspi, Roberts, & Harding (2016) [10] for a discussion of their X-ray emission and Caraveo & Patrizia (2014) [11] for a discussion of their gamma-ray emission) they are the most well-known for their radio emission. To date, there are 2872 pulsars listed in the Australia Telescope National Facility (ATNF) Pulsar Catalogue [12]. Some of the most well known facilities for detecting these pulsars include the Arecibo Observatory in Puerto Rico¹, the Parkes Observatory in Australia², the Green Bank Telescope in West Virginia³, the Jodrell Bank Observatory in England⁴, and recently the Five Hundred Meter Aperture Spherical Telescope in China⁵.

Pulsars are created in supernovae. They are well known for having predictable radio

¹See www.naic.edu/ao/ for details on the Arecibo Observatory.

²See this [link](#) for details on the Parkes Observatory.

³See greenbankobservatory.org for details on the Green Bank Telescope.

⁴See this [link](#) for details on the Jodrell Bank Observatory.

⁵See fast.bao.ac.cn for details on the Five Hundred Meter Aperture Spherical Telescope.

pulses as they spin down at very steady rates with the spin down a result of magnetic dipole braking. Typically, isolated pulsars have periods of 0.1 to 10 seconds, spin down rates of 10^{-17} to 10^{-12} s s⁻¹, and average surface dipolar magnetic field strengths of 10^{11} to 10^{13} G [13].

1.1.2 Observational Properties

After the pulse is emitted by the pulsar, it travels through many media before reaching earth. This propagation affects the observed characteristics of the pulse with the most obvious effect being the dispersion of the pulse. Interactions between the radio emission and the free electrons in the different media will delay the radiation. This delay depends on frequency, with lower frequencies showing greater delays, e.g.

$$\Delta t \propto DM(v_1^{-2} - v_2^{-2}) \quad (1.1)$$

where Δt is the relative time delay between two frequencies v_1 and v_2 , and DM is the dispersion measure in units of pc cm⁻³. The DM can also be represented as:

$$DM = \int_0^d n_e dl \quad (1.2)$$

where d is the distance to the pulsar, n_e is the free electron density, and the integral is over the path length l . The observed result of the delay Δt is a pulse that sweeps through

the frequency-time plane as shown in Fig. 1.1. Besides delaying the signal, the interstellar medium (ISM) can also scatter a pulse. Scattering, which is dependent on the frequency of the pulse, will asymmetrically broaden a pulse⁶. The ISM is also responsible for pulse scintillation (see Narayan (1992) [15] for details on this).

As the pulsar emission travels through different magneto-ionic material, it will also undergo Faraday rotation in which the polarization angle of the emission rotates at a rate proportional to the strength of the magnetic fields parallel to the pulsar's line of sight (LOS). The rotation measure (RM) of the pulsar quantifies the Faraday rotation of the linear polarization angle, χ , as a function of wavelength, λ ,

$$\Delta\chi = RM\lambda^2. \quad (1.3)$$

The RM is also proportional to the integrated product of the electron density, n_e , and the LOS component of the magnetic field, B ,

$$RM = 0.81 \int_0^d n_e \mathbf{B} \cdot d\mathbf{l}. \quad (1.4)$$

Thus, measuring the frequency dependence of the linear polarization position angle is useful for studying the LOS magnetic field.

⁶Different models for the ISM predict different scattering relations. One such example is that of Kolmogorov inhomogeneities where $\tau_{SC} \propto \nu^{-4.4}$ [14].

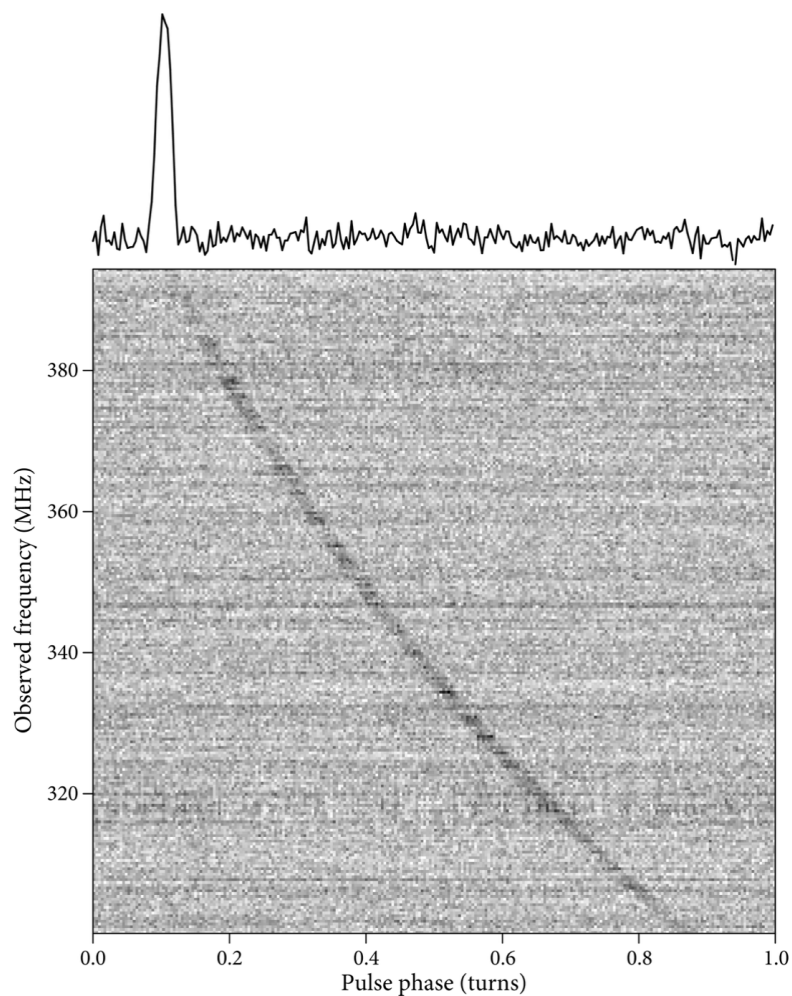


Figure 1.1: Example of radio emission from the pulsar J1800+5034. In the bottom panel, the initial observed pulse (before de-dispersion) is shown as a function of frequency and phase. In the top panel, the pulse has been de-dispersed and summed over all frequency channels. Figure courtesy of Condon and Ransom (2016) [16].

1.1.3 Pulsar as Tools

The LOS integrated pulsar properties can be used to study both the local environment of the pulsar and the ISM. For example, pulsar RMs have been used to map the magnetic field of the Milky Way (e.g. Han et al. (2018) [17], Weisberg et al. (2004) [18]), and their DMs were an integral part of the latest Milky Way electron density model (e.g. Yao, Manchester, & Wang (2017) [19]). Additionally, the timing of pulsars in and of itself is also highly valuable. PSR B1913+16, which is in a binary system with another neutron star, provided the first evidence for the theory of gravitational waves [20]. In the last century, pulsar timing arrays have also set out to measure a background of gravitational waves by timing millisecond pulsars [21].

1.2 Magnetars

1.2.1 Discovery

While all pulsars are neutron stars, not all neutron stars are necessarily pulsars. In 1979, repeating soft gamma-ray and hard X-ray emission was detected from two different sources, with their pulsating nature along with their energetics pointing towards a neutron star origin [4], [5], [6]. These ended up being the first examples of a class of neutron stars known as magnetars. Magnetars are similar to pulsars (and are most likely an extension of the same class as discussed below in Section 1.2.4), but the calculated energy release during the

X-ray and soft gamma-ray bursts is significantly larger than the available rotational energy of these sources. Magnetars also have considerably longer periods than pulsars, with the shortest known magnetar period ~ 2 seconds and the longest ~ 12 seconds [22], [23]. When combined with their measured spin-down rates, these long periods imply average surface magnetic field strengths of $\sim 10^{14}$ G, significantly larger than that of an average pulsar. The characteristic age⁷ for a magnetar is also $\sim 10^3$ to 10^5 years, while pulsars typically have characteristic ages $\sim 10^7$ years [24], [13]. Magnetars' characteristic ages, combined with their preferential locations in the Galactic plane and their associations with supernova remnants (SNR), lends strong evidence to magnetars being young neutron stars [25].

In 1992, Duncan and Thompson derived the first model for magnetars in which magnetic, rather than rotational, energy powers the magnetar [26]. More specifically, the magnetar is fueled by strong internal magnetic fields which arise through dynamo in the early convective stage of the source. These fields are unstable to decay, which can stress the crust and cause it to shift. As a magnetar's magnetic field lines are tied to the crust, this then twists the magnetic field lines in the magnetosphere. The reconfiguration and decay of these twisting fields, along with heating of the crust, leads to both the persistent emission seen from magnetars along with the sudden bursts.

Initially, there were two classes for objects which we now classify as magnetars: soft gamma-ray repeaters (SGRs) and anomalous X-ray pulsars (AXPs). While AXPs had softer

⁷The characteristic age is defined as $P/2\dot{P}$.

X-ray spectra, Thompson and Duncan (1996) predicted that AXPs and SGRs might both be magnetars [27]. This was confirmed in 2002 by the detection of hard X-ray bursts from AXPs [28]. Now magnetars are typically classified as: 1) persistent emission magnetars and 2) transient emission magnetars.

1.2.2 Persistent Emission Magnetars

Persistent emission magnetars have high, quiescent pulsed X-ray luminosities $> 10^{33}$ erg s $^{-1}$. However, persistent emission magnetars can also exhibit transient behaviour (see Section 1.2.3 for details on transient behaviour). Two such examples of persistent emission magnetars are 1E 2259+586, which underwent a large outburst in June 2002 (see Kaspi et al. (2003) [29]), and 4U 0142+61, which had two outbursts in 2016 (see Archibald et al. (2017) [30]).

The persistent soft X-ray emission can typically be modelled using an absorbed blackbody (BB) plus a power-law (PL) with BB temperatures of ~ 0.3 to 0.5 keV and PL photon indices of ~ -2 to -4 [25]. The non-thermal PL tends to dominate above temperatures of 3 to 4 keV with a spectral turn-over around 10 keV (e.g. see Figure 5 of Kaspi & Beloborodov (2017) [25]). Above 10 keV, the spectra of certain persistent emission magnetars turns up, with an increase in the number of counts at these higher energies [25].

The persistent soft X-ray emission seen in these magnetars is most probably generated by a combination of magnetospheric and surface effects. The thermal component likely arises from heating of the neutron star surface through either return currents from the

magnetosphere, a heat source within the crust itself, or the transfer of heat from within the core to the crust [25]. The thermal emission is then distorted in the atmosphere and magnetosphere, leading to the non-thermal components in the spectra. This distortion likely arises through resonant cyclotron scattering (e.g. see Lyutikov & Gavriil (2006) [31], Rea et al. (2007a) [32], Rea et al. (2007b) [33]). While the harder emission (that above ~ 10 keV) has proven more difficult to model, it is likely due to currents with the magnetar's magnetosphere [34].

1.2.3 Transient Emission Magnetars

Some magnetars (such as XTE J1810–197 and SGR J1745–2900) do not show strong quiescent emission, with persistent quiescent luminosities $< 10^{33}$ erg s $^{-1}$ [25]. These magnetars may actually be the most common amongst the population, but with lower persistent luminosities they are harder to detect. These magnetars often undergo periods of bursting behaviour which can be broken down into three categories: 1) bursts, 2) outbursts, and 3) flares.

Bursts are the most common of the three. They consist of emission on short, millisecond to second long timescales. They exhibit a range of luminosities from 10^{36} to 10^{43} erg s $^{-1}$ and have fairly steep fluence PLs of -1.6 to -1.8 . The bursts typically have a short, steep rise followed by a slower decay and some also have extended tails of emission in which there is an increase in the pulsed flux. Bursts are most likely generated by rapid re-configurations of a

twisted magnetic field within the magnetosphere [34]. There are several triggers that might provide the stress that causes the reconfiguration, including but not limited to 1. an unstable field in the core that eventually injects Alfvén pulses into the magnetosphere, 2. the decay of the field in the core which stresses the crust, causing it to rupture and inject Alfvén pulses, or 3. a stress built up in the magnetosphere e.g. spontaneous magnetic re-connection [34].

The second type of transient behaviour is an outburst. Outbursts tend to last for weeks to months, with an increase in the persistent pulsed flux by factors of 10 to 1000 [25]. For a transient emission magnetar, this factor is typically > 100 while for persistent emission magnetars it is < 100 [25]. Outbursts are accompanied by many short duration bursts, with the spectra and pulse characteristics also changing. Outbursts are often seen in conjunction with glitches and anti-glitches. Glitches (or anti-glitches) consist of sudden spin-ups (or spin-downs) in the pulsar’s period. They are then followed by a period of recovery in which the pulsar’s period returns to normal. Glitches are often associated with crustal deformations and are most commonly seen in magnetars and young radio pulsars [34], [13].

During the beginning of an outburst, the spectrum of the magnetar suddenly hardens. It then softens over the remainder of the outburst. Outbursts are most often modelled using a BB plus PL, with the BB temperature and PL steepness increasing by factors of roughly two at the onset of the outburst [25]. Outbursts are likely related to, and fueled by, re-configurations of a twisted magnetosphere, with larger twists leading to higher luminosities and harder spectra [25]. These re-configurations may be fueled by the crustal deformations

causing the glitches and anti-glitches.

The last type of transient behaviour in magnetars is flares. Flares are extraordinarily luminous with peak luminosities of 10^{44} to 10^{47} erg s⁻¹ and peak energies in the soft gamma-ray band. The peak of a magnetar flare is followed by a tail of decaying, pulsed emission (see Hurley et al. (2005) [35] for more details). Because of their enormous energy, flares must be caused by a major magnetic field reconfiguration and energy deposition, with the tail likely powered by a trapped fireball within the magnetosphere [25]. Only three Galactic magnetars have undergone giant flares: SGR 1900+14, SGR 1806–20, and SGR 0526–66 [36], [37], [4].

1.2.4 Lower Frequency Emission

While magnetars are most commonly observed in the X-ray and gamma-ray band, a handful have also been detected in the optical, IR, and radio bands. The radio emission has been detected in six magnetars, with all emission detected during or after an outburst. The detection of radio emission from magnetars opens the question of whether magnetars are related to pulsars, especially pulsars with high magnetic field strengths. This question has further been fueled by the detection of two magnetar-like outbursts from pulsars J1846–0258 and J1119–6127 [25]. Both J1846–0258 and J1119–6127 are high-B pulsars with magnetic fields of 4.9×10^{14} G and 4.1×10^{14} G, respectively [25]. PSR J1846–0258 has yet to be detected at radio wavelengths, but PSR J1119–6127 is otherwise a typical radio emitting pulsar [38]. Similar to pulsars, the emission from magnetars can also be highly linearly

polarized. However, the spectra of magnetars is considerably flatter than that of pulsars.

1.2.5 Additional Details

Since their initial discovery in 1979, ~ 31 magnetars have been discovered. The first magnetar catalog (Olausen & Kaspi (2014) [39]) was compiled in 2007, and all but one of the 31 magnetars (SGR J1555.2–5402) can be found at the online McGill Magnetar Catalog⁸ (see Palmer et al. (2021) [40] for details on the initial detection of the 31st magnetar SGR J1555.2–5402). For further details on magnetars, we direct the reader to the magnetar catalog (Olausen & Kaspi (2014) [39]) or the most recent magnetar review (Kaspi & Beloborodov (2017) [25]).

1.3 Fast Radio Bursts

1.3.1 What are they?

In 2007, when combing through archival data from a pulsar survey of the Magellanic clouds, a group of astronomers came across a rather surprising discovery: a burst similar to a pulsar, but whose properties suggested a cosmological origin [7]. The DM of the burst (375 pc cm^{-3}) was significantly larger than that predicted by the DM models for our own Galaxy along this LOS (25 pc cm^{-3}). It was also larger than the DMs of the handful of pulsars in the

⁸The McGill Magnetar Catalog can be found [here](#).

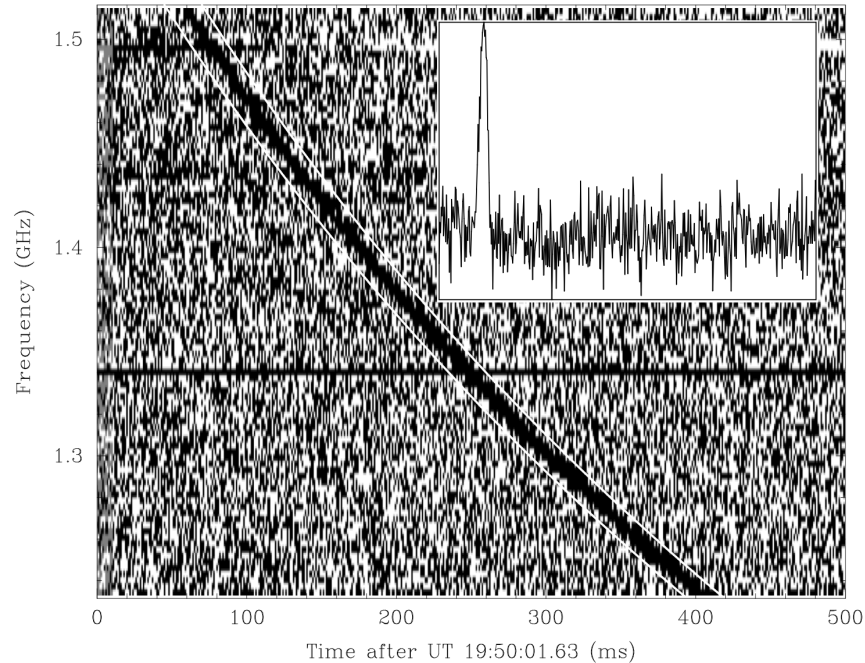


Figure 1.2: Pulse from the first FRB known as the “Lorimer Burst”. In the main panel, the original pulse (prior to de-dispersion) is shown as a function of frequency and time. In the smaller, top right panel, the integrated (over all frequencies) and de-dispersed pulse is shown. Figure courtesy of Lorimer et al. (2007) [7].

Magellanic clouds. This burst, known as the “Lorimer Burst,” was the first fast radio burst (FRB) discovered, and can be seen in Fig. 1.2.

Since their discovery in 2007, over 750 FRBs have been discovered and published. They are fast (on the order of milliseconds), highly energetic bursts of radio emission originating from extragalactic origins. An FRB-like burst was also detected in our own galaxy from the well-known magnetar SGR 1935+2154, albeit one to two orders of magnitude less energetic than that of typical FRBs [8]. FRBs have been detected in spiral galaxies (e.g. Mannings

et al. (2021) [41]), dwarf galaxies (e.g. Tendulkar et al. (2017) [42]), and recently in the neighbouring spiral galaxy M81 (e.g. Bhardwaj et al. (2021) [43], Kirsten et al. (2021) [44]). While the original discovery consisted of a single burst (herein called a “one-off” FRB), some FRBs have been shown to repeat, with two repeating periodically [45], [46], [47].

FRBs are exciting for several reasons. In and of themselves, they are an extremely energetic phenomenon with spectral luminosities $\sim 10^{32}$ erg s⁻¹ Hz⁻¹ (e.g. see Fig. 1.3) which cannot be explained by the typical models for pulsars or magnetars. Most models for FRBs still involve neutron stars but invoke new physical processes and mechanisms for producing these energetic events e.g. bunches of particles moving along curved magnetic field lines, magnetized shock waves, a stream of particles combing through the magnetosphere of the neutron star, an asteroid belt surrounding a pulsar, or an expanding fireball [48], [49], [50], [51], [52]. Outside of being a new physical phenomena, FRBs are also a new probe for studying cosmological parameters and questions such as the Hubble constant (e.g. Hagstotz, Reischke, & Lilow (2021) [53]), the missing baryon problem (e.g. Macquart et al. (2020) [54]), the epoch of reionization (e.g. Pagano & Fronenberg (2021) [55]), and Dark Matter (e.g. Muñoz et al. (2016) [56]). Since some properties of FRBs (e.g. DM, RM, scattering) are LOS-integrated, we can also use them to study Galactic and extragalactic environments e.g. mapping the halo of the Milky Way using their DMs and studying local magnetic fields using their RMs.

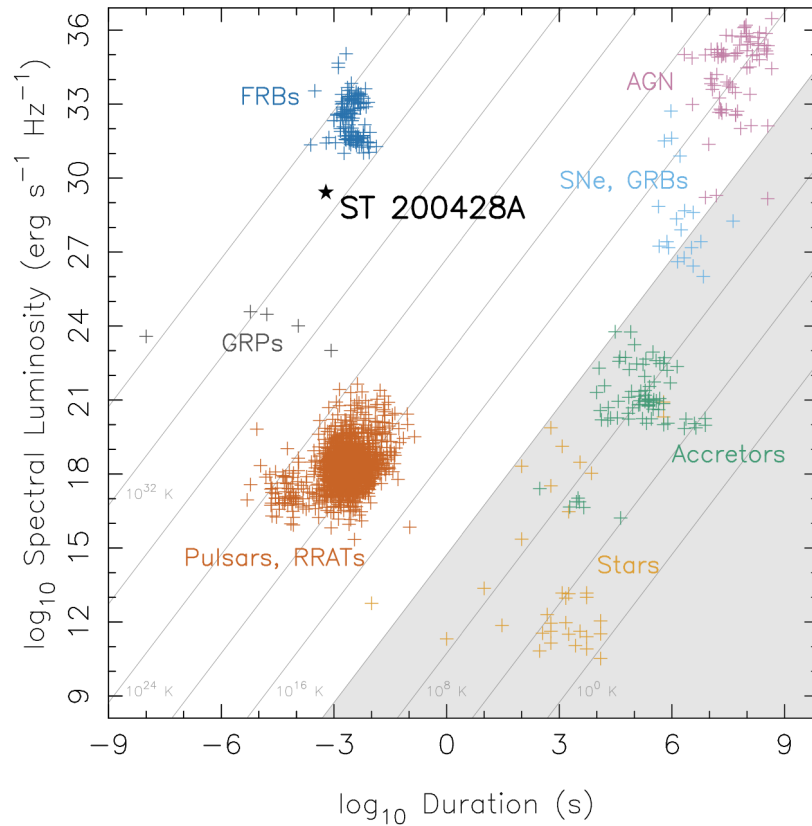


Figure 1.3: Spectral luminosity as a function of pulse duration for FRBs, pulsars, giant radio pulses (GRPs), active galactic nuclei (AGN), gamma-ray bursts (GRBs), supernova explosion (SNe), accretors, and stars. FRBs do not occupy the same regime as any other transient phenomena. A burst from the Galactic magnetar SGR 1935+2154 is indicated with a black star and labelled as 200428A. Figure courtesy of Bochenek et al. (2020) [57].

1.3.2 Large-scale View of the Population

Since their initial discovery in 2007, over 750 FRBs have been published. The first 119 of these FRBs (those up to July 2020) are available through FRBCAT, the first FRB catalog [58]. Recently, the CHIME/FRB collaboration released the first large (500+) FRB catalog with 536 FRBs detected between 25 July 2018 and 1 July 2019 [2]. Of the 536, 62 bursts are from 19 previously detected CHIME/FRB repeating FRBs (see CHIME/FRB Collaboration (2019a) [59], CHIME/FRB Collaboration (2019b) [60], and Fonseca et al. (2020) [61] for further details on these repeaters). The full set of > 750 FRBs detected both by CHIME/FRB and other collaborations is available through the Transient Name Server (TNS)⁹.

It is hard to perform population studies of FRBs using different instruments, as each instrument suffers from its own detection biases. Unless each bias can be corrected for, one cannot distinguish an instrumental bias from an intrinsic characteristic of the population. Thus, to summarize what is known about the FRB population, we focus primarily on the results of the first CHIME/FRB catalog and the four accompanying papers on the Galactic latitude dependence of the sample (Joseph et al. (2021) [62]), the morphology of the bursts (Pleunis et al. (2021) [63]), the cross-correlation of the sample with galaxy surveys (Rafiei-Ravandi et al. (2021) [64]), and the DMs and scattering times of the FRBs in the context of other transient phenomena (Chawla et al. (2021) [65]).

⁹The TNS can be found at www.wis-tns.org.

To first order, repeaters and non-repeaters detected by CHIME/FRB suffer from similar selection biases, allowing for a comparison of the two. This is important for determining whether non-repeating FRBs (“one-offs”) and repeaters are actually two distinct classes of FRBs. Within the first CHIME/FRB catalog, repeaters and “one-off” bursts are indistinguishable in their spatial (right ascension and declination) extents [2]. Repeaters and “one-offs” are also indistinguishable in their DM distributions, scattering distributions, and signal to noise (S/N) distributions within the first CHIME/FRB catalog. However, the burst widths along with the bandwidths are statistically different between the two. This is explored in detail by Pleunis et al. (2021) [63] who perform a large scale study of the morphology of the first CHIME/FRB catalog. They find that bursts from repeating sources have larger widths but smaller bandwidths. This could be due to beaming effects, where there is a correlation between the burst width and the repetition rate (see Connor, Miller, & Gardenier (2020) [66]), or due to propagation effects such as plasma lensing (e.g. see Cordes et al. (2017) [67]). However, the difference might also be intrinsic, with different progenitors or different emission mechanisms responsible for the differing features.

In addition to studying the different width and bandwidth distributions, Pleunis et al. (2021) [63] also creates a schema for classifying bursts based on their morphology. There are four possible categories for FRB burst morphologies: 1. simple (one component) broadband bursts ($\sim 30\%$ of the bursts), 2. simple, narrowband bursts ($\sim 30\%$ of the bursts), 3. temporally complex (multiple components) bursts ($\sim 5\%$ of the bursts), and 4. downward

drifting (type 3 bursts for which the components drift downward in frequency with time e.g. the burst in Fig. 1.4) bursts ($\sim 5\%$ of the bursts). “One-off” FRB bursts tend to be simpler bursts exhibiting type one structure while repeating FRBs often have downward drifting bursts. This might point to intrinsic differences between the two populations, although systematic effects can also make one type of burst appear as another type e.g. a type two burst might actually be a type three burst, but the temporal resolution might not be fine enough to distinguish the sub-bursts.

To study the intrinsic properties of the entire FRB population within the first CHIME/FRB catalog, the CHIME/FRB collaboration uses an injection system in which fake bursts are injected into the CHIME/FRB detection pipeline to quantify the pipeline’s selection effects. After doing so, the DM distribution is well fit by a log-normal function with a peak at 500 pc cm^{-3} and a tail that extends to $\sim 3000 \text{ pc cm}^{-3}$. Maybe this is the true DM distribution of FRBs at CHIME/FRB’s sensitivity, or there is a correlation between scattering and DM, or fluence and DM that skews the distribution. The injections do, however, clearly show that CHIME/FRB is biased against bursts with large widths and those with large scattering tails. While most bursts probably still have relatively modest widths of $< 10 \text{ ms}$, there is likely a large population of bursts with scattering times $> 100 \text{ ms}$.

Injections also allow the CHIME/FRB collaboration to model the fluence distribution of FRBs. They calculate a spectral index for the fluence distribution of -1.40 ± 0.11 , consistent

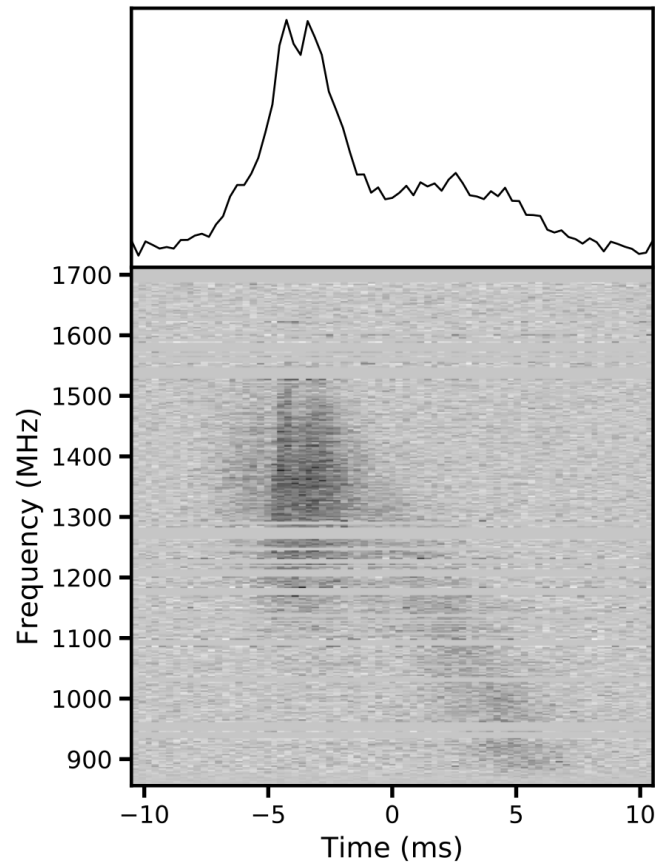


Figure 1.4: An example of a downward drifting burst from FRB 20121102A after applying de-dispersion. The top panel shows the pulse as function of time after integrating over all frequencies. The bottom panel shows the frequency dependence and the downward drifting (in frequency) nature of the emission. Figure courtesy of Caleb et al. (2020) [68].

with the predicted value of -1.5 for a constant-density, Euclidean space. While most FRB surveys' fluence distributions have been consistent with the Euclidean prediction, some have not, although it is unclear if this is systematic or astrophysical. We refer the reader to Section 7.4 of CHIME/FRB Collaboration (2021) [2] for a detailed discussion of this.

Lastly, the CHIME/FRB collaboration calculates the rate of FRBs per day, finding a rate of $818 \pm 64^{+220}_{-200}$ FRBs per sky per day at 600 MHz. To compare this rate with those determined for other surveys, they scale the rate based on a given survey's observing frequency. However, the spectral index used for this scaling is still not well constrained so they assume a flat spectral index. Then, the rates are assumed to be equivalent at the varying observing frequencies. The rate inferred from CHIME/FRB is consistent with that from the Green Bank North Celestial Cap Survey (see Parent et al. (2020) [69]), that from the Parkes Radio Telescope (see Bhandari et al. (2018) [70]), and (within 3σ) that from the Australian Square Kilometre Array Pathfinder (ASKAP) (see Shannon et al. (2018) [71]). It is not consistent with the rate inferred from the UTMOST project at the Molonglo Observatory Synthesis Telescope (see Farah et al. (2019) [72]), although this may just be a result of unaccounted for biases due to the Molonglo Telescope's complex beam structure. The two telescopes also have different bandwidths which might account for the discrepancy in the rates.

While the sky position uncertainties for CHIME/FRB events are too large to localize FRBs to specific host galaxies, Rafiei-Ravandi et al. (2021) [64] performs a large-scale cross-correlation between the CHIME/FRB sample of bursts and five different galaxy catalogs in

the redshift range of $0.3 \lesssim z \lesssim 0.5$. They find a statistically significant cross-correlation with three of the surveys, with a large fraction (if not the entire fraction) of FRBs associated with the dark matter halos from these galaxy surveys. Additionally, they note there may be a population of FRBs with very large ($\sim 400 \text{ pc cm}^{-3}$) host DMs.

The localizations of the FRBs can, however, be used to investigate a possible Galactic latitude dependence of FRBs. This dependence was first suggested by Petroff et al. (2014) [73] and Champion et al. (2016) [74]. However, the FRB sample sizes for these two analyses were small. Using the entire CHIME/FRB first catalog, Josephy et al. (2021) [62] find no dependence on Galactic latitude for the sky positions of FRBs.

In addition to the first CHIME/FRB catalog, there have been numerous other FRB discoveries, although none of the same magnitude. Possibly the second largest discovery is one by ASKAP in which they present 20 “one-off” FRBs [71]. In addition to ASKAP¹⁰, the UTMOST telescope¹¹, Parkes Radio Telescope, Very Large Array¹², Green Bank Telescope, Apertif system at the Westerbork Synthesis Radio Telescope¹³, and Five-hundred-meter Aperture Spherical radio Telescope (just to name a few) have also detected FRBs. Some of the FRBs in these discoveries have been followed up by high-energy facilities, although no high-energy emission has been observed yet [72], [70].

A select number of FRBs have been localized to specific host galaxies. Most recently,

¹⁰See this [link](#) for details on ASKAP.

¹¹See astronomy.swin.edu.au/research/utmost/ for details on the UTMOST telescope.

¹²See public.nrao.edu/telescopes/vla/ for details on the Very Large Array.

¹³See astron.nl/telescopes/wsrt-apertif/ for details on the Apertif system.

Mannings et al. (2021) [41] presented a detailed analysis of eight FRB host galaxies. They found that five of the eight FRB hosts are spiral galaxies, and while the FRBs are located within the spiral arms of these galaxies, they are not actually located at the brightest positions within the spiral arms. Additionally, only two of the eight FRBs lie in areas of high star formation, which is surprising as young magnetars (a leading progenitor possibility for FRBs) are expected to exist in high star formation regions. It is interesting to compare these observational results to the findings of Chawla et al. (2021) [65], who simulate the DM and scattering times of FRBs in different environments and compare these results to the first CHIME/FRB catalog. Chawla et al. (2021) [65] favours models in which FRBs, unlike pulsars and magnetars, do not lie in the spiral arms of galaxies.

The authors of Mannings et al. (2021) [41] also compare several FRB host galaxy properties with those predicted for six different transient phenomena: long duration gamma-ray bursts (LGRBs) short-duration gamma-ray bursts (SGRBs), Ca-rich transients, Type Ia supernova (Type Ia SNe), core-collapse supernova explosions (CCSNe) and super-luminous supernova explosions (SLSNe). The only two phenomena fully consistent with their sample of FRB host galaxies are Type Ia SNe and CCSNe. This agrees with previous work that finds FRBs are consistent with CCSNe (see Bochenek, Ravi, & Dong (2021) [75]), but is inconsistent with work that finds it unlikely that Type Ia SNe are associated with every FRB (see Marnoch et al. (2020) [76]).

1.3.3 A Few Specific FRBs

There are a few specific FRBs which have received significant attention: FRB 20121102A, FRB 20180916A, FRB 20200120E and SGR 1935+2154. FRB 20121102A, which was initially detected in 2012, became the first repeating FRB when archival data showed additional bursts from the source [77], [78]. The repetitions allowed for follow-up observations of the source with FRB 20121102A now one of the most frequently studied FRBs¹⁴.

Since its initial discovery, FRB 20121102A has been localized to sub-arcsecond precision by Chatterjee et al. (2017) [80] and further localized to dwarf galaxy at a redshift of $z = 0.2$ by Tendulkar et al. (2017) [42]. The location of the FRB is spatially coincident with a compact, persistent radio source (see Marcote et al. (2017) [81]), and lies in a rather extreme magnetic environment with 100% linearly polarized emission and a large ($\sim 10^5$ radians m^{-2}), variable RM [82]. Additionally, the bursts from FRB 20121102 show structure down to $\sim 30 \mu\text{s}$ and exhibit the downward drifting often seen in repeating FRBs (see Fig. 1.4) [82], [83]. When combined with the persistent emission and extreme magnetic environment, this hints at the FRB being located within a SNR, a highly magnetized wind nebula, or nearby to an accreting black hole. Most recently, a periodicity of ~ 157 of days was suggested for FRB 20121102A [46], [47]. The long period is best explained by a high mass X-ray binary, although might be due to a flaring magnetar or a precessing neutron star [46].

¹⁴We note that FRB 20121102A is likely atypical among FRBs, lying in a rather extreme environment [79].

In addition to FRB 20121102A, FRB 20180916A also shows periodic emission, and was actually the first FRB for which a periodicity was noted. First discovered by the CHIME/FRB collaboration (see [45]), this FRB has a much shorter period of 16.4 days. The periodic nature of the source hints at a neutron star in orbital motion or binary precession. Models involving isolated sources are likely implausible [45]. Additionally, the source has been detected down to ~ 100 MHz, making it the lowest-frequency detected FRB [84].

A third FRB that has received significant attention is FRB 20200120E. First discovered by the CHIME/FRB collaboration, FRB 20200120E is coincident with a globular cluster within M81 [43], [44]. This is rather surprising, as one of the leading formation channels for FRBs involves a magnetar formed through a CCSNe. However, as globular clusters host older stellar populations, a magnetar existing in a globular cluster and formed through a CCSNe likely should not produce FRBs (if a magnetar this old could even exist at all). A different mechanism (although likely still involving a neutron star) is needed to explain this FRB. Additionally, located only 3.6 Mpc away, this FRB is a strong candidate for follow-up observations in the optical, X-ray, and gamma-ray bands.

The last FRB which we will mention is SGR 1935+2154. As this FRB is the focus of Chapter 4, we will only briefly touch upon it here. SGR 1935+2154 is a well-known Galactic magnetar, which prior to April 2020 had only been detected by high-energy telescopes. However, on 28 April 2020, it emitted an FRB-like burst which was detected both by radio

and high-energy telescopes. While not quite as energetic as a “typical” FRB, the burst is significantly more energetic than radio bursts seen from any previous Galactic magnetar (see Fig. 1.3). It appears as a bridge between the magnetar and FRB regimes.

1.3.4 Possible Progenitor Models

FRB progenitor models can be broken down into three categories: 1. cataclysmic events (which can only be applied to “one-off” FRBs), 2. interacting systems (such as those invoked for FRB 20121102A or FRB 20180916A), or 3. isolated compact objects. Here we only focus on the third category of models, but we direct the reader to Petroff, Hessels, & Lorimer (2021) [85] for more detailed descriptions of progenitor and emission models.

If we consider compact, isolated objects as the progenitors of FRBs, then FRBs likely originate from neutron stars rather than white dwarfs due to the short duration of the emission (μs to ms timescales). Most models invoke magnetars over pulsars due to the large energies required to produce FRBs. However, some theories still involve giant pulses emitted from young pulsars similar to the Crab (see Cordes & Wasserman (2016) [86], Connor, Sievers, & Pen (2016) [87], and Lyutikov, Burzawa, & Popov (2016) [88] for further details). Of the theories that involve magnetars, there are two primary models for producing the coherent emission seen from FRBs. In the first model, the emission is produced in the neutron star’s magnetosphere through curvature radiation. The curvature radiation is produced by bunches of charged particles moving along curved magnetic field lines. For further details

on this model, we direct the interested reader to Kumar, Lu, & Bhattacharya (2017) [48] and Lu & Kumar (2018) [89]. In the second model, a flare is produced by the magnetar, which then collides with the surrounding medium producing an outward moving shock wave. When the shock wave collides with a surrounding, magnetized medium, Larmor rotation of particles within the shock can eventually (through population inversion) lead to the release of a coherent electromagnetic wave [49]. We direct the reader to Lyubarsky (2014) [90], Beloborodov (2017) [91], and Metzger, Margalit, & Sironi (2019) [49] for further details on this model.

We proceed in the next section by describing in detail the Canadian Hydrogen Intensity Mapping Experiment Fast Radio Burst Project (CHIME/FRB). This project is aimed at detecting FRBs, although it has also detected several pulsars (see Good et al. (2020) [92]) and the magnetar SGR 1935+2154 (see CHIME/FRB Collaboration (2020) [8]), hence the background given to all three classes of astrophysical objects.

Chapter 2

The Canadian Hydrogen Intensity

Mapping Experiment

2.1 The Telescope

The Canadian Hydrogen Intensity Mapping Experiment, herein abbreviated as CHIME, is located in Penticton, British Columbia. Originally built to study the Baryon Acoustic Oscillation (BAO) signal through 21-cm hydrogen emission at redshifts of 0.8 to 2.5, it is a transit radio telescope designed to operate with a large field of view (FOV) and enough sensitivity to map the BAO. However, its large FOV and transit nature also make it a great candidate for blind FRB searches and pulsar timing. Thus, CHIME is composed of three different projects: CHIME/Cosmology, CHIME/FRB, and CHIME/Pulsar. There is also



Figure 2.1: A photograph of CHIME as taken on 15 September 2016 in Penticton, British Columbia. The four N-S cylinders are visible along with the focal lines containing the 256 dual polarization feeds. Image courtesy of CHIME/FRB Collaboration (2018) [1].

an additional project underway to search for slow pulsars, and three outrigger sites under construction to localize > 1000 FRBs detected by CHIME/FRB to 50 mas.

CHIME consists of four, 100-m x 20-m cylindrical, parabolic reflectors with the reflectors oriented in the north-south (N-S) direction (see Fig. 2.1). It has a N-S FOV of $\sim 120^\circ$ and an east-west (E-W) FOV of ~ 1.3 to 2.5° (dependent on frequency with 1.3° corresponding to 800 MHz) for a total FOV of $\sim 250^\circ$ [93]. Each of the four reflectors has 256 dual polarization feeds hanging along its axis for a total of 2048 antennas operating between 400 and 800 MHz. The feeds are placed along the focal lines, spaced by 0.3 m and at a height of 5 m. The 400 to 800 MHz band was chosen with the BAO in mind, as the 21-cm hydrogen emission line is redshifted to ~ 800 MHz at z of 0.8 and ~ 400 MHz at z of 2.5 [94].

The 2048 antenna signals are fed into a hybrid FX correlator where the F-engine digitizes and transforms the antenna signals and the X-engine performs spatial correlation. The F-engine operates on Field Programmable Gate Arrays (FPGAs) and digitizes the ADC voltages for each antenna at a rate of 13.1 Tb s^{-1} . A polyphase filterbank is used to perform a discrete Fourier transform to channelize the data into 1024 frequency channels. The data rate is then reduced to 6.5 Tb s^{-1} corresponding to a sampling rate of $2.56 \mu\text{s}$.

The digitized data are sent to the X-engine which consists of 256 GPU nodes. Each node processes four of the 1024 frequency channels. The X-engine produces a set of data products for each of the CHIME projects e.g. 2M visibilities for CHIME/Cosmology, 1024 formed beams for CHIME/FRB, and 10 tracking beams for CHIME/Pulsar. Focusing on CHIME/FRB, the X-engine forms 256 N-S beams through a spatial fast Fourier transform (FFT) of the pre-correlated antenna signals. This is unlike the more traditional interferometry where pairwise correlation is used to produce a set of visibilities. FFT algorithms are computationally much cheaper than pairwise correlation, scaling as $N \log N$ rather than N^2 where N is the number of antennas [95]. For telescopes such as CHIME with a large number of equispaced antennas, FFT algorithms are considerably computationally cheaper. One challenge is that the resulting FFT beams on the sky are highly frequency dependent. To overcome this, the initial input data are padded with zeros to form 512 FFT beams. Then, for a given sky location, multiple FFT beams are selected to form a new beam whose centre depends very weakly on frequency. The final result is 256

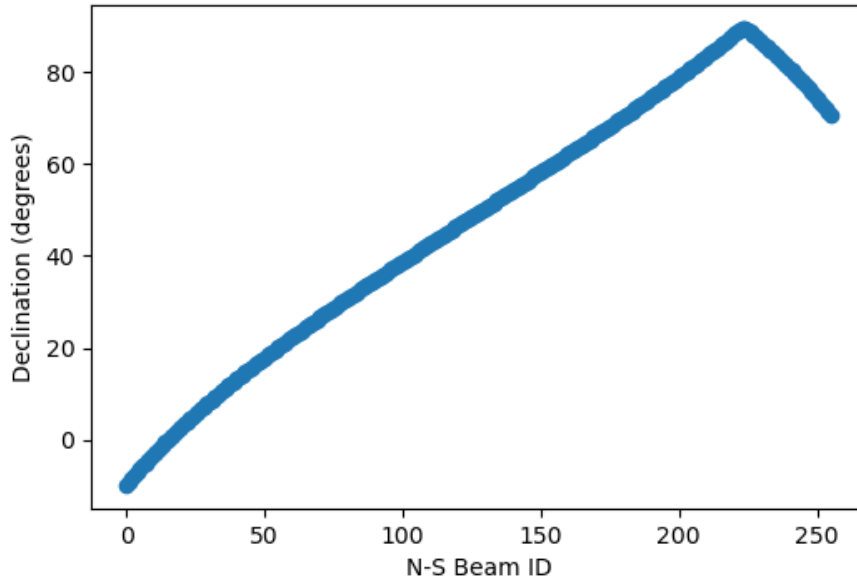


Figure 2.2: Mapping between the N-S CHIME/FRB beams and declination at 19:29:10 UTC on 2021-08-03. Note the mapping depends on the time at the observatory, so this is only one approximation of the relation.

N-S beams which span from declinations of approximately -10° to $+89^\circ$ and are evenly spaced in $\sin \theta$ where θ is the angle from zenith (see Fig. 2.2 for an approximate mapping between declination and N-S formed beam). For more details on the formed beams, we direct the reader to Masui et al. (2019) [95] and Ng et al. (2017) [93]. In addition to 256 N-S beams, four E-W beams are formed using exact phasing for a total of 1024 stationary formed beams.

The X-engine also upsamples the frequency resolution for CHIME/FRB from 1024 frequencies to 16k frequencies and downsamples the time resolution from $2.56 \mu\text{s}$ to 0.983

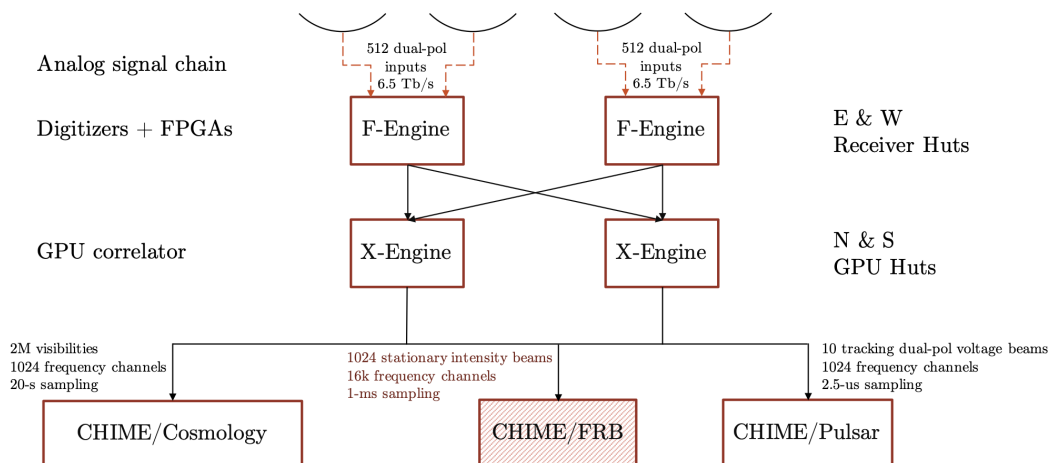


Figure 2.3: Schematic of the CHIME pipeline. Each cylinder contains 256 dual polarization inputs which are digitized and Fourier transformed by two F-engines. The output of both F-engines is fed into two X-engines which perform spatial correlation. The results of the X-engine are sent to the three backends: CHIME/Cosmology, CHIME/FRB, and CHIME/Pulsar. Schematic courtesy of CHIME/FRB Collaboration (2018) [1]

ms using a Fourier-transformation [1]. For CHIME/Pulsar, the frequency resolution is maintained at 1024 frequencies with a sampling time of $2.56 \mu\text{s}$. For CHIME/Cosmology, the nominal 1024 frequency channel resolution is maintained but the sampling time is reduced to 20 s. A schematic of the FX correlator and the different outputs is shown in Fig. 2.3 and extracted from CHIME/FRB Collaboration (2018) [1].

While CHIME/Pulsar Collaboration (2020) [96] and Newburgh et al. (2014) [97] discuss the CHIME/Pulsar and CHIME/Cosmology backends, respectively, in more detail, we focus below on the details of the CHIME/FRB pipeline.

2.2 The CHIME/FRB Backend

As a transit telescope with a large FOV, CHIME can monitor large portions of the sky with consistent daily exposure. This is especially useful for detecting new FRBs for which temporal and spatial information is not available. Since its commissioning in 2018, CHIME/FRB has detected over 2000 FRBs and published over 500 [2]. This has revolutionized the field, with CHIME/FRB detecting magnitudes more FRBs than any other existing radio telescope.

Due to the large data rate from CHIME of ~ 142 Gb/s, the CHIME/FRB pipeline must operate in real-time, and this real-time search pipeline is split into four processing levels: L1, L2, L3, and L4. Each pipeline is discussed below and shown in Fig. 2.4.

2.2.1 L1

L1 consists of 128 nodes with two central processing units (CPUs) per node. Each node processes all 16k frequency channels for 8 formed beams at a ~ 1 ms sampling rate. L1 has four main components: 1. a radio frequency interference (RFI) removal process, 2. a de-dispersion algorithm, 3. an event detection algorithm, and 4. an RFI sifting algorithm. The first three components are called L1a while the fourth is called L1b. Each beam has L1a and L1b independently run on it.

First, RFI mitigation is performed through *rf-pipelines* (Rafiei-Ravandi, M., *in prep.*). Data arrive in *rf-pipelines* in two parallel arrays, one consisting of intensity information and

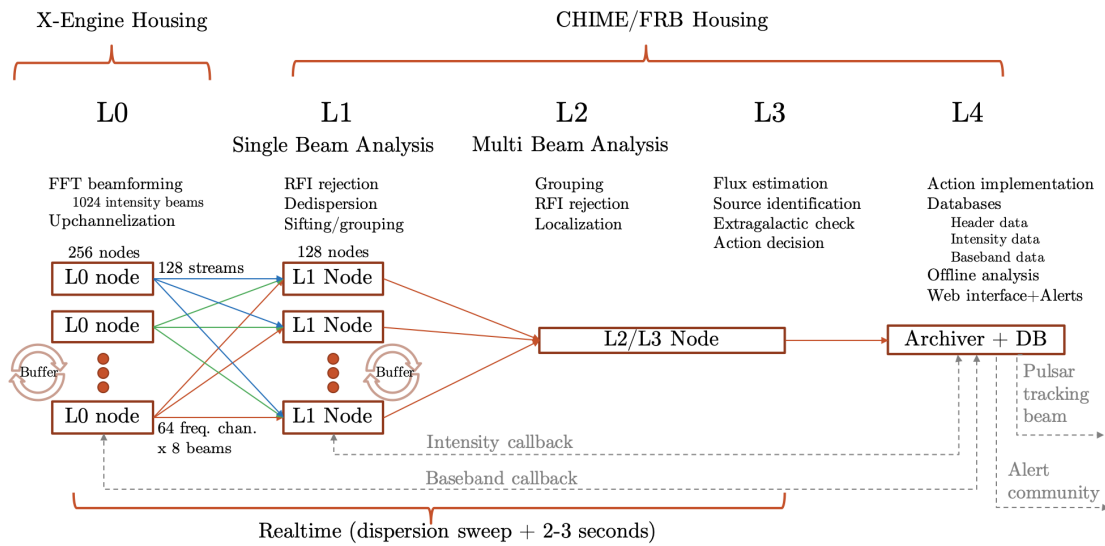


Figure 2.4: A schematic of the different CHIME/FRB pipelines starting with the X-engine (also called L0) and ending with L4. The schematic contains the number of nodes required for each processing pipeline, along with the main responsibilities of each pipeline. Figure courtesy of CHIME/FRB Collaboration (2018) [1].

the other consisting of the weights. The initial input signal consists of a gaussian signal plus non-gaussian outliers which are iteratively removed through a chain of transforms. The chain is configured to minimize false positives and false negatives while remaining computationally efficient.

Each transform operates on a four second chunk of intensity data and weights. First, nine different clipping transformations are applied to the intensity and weights. Each clipping applies a specified cutoff of the intensity amplitude and adjusts the weights for the segments above the cutoff. While the weights could theoretically be any floating point number, the weights in *rf-pipelines* are limited to either 0 or 1. Each clipper outputs the intensity data, untouched, and the weights, readjusted by the results of the clipping. The weights and intensity data are then fed into the next clipping transformation.

The nine clipping transformations are repeated six times before the data are passed on to a detrender. The data are detrended twice, once using a 4 degree polynomial and once using a 12 degree spline. Each detrending operation happens both along the frequency axis and along the time axis. The detrending transform aims to capture broadband signals such as RFI or uncalibrated variations in the spectrum. The polynomial/spline are then subtracted from the intensity data to remove the large scale noise and find the narrowband FRBs (although most FRBs span the entire band). The detrending transforms alter both the intensity and weight arrays. The sequence (9 clippings, repeated 6x, detrended 2x in both frequency and time) is then repeated once more.

After *rf-pipelines*, the data are de-dispersed. CHIME/FRB must search 1.5 PB of data per day which makes de-dispersion the most computationally expensive part of the CHIME/FRB pipeline [1]. Direct de-dispersion for this quantity of data is too expensive (computational cost is on order TF^2 where T is the number of time samples and F the number of frequency samples). Instead, tree de-dispersion (for which the computational cost is on order $TF \log F$) is deployed through a new algorithm, *bonsai* [98]. Tree algorithms suffer from two major problems though, namely memory bottlenecks and loss of S/N in approximating the DM delay. *Bonsai* overcomes these issues by processing data in smaller sample sizes and by weighting the data depending on the DM and pulse width size in (ν^{-2}, t) space rather than in (ν, t) space. For a set of spectral indices, scattering times, and intrinsic width parameters, *bonsai* then calculates an approximate S/N for a grid of DMs and times.

All events above a given S/N limit are sent to L1b. L1b uses a supervised machine learning algorithm to determine whether an event is astrophysical or RFI by analyzing events in the (DM, time) plane. Events from a true astrophysical candidate tend to exhibit a bowtie shape in this plane while RFI tends to exhibit a straight line. Each event is assigned an L1b RFI rating and is then passed on to the next stage of the backend: L2/L3. For more details on this stage of L1, we direct the reader to Josephy (2018) [99].

2.2.2 L2/L3

L2/L3 performs additional analysis to group multi-beam events, improve the initial localization, estimate the flux, determine the nature of a source (Galactic, extragalactic, known, unknown), and decide which set of actions to perform based on the previous classifications. More specifically, L2 groups events in neighbouring beams and then uses the machine learning algorithm of a support vector classifier to determine whether groups are astrophysical or RFI. The classifications are based on the time, DM, and sky position of the grouping along with the L1b RFI ratings. Astronomical events typically occur in one or two beams with high S/N and a few weaker nearby beams while RFI events occur in multiple beams with the peak S/N beams spread throughout. Events classified as RFI by L2 are passed directly to L4 (see Section 2.2.3), while astrophysical events continue on to L3.

L2 also improves the localization of all candidates. A look-up table is computed for multi-beam events which contains a grid of the S/N ratio for different beams for a grid of sky locations. Thus, for multi-beam events, the relative S/N ratios for each beam are compared to this lookup table to improve the initial localization. For single beam events, a mapping between the centre of the beam and sky position is used [1]. Lastly, L2 calculates approximate radio fluxes for each event using the radiometer equation.

After L2, all astrophysical events are sent to L3. Using a known source database and models for the maximal Galactic DM along a given LOS, L3 classifies events as Galactic

or extragalactic, and then as known or unknown based on an event's DM and position. Depending on the classification, L3 selects a set of actions for the event. Actions can include things such as callbacks of buffered intensity and baseband data. Due to the high volume intake of data by CHIME, intensity and baseband data are not automatically stored for every event. Instead, a ring buffer is used to store up to ~ 240 s of intensity data¹ and up to ~ 40 s of baseband data.

2.2.3 L4

L4 then implements the actions decided in L2/L3. For example, data stored in the ring buffers are retrieved for events for which an intensity callback was requested. L4 is also responsible for storing the header information and all additional information for all L2/L3 events (including RFI, known sources, and unknown sources). All events not discarded by L1 are archived by L4 into CHIME/FRB's databases.

¹Data stored for 240 s have been downsampled in time by a factor of four. Full resolution data are only saved for ~ 60 s)

Chapter 3

The *rfi-scout* Pipeline

3.1 Radio Frequency Interference at Radio Telescopes

3.1.1 Challenge of Radio Frequency Interference

While radio astronomy is fortunate to operate at wavelengths long enough to penetrate through the Earth's atmosphere, allowing the use of ground-based observatories, it is not without its challenges. Radio observatories operate within the same frequency range as digital broadcasting signals, cellular networks, and satellite communications. The radio frequency interference (herein called RFI) caused by these synthetic signals can be significantly larger than the desired astrophysical signals. RFI can also emanate from astrophysical sources; the Sun, Moon, and bright calibrators (e.g. Cygnus A, Taurus A, Cassiopeia A) can be labelled as interference as they can completely saturate the observing

bandwidth.

RFI mitigation and characterization is a core aspect of radio astronomy. Amongst the recent literature on the RFI environment at different telescopes, three surveys are relevant for CHIME/FRB. The first two surveys were performed by Indermuehle et al. (2016) [100] and Sokolowski, Wayth, & Ellement (2014) [101] in Australia at the future location of the Square Kilometer Array (SKA) in the 700 to 1700 MHz and in the 70 to 300 MHz frequency bandwidths, respectively. Even though the location of the SKA is in a radio quiet zone, Indermuehle et al. (2016) [100] finds that up to $\sim 15\%$ of its spectrum can be lost to RFI with the majority of this due to external, broadband (> 5 MHz) RFI and the minority internal, narrowband RFI. Additionally, both studies detect interference signals produced up to 600 km away. They attribute this to 2G, 3G, and 4G signals that have been reflected and refracted in the atmosphere for significant distances [100], [101].

Another more recent study by Tingay et al. (2020) [102] is similarly performed at the location of the SKA. However, unlike the previous two surveys which contain only temporal information, this survey also contains spatial information on the RFI. Tingay et al. (2020) [102] focuses on a specific one MHz frequency channel in the frequency modulation (FM) radio broadcasting bandwidth over a period of three days. They find many reflected FM signals off of airplanes and meteor trails.

With the above three studies and their implications in mind, we proceed below by adding more detail on the RFI situation at CHIME/FRB.

3.1.2 Radio Frequency Interference at CHIME

CHIME is located in a radio quiet zone near Penticton, British Columbia at the National Research Council’s Dominion Radio Astrophysical Observatory (DRAO). This site is surrounded by mountains, which naturally reduces the RFI. However, similar to the SKA, CHIME still suffers from considerable RFI. As discussed in Section 2.2.1, one way in which CHIME/FRB masks RFI is through *rf-pipelines*. The average amount of data masked by *rf-pipelines* is typically on the order of 20% with the minimum masking fraction for all beams fairly steady around 15% and the maximum fluctuating from 40% to 60%.

While this is just the L1 masking fraction, the masking fraction we record for CHIME/FRB science metrics also includes effects from L0. As discussed in Section 2.1, each L0 node is responsible for four frequency channels. When a node is offline, it is equivalent to those four frequency channels being masked at 100%. We record this combined masking fraction (offline L0 nodes plus *rf-pipelines* masking) rather than just the *rf-pipelines* masking fraction because it better reflects the available portion of our frequency bandwidth. When including these offline L0 nodes, the average masked percent is closer to 35%. This total mask (L0 + L1) can fluctuate depending on the L0 nodes that have been blacklisted, and is typically higher prior to a system-wide telescope upgrade and lower after an upgrade as blacklisted nodes are often debugged during these upgrades. The remainder of this chapter, and the analysis that follows, is based on this combined masking

fraction.¹

There are a variety of sources, some known and some unknown, responsible for the RFI at CHIME. In Canada, the LTE band² spans radio frequencies in the range of 698 MHz to 787 MHz. As discussed in Section 2.2.1, the majority of *rf-pipelines* works through dynamical masking where the mask per frequency channel is determined in real-time. However, certain frequency channels such as those within the LTE band are also statically masked, meaning they are consistently set to a masking fraction of 100%. This can be seen in Fig. 3.1 where we show the CHIME/FRB masking fraction per frequency channel averaged over an entire day and over all beams. Many frequency channels from 725 to 750 MHz are masked at, or close to, 100%. Prior to 2020, the main source of RFI from cellular networks was concentrated around 700 MHz. However, in early and late 2020, 5G networks came online³ and their effects were seen rather dramatically in the CHIME/FRB band, especially due to the 5G downlink for wireless networks around 635 MHz (see Fig. 3.1). There is also substantial masking in the frequency range of 450 to 600 MHz as the ultra-high frequency (UHF) TV channels in Canada operate in the range from 470 to 602 MHz. There is little RFI masking directly above the UHF TV band as there is an allocated radio astronomy band from 609 to

¹This combined masking fraction is queried from L1, and so unless stated otherwise, is just called the L1 masking fraction.

²LTE is an acronym for the long-term evolution frequency bandwidth. For further details on it, see the Section *Long-term Evolution* of Frenzel (2018) [103].

³These networks are largely a result of the [2019 Canadian 600 MHz auction](#). The auction results can be found [here](#).

614 MHz.⁴

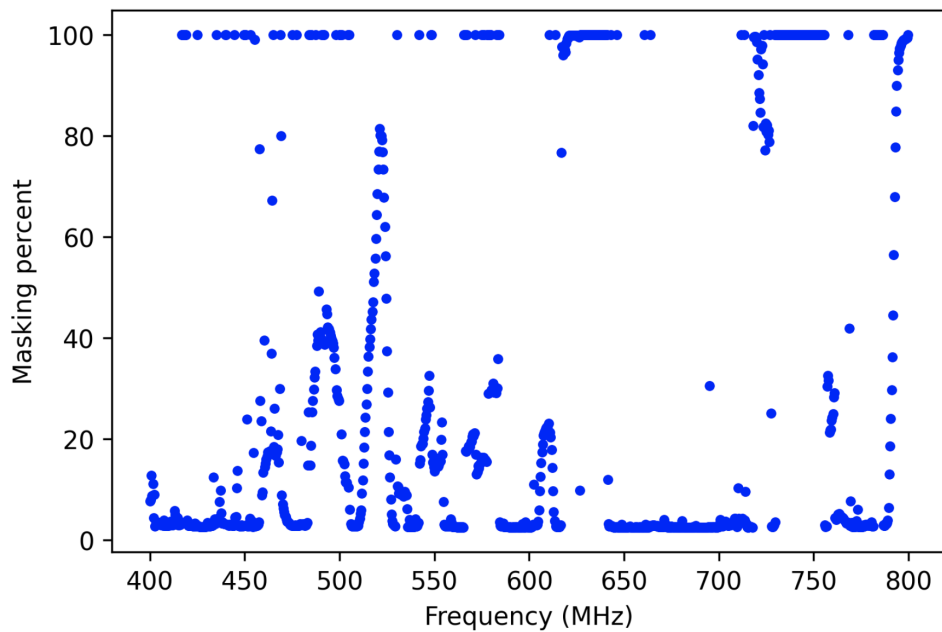


Figure 3.1: CHIME/FRB L1 masking percent as a function of frequency. The masking percent is averaged over all beams and over all timestamps from 2021-05-18 to 2021-05-19. The majority of the LTE band in the 700 MHz band is masked at 100% while the TV band from 470 to 600 MHz also shows significant masking. The figure includes contributions from offline L0 nodes, where one offline L0 node is equivalent to four frequency channels masked at 100%. It is impossible to differentiate L0 masking, static *rf-pipeline* masks, and dynamic 100% masking from *rf-pipeline*.

The masking fraction of CHIME/FRB is also highly dependent on the N-S beam location⁵ as seen in Fig. 3.2. Unsurprisingly, the edge beams (those furthest north or south) suffer from the most RFI as these are the least shielded from ground noise. There is also an

⁴For details on the different frequency allocations, we direct the reader to the [Canadian Table of Frequency Allocations](#).

⁵See Fig. 2.2 in Section 2.1 for a mapping between N-S beam number and declination.

increase in the RFI masking fraction for beams ~ 100 to 150. Two of CHIME’s calibrators, Cassiopeia A and Cygnus A, transit above CHIME in beams ~ 150 and ~ 110 , respectively. The signals from these two celestial objects, along with Taurus A which transits at beam 55, are very prominent across all frequency bandwidths. Thus, L1 treats these objects as sources of RFI and masks their signal. The Sun is similar except it transits through a larger number of beams. When the Sun is along CHIME’s meridian, its signal can saturate many frequency and beam channels as seen in the bottom panel of Fig. 3.3 where the CHIME/FRB mask is shown as a function of both beam and frequency at the time of the Sun’s transit.

In late 2020 and early 2021, CHIME/FRB detected an enormous number of RFI events per day, with a peak of 1.7M RFI events/day with $S/N > 7.5$. This huge increase in the number of RFI events, for which we typically detect $\sim 20k$ to $30k$, are herein called “RFI storms”. We identify two distinct RFI storms: one at high DMs ($> 1000 \text{ pc cm}^{-3}$) and another at medium DMs (~ 500 to 1000 pc cm^{-3})⁶.

The two RFI storms are different in their DM range, time dependence, and beam distribution. The high DM RFI storms occur on a ~ 20 minute timescale, with the storms detected in the edge N-S beams. The mid-DM RFI storms occur on 8 second timescales, and are more evenly detected in all N-S beams with a slight fall-off for the edge N-S beams. For both storms, we captured intensity data on approximately 10 different occurrences for various beams to identify the frequency channels responsible for the RFI storms. Four

⁶These RFI storms are likely caused by terrestrial RFI, and so DM has no physical meaning here. Instead, it merely reflects the level of de-dispersion which maximizes the S/N of the RFI.

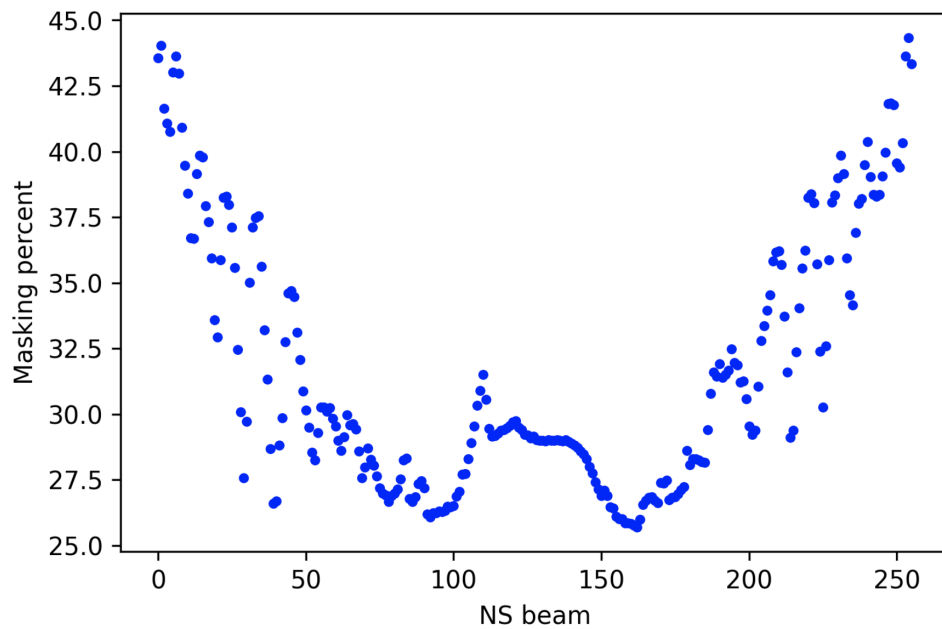


Figure 3.2: CHIME/FRB L1 masking percent as a function of N-S beam. The masking percent is averaged over all frequencies, all E-W CHIME columns, and over all timestamps from 2021-05-18 to 2021-05-19. The masking fraction is highest for the beams furthest north and south. There is also elevated masking for N-S beams 100 to 150. While this figure includes contributions from offline L0 nodes, this does not affect the relative masking per beam, but instead just raises the baseline over all beams.

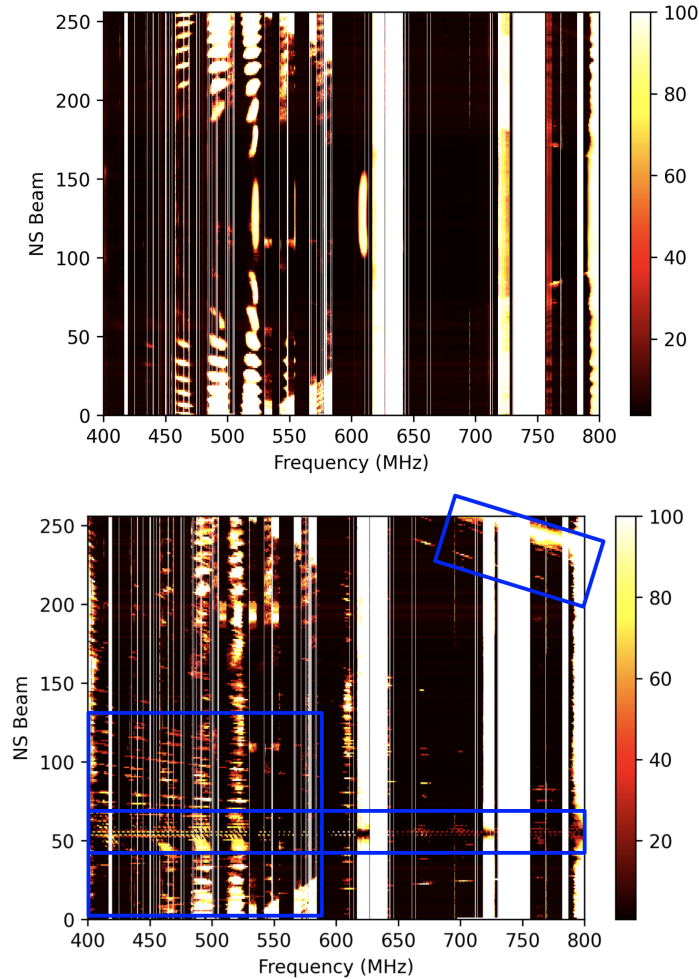


Figure 3.3: The CHIME/FRB L1 masking percent as a function of both beam and frequency. The masking percent is averaged over all E-W beam columns. In the top panel, the masking fraction is averaged over all timestamps between 2021-05-18 and 2021-05-19. In the bottom panel, the metrics are displayed for 2021-05-18 at 19:55 UTC. The Sun transits above CHIME between 2021-05-18 19:54 and 2021-5-18 19:55 UTC. The colour scheme corresponds to the percent masked, with white being 100% masked. Effects due to the Sun are circled in blue. The figure includes contributions from offline L0 nodes, where one offline L0 node is equivalent to four frequency channels masked at 100%. It is impossible to differentiate L0 masking, static *rf-pipeline* masks, and dynamic 100% masking from *rf-pipeline*.

frequency ranges are identified as the sources of the high DM RFI storms: 781.8 to 786.7 MHz, 418.3 to 419.2 MHz, 417.2 to 417.6 MHz, and 440.2 to 440.4 MHz. The 700 MHz signals are likely new LTE sources, but it is unclear what causes the 400 MHz signals. For the mid-DM RFI storms, only one frequency range is identified: 627.2 to 641.4 MHz. The downlink for 5G telecommunications lies in this range and is likely responsible for this source of RFI. As a solution to the RFI storms, the CHIME/FRB team added additional static masks to *rf-pipelines* for the frequency ranges listed above. This increased the average L1 + L0 masking fraction from $\sim 29\%$ (early 2020) to $\sim 35\%$ (early 2021).

The static mask of 627.2 to 641.4 MHz can clearly be seen in Fig. 3.3 where we show the L1 masking percent as a function of both beam and frequency. The high level of both dynamic and static masking in the LTE band from ~ 720 MHz to ~ 760 MHz is also evident along with the TV band from ~ 460 to ~ 580 MHz. While there are some frequency channels in the band of ~ 460 to ~ 580 MHz that are almost 100% masked, there are also several ~ 20 MHz frequency bandwidths for which the masking shows a ripple feature as a function of beam, with little to no masking towards the more central N-S beams.

As seen through Figures 3.1 - 3.3, CHIME/FRB's RFI is rather complicated. It is highly dependent on both beam and frequency with the masking percent as high as 50% for certain beams and as high as 100% for certain frequency channels. Recording the L1 RFI masking fraction is important for incorporating RFI metrics into daily exposure calculations (Chawla, P., *in prep.*), quantifying and understanding unknown sources of RFI, and monitoring the

system sensitivity. For example, FRBs occur on millisecond timescales, but there are entire 4 second periods (discussed below in Section 3.1.3) with masking fractions $> 50\%$, causing us to operate rather blindly. This has implications for our exposure calculations which affect rate and repetition statistics. The RFI metrics can also be compared with other system sensitivity metrics such as the number of pulsars detected per day or the synthetic pulse injection system to gain a deeper understanding of our system. Thus, in early 2020, we began collecting daily L1 RFI masking metrics. We detail this initial collection process below.

3.1.3 Previous CHIME/FRB RFI Pipeline

Starting in early 2020, we began routinely collecting L1 RFI masking metrics. The metrics are retrieved from the L1 nodes using a synchronous Remote Procedure Call (RPC)⁷ on a 1-minute timescale. For every beam, we store several different metrics such as start and end timestamps, the number of masked samples, and the total number of samples in a Structured Query Language (SQL) database⁸ on a per beam and per frequency basis. This amounts to a data volume of $\sim 16\text{G/day}$ or $\sim 5.6\text{T/year}$. The data are analyzed offline to produce graphs of the masking fraction per beam, per frequency, and per timestamp.

As noted above, using this method, the RFI metrics are sampled on a minute timescale,

⁷A remote procedure call is a method for communicating between two networks based on synchronous calls from a local machine to a remote server. For further details on remote procedure calls, we refer the reader to the PhD thesis presented in Nelson (1981) [104].

⁸SQL is a relational database. The data are assumed to be related to each other and are stored in tables. We direct the reader to [IBM's description of relational databases](#) for more information.

with the reported L1 RFI masking fraction averaged over the entire one minute period. The timescale of one minute was chosen as a compromise between having sufficient time resolution and collecting a manageable amount of data. The exposure for CHIME/FRB, on the other hand, is calculated on a four second timescale. We had never investigated the RFI metrics on a similarly short timescale, so we collected data on 24 May 2020 at a rate of five seconds and then downsampled to 10, 20, 40, 60, and 240 second averages to compare the different sampling rates.

As seen in Fig. 3.4, while sampling on a longer timescale (i.e. 60 seconds and 240 seconds) captures the baseline trend of the RFI, it does not capture extrema where the RFI mask is greater than 35% to 45%. If we define a chunk as the average RFI mask over a 5 second period, then on average there are order ten chunks per day where our RFI masking for a beam is greater than 45%. As one such example, consider beam 180 on 24 May 2020. Sampling at a five second cadence, there are 42 chunks for which the masking fraction is greater than 45%. However, if we sample at a sixty second cadence, these maxima are averaged out with only two averages having masking fractions greater than 45%⁹. As FRBs are transient events lasting for milliseconds, these moments of high masking fractions may leave us partially blind to these events. It is essential to account for these moments in exposure and system sensitivity metrics, and thus necessary that we sample the RFI metrics on a much shorter timescale than the initial choice of 60 seconds.

⁹Note that these two time averages do not encompass all 42 earlier time chunks for which the masking fraction was high.

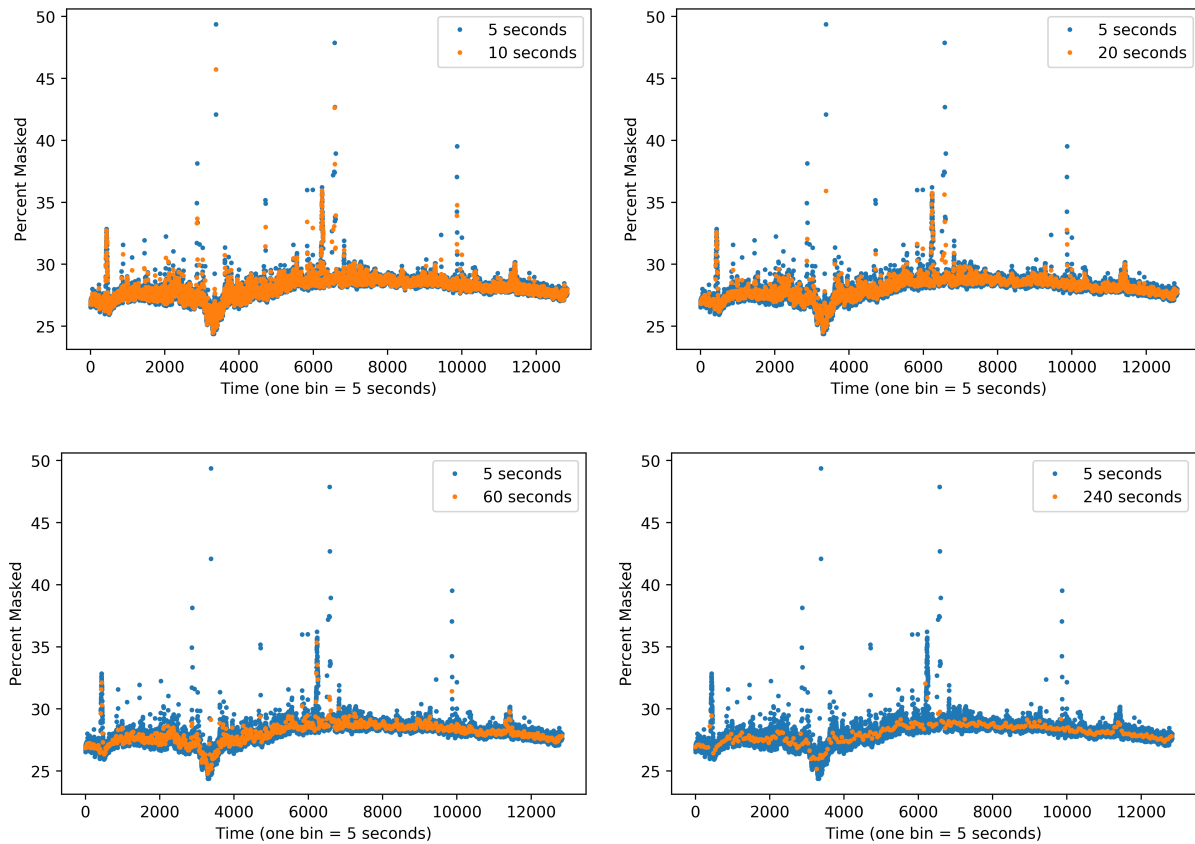


Figure 3.4: Comparison between the L1 masking fraction on 24 May 2020 for beam 130 sampled every five seconds with four other L1 sampling rates: ten (top left), twenty (top right), sixty (bottom left), and 240 (bottom right) seconds. The RFI metrics are averaged over all frequency channels. For each sampling rate, the L1 RFI masking fraction is averaged over the entire time chunk. For example, at a twenty second cadence, each data point represents the average L1 RFI masking fraction for the past twenty seconds.

However, storing the RFI metrics on a five second time scale using the above RFI pipeline is not feasible. First, it would greatly increase our data storage. We would be storing $\sim 240\text{G}$ of data per day or $\sim 84\text{T}$ per year. This is not practical over the course of many years. Additionally, it takes the RPC client ~ 5 to 15 seconds to collect all the RFI metrics from L1. Thus, consistently collecting metrics at a five second time scale is not possible using this software. To this end, we build a new pipeline for collecting L1 RFI metrics on the desired time scale while simultaneously analyzing the data in real-time to decrease our data storage.

3.2 Pipeline: *rfi-scout*

3.2.1 Objectives

The new RFI pipeline, herein called *rfi-scout*, collects and analyzes L1 metrics in real-time, similar to other CHIME/FRB backends. *rfi-scout* deploys a new method for querying L1 RFI metrics so that they can easily be accessed and recorded on a four second timescale¹⁰. The metrics are then downsampled through various algorithms (discussed in Section 3.2.2) to reduce the overall storage pressure so the metrics can be collected and stored for the entire CHIME/FRB operational period. Additionally, the metrics are stored in a location accessible to all CHIME/FRB users, and can easily be maintained and accessed by others within the collaboration.

¹⁰Four seconds is chosen to match exposure times.

Below, in Section 3.2.2, we outline the *rfi-scout* pipeline. In the following Section 3.2.3, we discuss the benefits achieved by the *rfi-scout* pipeline. We end by discussing future work for *rfi-scout*. For additional details on the *rfi-scout* pipeline and more specific investigations into its different components, we direct the reader to Appendix A.

3.2.2 Structure

The *rfi-scout* pipeline has five key structural components:

1. Querying metrics from L1.
2. Storing the initial L1 RFI metrics.
3. Data reduction I: downsampling over frequency channels.
4. Data reduction II: downsampling over the E-W columns of CHIME.
5. Data reduction III: fitting a polynomial to the RFI per beam and per frequency.
6. Storing the results in a mongoDB database.

This is also depicted in Fig. 3.5.

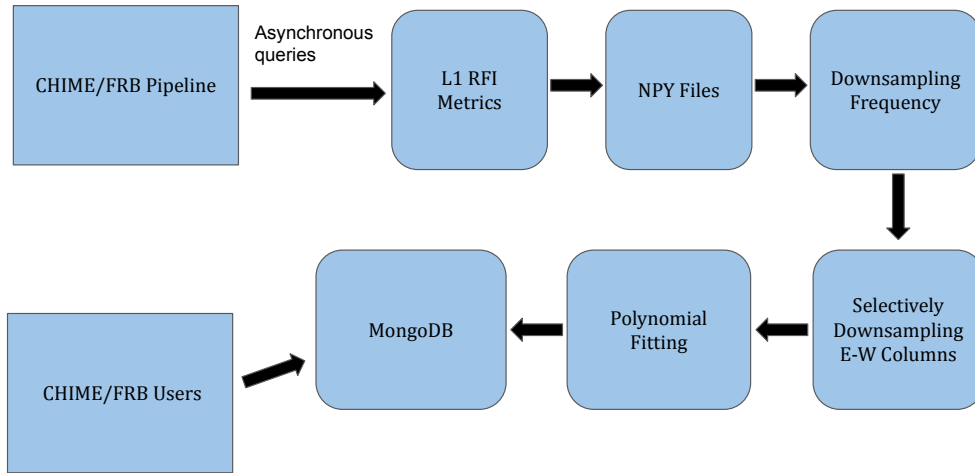


Figure 3.5: Flowchart of the *rfi-scout* pipeline. The data are initially queried from L1 using asynchronous queries and stored in npy files. The data are then reduced through frequency downsampling, downsampling over the E-W CHIME columns, and polynomial fitting. They are finally stored in a mongoDB database which can be accessed by CHIME/FRB users.

Below, we detail each of these five parts.

L1 query and Initial Storage

Previously, L1 RFI metrics were queried using an RPC client, with the client performing synchronous calls to each L1 node to retrieve the RFI metrics. However, it takes ~ 10 seconds to retrieve the L1 RFI metrics for all CHIME/FRB nodes using this method which is a factor of two larger than our desired query time of 4 seconds (to match exposure times). To overcome this, we implement a slightly different technique using asynchronous queries.

Using asynchronous queries greatly reduces the overhead time to query L1 metrics to ~ 1 second for all nodes. After querying the L1 metrics, we decode the metrics¹¹ and store the mask per frequency and per beam at the full resolution of 1024 frequencies and 1024 beams in npy files¹².

Data Reduction

Every six hours, we retrieve the RFI metrics from the npy files for further analysis and reduction. Downsampling is an essential part of *rfi-scout*, as the increased sampling rate increases the data storage pressure to a non-sustainable level. First, we downsample the data in frequency from 1024 frequency channels to 256 frequency channels, averaging over every four frequency channels. It is tempting to downsample to a smaller number of frequency channels as the exposure is solely calculated on a per beam basis with no dependence on frequency. However, the frequency dependence of the RFI is still relevant for other science purposes e.g. the usage of the CHIME/FRB RFI metrics to estimate CHIME/FRB's bandwidth in Josephy et al. (2021) [62]. Additionally, the frequency dependence of RFI metrics can be useful for identifying new sources of narrowband RFI. Thus, we limit ourselves to a factor of four in downsampling which is equivalent to a 75% reduction in our data storage.

After we downsample the RFI metrics per beam by a factor of four in frequency, we

¹¹Specifics on the decoding process can be found in Appendix A.1.

¹²Details on the type of file chosen here can be found in Appendix A.2.

further downsample the data by averaging the RFI metrics across the four E-W CHIME cylinders. As shown in Fig. 3.6, the RFI masking fraction behaves similarly across the four E-W cylinders. However, to be certain that our downsampled data represent the true RFI to within a few percent, we perform selective downsampling¹³ in which we keep track of outliers from the average. The average and the outliers are then stored for further analysis. This selective downsampling results in a total data reduction of 57%¹⁴.

Lastly, we fit a 15 degree polynomial to the masking fraction per beam and per frequency. The polynomial fit is performed over six hours of RFI metrics. Each fit is performed per beam and per frequency bin. Five rounds of polynomial fits are implemented to eliminate outliers and improve our final fit¹⁵. When, even after five rounds, the fit is not satisfactory, we store the full resolution data. We show two examples of our polynomial fits in Figs. 3.7 and 3.8. Polynomial fitting further reduces our total data storage by 61% percent¹⁶.

Final Data Format and Storage

We store the final downsampled data in a mongoDB database¹⁷ that is accessible to all CHIME/FRB users. The RFI can easily be reconstructed from this database using the polynomial fit and outlier values.

The original npy files in which the initial full-resolution data are stored are kept for one

¹³See Appendix A.4 for more details on the algorithm behind selective downsampling.

¹⁴This is the data reduction achieved for the already frequency downsampled data.

¹⁵See Appendix A.5 for more specifics on the polynomial fits.

¹⁶This is the data reduction achieved for the already frequency downsampled and E-W downsampled data.

¹⁷Details on mongoDB can be found in Appendix A.6 or at [mongoDB.com](https://www.mongodb.com).

to two weeks post collection in case we want to investigate the metrics at the full resolution or in case there are any problems in downsampling the data. However, after this two week period, the full resolution data are deleted and we only store the downsampled data in the mongoDB.

3.2.3 Benefits Achieved by *rfi-scout*

The *rfi-scout* pipeline leads to a huge reduction in our total data storage while simultaneously recording the L1 RFI metrics on a timescale that satisfies CHIME/FRB's science requirements. Using the *rfi-scout* pipeline, we are able to query the RFI metrics from L1 and store these metrics in under four seconds. Additionally, by downsampling in frequency, downsampling over the E-W columns, and fitting a polynomial, we reduce the total daily storage ¹⁸ by $\sim 96\%$ ¹⁹ (see Table 3.1). *rfi-scout* makes querying and storing the L1 RFI metrics both computationally feasible (e.g. able to query on a 4 second timescale) and sustainable (e.g. producing $\sim 4\text{T}$ of data/year).

¹⁸This is the reduction achieved for the data queried at the four second rate.

¹⁹The data reduction achieved will vary from day to day, as some days may have more extreme and unpredictable RFI environments than others.

	Previously	<i>rfi-scout</i>
Number of Frequency Channels	1024	256
Reduction in Data due to Frequency Binning	0%	75%
Number of Beams	1024	256 + outliers
Reduction in Data due to E-W Downsampling	0%	57%
Number of Time Samples	All	Only outliers
Reduction in Data due to Polynomial Fitting	0%	61%
Total Reduction	0%	96%

Table 3.1: Summary of the improvements made through *rfi-scout* by downsampling in frequency, downsampling over the E-W columns, and fitting a polynomial to the data.

3.3 Future Work for *rfi-scout*

3.3.1 Remaining Work

While the *rfi-scout* pipeline has been written and tested, only querying the L1 RFI metrics and storing them in npy files has successfully been deployed on site. The data reduction has been performed on a local machine. As *rfi-scout* is to be an automatic process operating on site, it is essential to finish deploying this latter half. This will be the main focus of all future work related to *rfi-scout*.

The metrics produced by *rfi-scout* have also yet to be incorporated into system sensitivity metrics or other science data products. Once the pipeline is deployed on site, we will smoothly and automatically incorporate the metrics into the relevant data products.

3.3.2 Areas for Improvement

We would achieve even further reduction in the data storage if we could fit the masking fraction over all beams for a given time bin by a polynomial. However, there is large variation in the masking fraction in the Northern and Southern edge beams, and a polynomial cannot be acceptably fit to the data (see Fig. 3.9). If we fit only beams 58 through 198 (140 beams symmetric about beam 128), then the fit is much more reasonable (see Fig. 3.10), and all residuals are less than 2%. Future work could attempt to work this into the *rfi-scout* pipeline. Additionally, the structure seen in beams 58 through 198 is possibly sufficiently stable to be fit using a pre-determined template. Future work could test whether this is possible.

The frequency binning is currently evenly spaced, with adjacent frequency channels averaged and each bin of equal size. However, there are certain bands (e.g. the LTE band) where the RFI masking is very similar across all frequencies. An additional step would be to explore differing frequency binning where large regions such as the LTE band would be averaged together while other frequency channels might not be.

Lastly, as seen in Fig. 3.7, the RFI masking can exhibit the behaviour of a step function. One could attempt a Bayesian block scheme here to better fit the data.

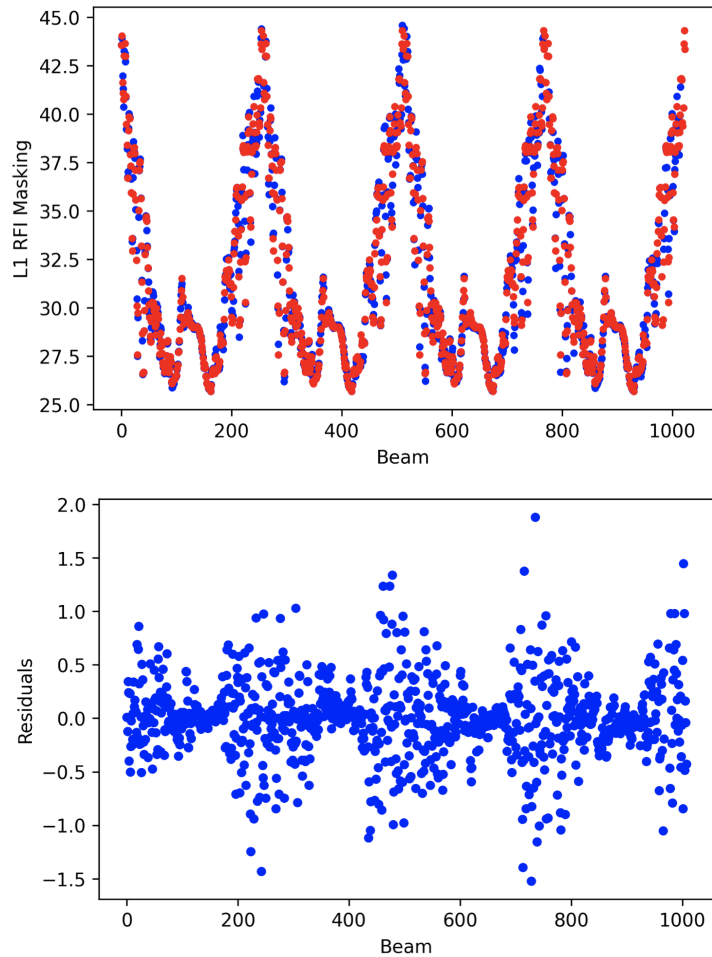


Figure 3.6: Comparison between the masking fraction for all N-S and E-W beams with the masking fraction averaged over all E-W beams from 2021-05-18 to 2021-05-19. The data are also averaged over all frequencies and timestamps. In the top panel, the full-resolution data for all 1024 beams are shown in blue while the average over all E-W columns is shown in red. In the bottom panel, the residuals are shown between the E-W averaged masking fractions and the full-resolution 1024 beam masking fractions.

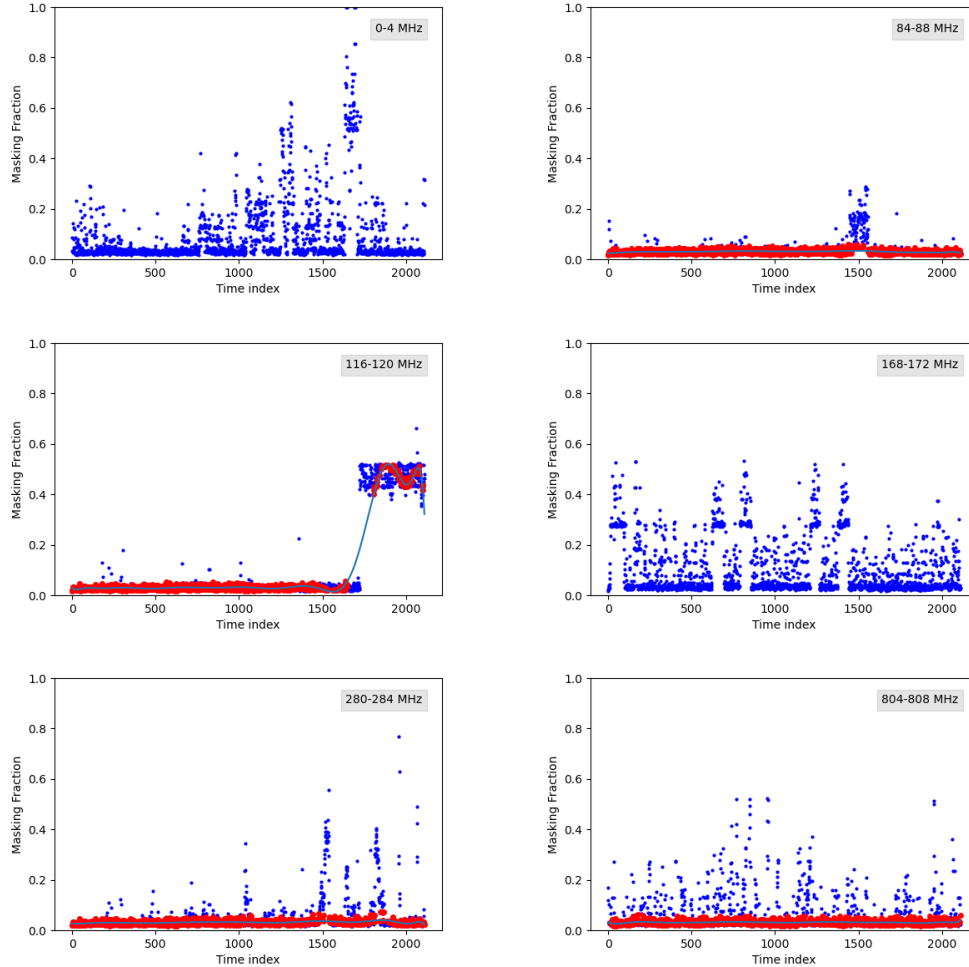


Figure 3.7: Masking fraction as a function of time for N-S beam 3 after averaging over the E-W columns and downsampling in frequency. Each panel shows the RFI metrics for a different four MHz frequency bin with the frequency range indicated in the top right corner of each plot. We show four examples in which the polynomial is a strong fit to the data (less than 50% of the data are outliers) and two examples in which a polynomial could not be satisfactorily fit to the data. In both cases, the blue dots are the initial RFI metrics sampled at a ten second cadence. For the cases in which a polynomial fit is satisfactory, the final fit is shown in blue with the red dots the metrics within 2% of this fit. For the two cases where a polynomial cannot be satisfactorily fit, the fit is not included nor are the red dots within 2% of this fit.

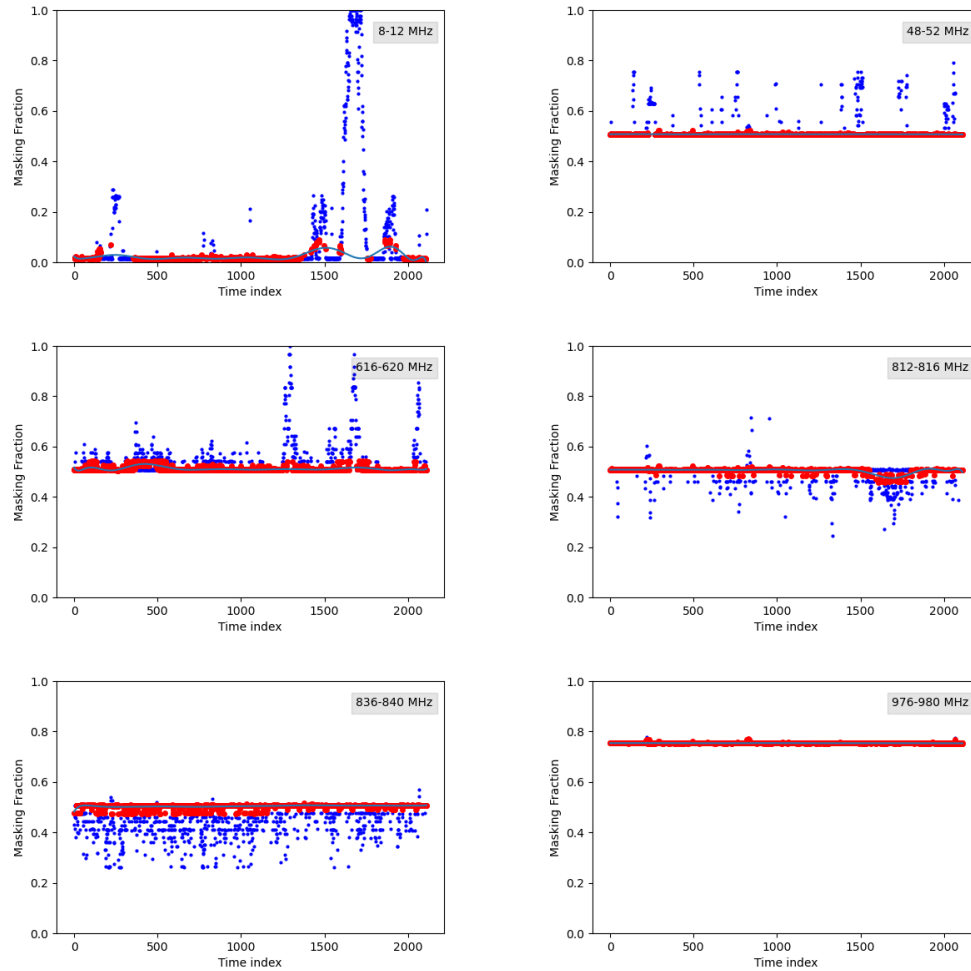


Figure 3.8: Percent masking as a function of time for N-S beam 108 after averaging over the E-W columns and downsampling in frequency. Each panel shows the RFI metrics for a different four MHz frequency bin with the frequency range indicated in the top right corner of each plot. In all six examples, the polynomial is a strong fit to the data (less than 50% of the data are outliers). The blue dots are the initial RFI metrics sampled at a ten second cadence while the final fit is shown in blue with the red dots the metrics within 2% of this fit.

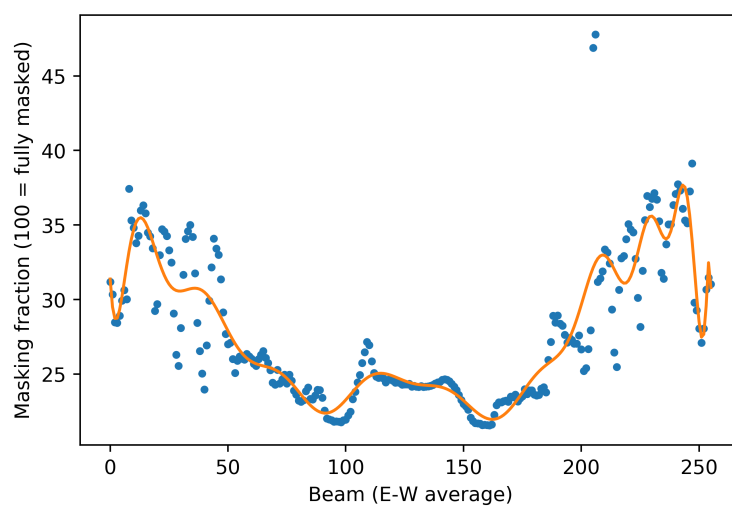


Figure 3.9: Masking fraction as a function of N-S beam number (averaged over the E-W columns) fit using a polynomial. In the edge beams, the difference between the polynomial and the data is as high as $\sim 5\%$.

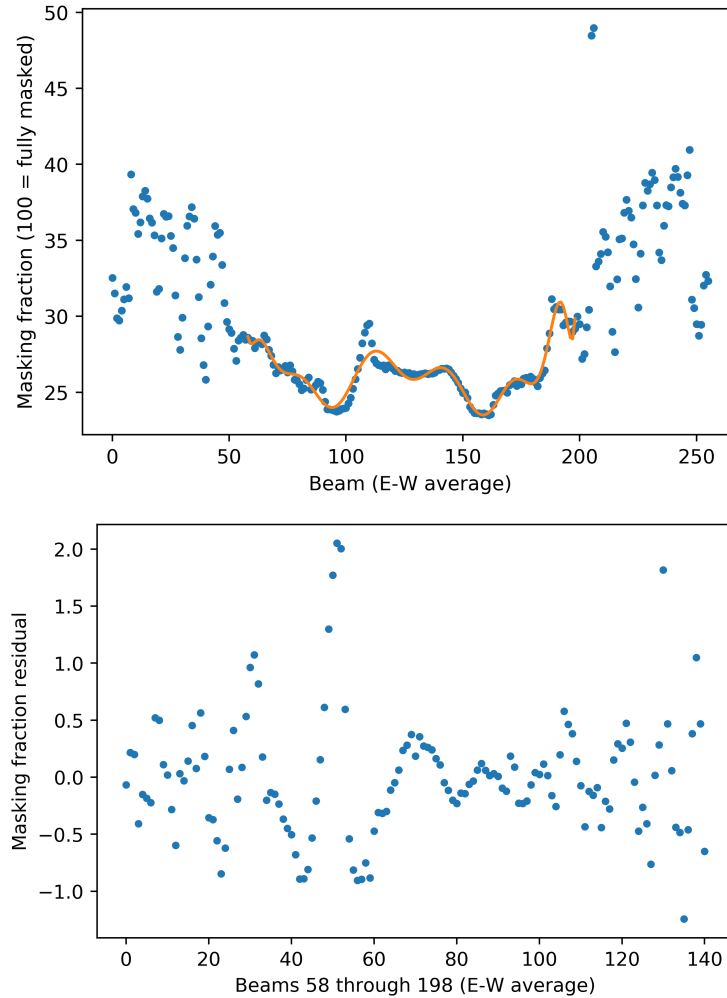


Figure 3.10: Masking fraction as a function of N-S beam number (averaged over the E-W columns) fit using a polynomial. Only beams 58 through 198 are fit with the edge beams ignored. In the top plot, the fit and the data are shown while residuals between the two are shown in the bottom plot.

Chapter 4

Radio Limits for SGR 1935+2154

4.1 Introduction to SGR 1935+2154

SGR 1935+2154 was first detected on 5 July 2014 by the Neil Gehrels *Swift* Observatory¹ [105]. Follow-up observations by the *Swift*, *Chandra*², and *XMM-Newton*³ observatories confirmed the source to be a magnetar located within the Milky Way [106]. In the following two years, it had three other large bursts: one on 22 February 2015, one on 14 May 2016, and one on 18 June 2016 [107]. The bursts between 2014 and 2016 were observed by *Swift*/XRT, *Swift*/BAT, *Chandra*, *XMM-Newton*, *NuSTAR*⁴, and the *Fermi* Gamma-ray Space Telescope⁵. As first presented in an analysis done by Israel et al.

¹See swift.gsfc.nasa.gov for details on the *Swift* observatory.

²See this [link](#) for details on the *Chandra* observatory.

³See this [link](#) for details on the *XMM-Newton* observatory.

⁴See www.nustar.caltech.edu for details on the *NuSTAR* telescope.

⁵See fermi.gsfc.nasa.gov for details on the *Fermi* Gamma-ray Space Telescope.

(2016) [106] using *Chandra* and *XMM-Newton*, the magnetar has a period of 3.24 s with a period derivative of $1.43 \times 10^{-11} \text{ s s}^{-1}$. This can be extrapolated to a surface dipolar magnetic field of $\sim 2.2 \times 10^{14} \text{ G}$ with an age of 3.6 kyr [106].

The distance to the magnetar, however, has still not been well constrained. As noted in Gaensler (2014) [108], SGR 1935+2154 is close to the centre of SNR G57.2+0.8. In 2016, Kothes et al. (2016) [109] presented a detailed radio continuum and linear polarization study of this SNR. They determined the distance to the SNR to be 12.5 kpc, placing it in the outer arm of the Milky Way, and estimated its age to be 41,000 years. Later studies, however, have found distances in the range of ~ 1.5 to 9 kpc for SGR 1935+2154 (e.g. see Zhou et al. (2020) [110], Zhong et al. (2020) [111], Bailes et al. (2021) [112]).

SGR 1935+2154 was also observed using the 305-m William E. Gordon Telescope at the Arecibo Observatory in Puerto Rico [107]. The follow-up observations occurred during March of 2015 and July of 2016 with six observing days of approximately one to three hours of observation per day [107]. However, these were all follow-up observations – none occurred simultaneously with the X-ray detections. The data were searched for both coherent pulsations along with single pulses. No radio emission was found down to $14 \mu\text{Jy}$ at 4.6 GHz and down to $7 \mu\text{Jy}$ at 1.4 GHz [107].

SGR 1935+2154 underwent a prolonged period of quiescence with no detections from the source in 2017 or 2018. It then began a new extended active phase on 4 October 2019 [113]. During both November 2019 and April/May 2020 the source was particularly active with

approximately thirteen reported bursts between 4 November 2019 and 5 November 2019, and hundreds of bursts between April and May of 2020. These bursts were identified by a range of high-energy telescopes such as the Burst Alert Telescope (BAT) onboard *Swift*, the Gamma-ray Burst Monitor (GBM) onboard *Fermi*, the Konus-*WIND* (KW) onboard the NASA GGS-*WIND* spacecraft⁶, the International Gamma-Ray Astrophysics Laboratory (INTEGRAL)⁷, and the Hard X-ray Modulation Telescope (*Insight*-HXMT) Satellite⁸.

4.2 Initial CHIME/FRB Detection of SGR 1935+2154

Before April 2020, SGR 1935+2154 had only been observed in X-ray and high-energy bands with no detected radio emission. However, on 28 April 2020, CHIME/FRB observed an extremely bright burst from the source, providing the first evidence for radio emission from SGR 1935+2154 [8]. This detection (first reported in Atel 13681 [114]), triggered other radio and high-energy telescopes to search for bursts, with the discovery that the STARE2 instrument (Bochenek et al. (2020) [57]), the *Insight*-HXMT telescope (Li et al. (2020) [115]), the Konus-*Wind* experiment (Ridnaia et al. (2020) [116]), the AGILE instrument (Tavani et al. (2020) [117]), and the INTEGRAL satellite (Mereghetti et al. (2020) [118]) had also detected the same burst from SGR 1935+2154.

CHIME/FRB observed two sub-bursts from SGR 1935+2154 with arrival times of

⁶See asd.gsfc.nasa.gov/konus/ for details on Konus-*WIND*.

⁷See sci.esa.int/web/integral for details on INTEGRAL.

⁸See hxmten.ihep.ac.cn for details on *Insight*-HXMT.

14:34:24.42848 and 14:34:24.45745 (UTC, geocentric) as seen in Fig. 4.1. Both sub-bursts were detected in the far sidelobes of CHIME/FRB (apparent in the spectral structure of the bursts), in 93 of the 1024 formed beams. The two bursts had 400 to 800 MHz peak fluxes of 110 and 150 kJy and fluences of 480 and 220 kJy ms, respectively (see Table 1 of CHIME/FRB Collaboration (2020) [8]). The burst was also observed by a 10-m radio dish with a CHIME feed in the Algonquin Provincial Park, Ontario [8].

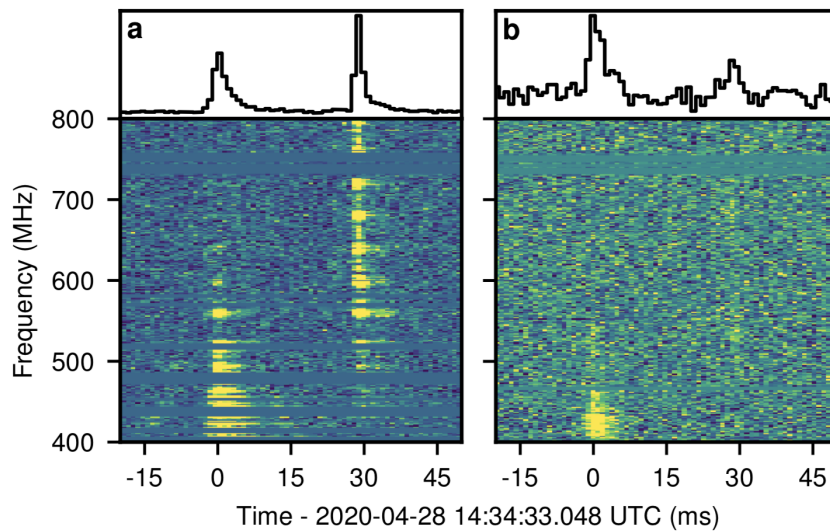


Figure 4.1: Normalized dynamic spectra and band-averaged time-series (geocentric) of the burst from SGR 1935+2154 as detected by a) CHIME/FRB and b) the 10-m dish in the Algonquin Provincial Park. The spectra have a time resolution of 0.98302 ms and frequency resolution of 1.5625 MHz. Figure courtesy of CHIME/FRB Collaboration (2020) [8]

The burst from SGR 1935+2154 on 28 April 2020 provides a unique opportunity to calculate the radio to high-energy flux ratio as simultaneous detections were made in the

radio, X-ray, and gamma-ray energy bands. The burst was identified by the *Konus-Wind* telescope with a 20 to 200 keV flux of 9.1×10^{-6} erg cm² s⁻¹. Using this *Konus-Wind* flux and a CHIME/FRB peak flux of approximately 100 kJy, we calculate a radio to gamma-ray flux ratio of approximately 10^{10} Jy erg⁻¹ cm⁻² s.

4.3 Non-detections by CHIME/FRB of SGR 1935+2154 Bursts Detected by *Swift*/BAT

4.3.1 Upper Limits on Radio Emission

Whether or not all high-energy bursts from SGR 1935+2154, and potentially all magnetars, are accompanied by luminous radio emission is an interesting question, both for magnetar models, and for the possible connection between magnetars and FRBs. However, this typically requires a targeted follow-up of a magnetar to be coincident with a high-energy burst, something very hard to achieve. CHIME/FRB can rather uniquely address this question though due to its large FOV (~ 250 deg²) and transit telescope nature. Thus, we search within the CHIME/FRB database for luminous radio emission coincident with high-energy bursts from SGR 1935+2154. While we do not find any coincident emission, we constrain the level of radio emission to less than a few kJy for seven high-energy bursts from SGR 1935+2154. We also study the spectral properties of the high-energy bursts, and compare these properties, along with the radio to X-ray flux

ratios, to the 28 April 2020 FRB-like burst from SGR 1935+2154. Below, we discuss in detail these upper limits and spectral properties.

While many of the high-energy bursts produced by SGR 1935+1154 between October 2019 and May 2020 were not within CHIME’s FOV, four high-energy bursts from SGR 1935+2154 on 4 November 2019, two bursts on 5 November 2019, and one burst on 14 November 2019 were within the FOV with hour angles less than that of the burst observed on 28 April 2020 [119], [120], [121].

Three of the bursts detected on 4 November 2019 along with the burst on 14 November 2019 were detected by *Fermi*/GBM and will be discussed in Section 4.4. The three other bursts were detected on 4 November 2019 at UTC 01:54:37, 5 November 2019 at UTC 00:08:58, and 5 November 2019 at UTC 01:36:25 by *Swift*/BAT. These three bursts were at CHIME/FRB hour angles of 18.1° , -7.4° , and 14.5° , respectively (see Table 4.1). All three bursts occurred during nominal CHIME/FRB operational periods yet no radio counterparts were detected.

The hour angles for all three events place them in the sidelobes of CHIME/FRB which makes calculating an upper limit on the radio flux difficult. Additionally, to calculate an upper limit on the radio emission from SGR 1935+2154 at a given time, we would ideally have a near-simultaneous and near-on-the-sky FRB from a different source for our flux calibration. However, it is not possible to satisfy both criteria as CHIME/FRB only detects ~ 2 to 3 FRBs per day [2]. Instead, we choose an FRB nearby in declination (e.g. $< 1^\circ$) to SGR

Date (UTC, geocentric)	Hour Angle ($^{\circ}$)	Flux to S/N Ratio (FRB)	Primary Beam Sensitivity Ratio	Formed Beam Sensitivity Ratio	System Sensitivity Ratio	Upper Limit on Radio Emission (kJy)
4 Nov. 2019 at 01:54:37	18.1	0.11 ± 0.03	211 ± 44	5.0	0.99 ± 0.05	1.1 ± 0.4
5 Nov. 2019 at 00:08:58	-7.3	0.11 ± 0.03	73 ± 19	3.8	0.95 ± 0.5	0.3 ± 0.1
5 Nov. 2019 at 01:36:25	14.5	0.11 ± 0.03	104 ± 19	7.1	0.96 ± 0.05	0.8 ± 0.2

Table 4.1: Parameters for calculating radio emission upper limits for three high-energy bursts from SGR 1935+2154 detected by *Swift*/BAT between October 2019 and 28 April 2020. We present the hour angle, flux to S/N ratio, primary beam ratio, formed beam ratio, system sensitivity ratio, and upper limit on the radio counterpart for each burst. The hour angle is calculated assuming an 8.6 second DM delay at 400 MHz. We present the flux to S/N ratio for FRB 20190320C. The primary beam and formed beam ratios are between the responses at the spatial locations of the calibrator FRB and SGR 1935+2154 at the time of the high-energy burst. Note there is no error on the formed beam ratios as these are analytically determined. The system sensitivity is a ratio between the sensitivity of the system on the day the FRB was detected with that for the days of the SGR 1935+2154 bursts. All listed errors are 1σ .

1935+2154 and use models of our beam shape to account for slight differences in position between the two sources.

We do not place constraints on the timestamp of the FRB and instead use system sensitivity metrics to account for temporal differences. These metrics are determined using the daily RMS noise. We do not account for local RFI storms (see Section 3.1.2 for details on such storms) or any other fluctuations in the system sensitivity on a timescale smaller than one day as these metrics were not consistently available. Additionally, while CHIME/FRB is developing a parallel injections system to quantify further aspects of the system's sensitivity to given parameters, this has not yet been applied in this work and as such there may be additional, unknown systematic effects that are not accounted for. However, as discussed by CHIME/FRB Collaboration (2021) [2], the only major thus-discovered bias of CHIME/FRB is against highly scattered bursts. Given the 28 April 2020 burst was not highly scattered, this bias likely does not affect our work.

There is an additional, unaccounted for DM delay between any detection of high-energy emission and the time at which a radio burst would be detected by CHIME/FRB. Given a DM of 332.7 pc cm^{-3} for SGR 1935+2154, we determine an 8.6 second time delay as referenced to 400 MHz between the high-energy emission and a proposed radio detection [8]. The rest of the analysis is performed with this DM delay applied.

Due to the differences in the declination of our calibrator FRB and the high-energy burst, we must account for two different beam sensitivities: that of the primary beam and

that of the formed beams. To map the primary beam, the CHIME team uses Taurus A holography⁹ data in which Tau A is tracked using the DRAO John A. Galt 26-m telescope. These tracks are then correlated with Tau A's transit over CHIME with the only unknown in this correlation the primary beam of CHIME. Averaging multiple tracks creates a clear depiction of the primary beam's amplitude and phase dependence on hour angle for the given source's declination. This method, as it relates to CHIME, is discussed in more detail in Berger et al. (2016) [124]. We eliminate the frequencies with substantial RFI and then average the primary beam holography data over all frequencies (originally sampled every ~ 4 MHz). We note this model for the primary beam model cannot be applied to all sources. However, as Tau A lies at a declination of 22.03° , very similar to that of SGR 1935+2154, the primary beam sensitivity as mapped by Tau A is a good approximation for the primary beam sensitivity for SGR 1935+2154. We calculate the primary beam sensitivity at both the location of SGR 1935+2154 and at the location of the calibrator FRB. We scale the flux of the FRB using the ratio of the two sensitivities.

Besides the primary beam, we must also account for the formed beam sensitivity of CHIME/FRB. As discussed in Section 2.1, CHIME/FRB's formed beams are calculated through an FFT algorithm. We calculate the formed beam sensitivity at the location of our calibrator FRB and at the location of SGR 1935+2154, compute the ratio of the two, and then scale the flux of the FRB accordingly.

⁹For the fundamentals of holography, see Thompson, Moran, & Swenson (2001) [122] and Baars & Swenson (2008) [123].

We assume, conservatively, that CHIME/FRB is sensitive to bursts with a S/N threshold of 10. We can then scale the flux to S/N ratio of our calibrator FRB to a S/N of 10. Combining the calibrator FRB's flux to S/N ratio, the system sensitivities, and the beam sensitivities, the upper limit on the radio flux in the 400 to 800 MHz CHIME/FRB band is given by:

$$Flux_{1935} = 10 \times \frac{Flux_{FRB}}{S/N_{FRB}} \times \frac{B_{FRB}}{B_{1935}} \times \frac{F_{FRB}}{F_{1935}} \times \frac{S_{1935}}{S_{FRB}}, \quad (4.1)$$

where B is the primary beam response, F is the formed beam response, and S is the system sensitivity¹⁰.

We use three FRBs for flux calibration: FRB 20181226D, FRB 20190320C, and FRB 20181223B at declinations of 22.15° , 22.4° , and 21.6° with fluxes of 1.5 ± 0.7 , 1.2 ± 0.3 , and 0.6 ± 0.3 Jy, respectively [2]. The S/N ratios of the bursts are 24.1, 11.3, and 13.03 so the FRBs have flux to S/N ratios of 0.06 ± 0.03 Jy, 0.11 ± 0.02 Jy, and 0.05 ± 0.02 Jy, respectively. While we use all three FRBs to calibrate our system, we only present the limits for the FRB that yields the most conservative radio upper limits, FRB20190320C. Using Eq. 4.1 for the X-ray burst from SGR 1935+2154 on 4 November at UTC 01:54:37, we determine a conservative upper limit on the radio burst flux in the 400 to 800 MHz range of < 2.3 kJy (99% confidence). For the two bursts on 5 November at UTC 00:08:58 and UTC 01:36:25, we determine conservative upper limits on the radio burst fluxes of < 0.6 kJy and < 1.4

¹⁰The system sensitivity is determined by relative RMS noise, so a higher value for the system sensitivity means we were less sensitive on that day, thus the ratio is flipped for this one quantity.

kJy, respectively (99% confidence). The uncertainties on the upper limits are dominated by those on the flux of the calibrator FRB but are also determined using the uncertainties on our primary beam model and system sensitivity. Depending on which FRB we use for calibration, the ratios and upper limits are slightly different. In Table 4.1 we list the most conservative results. We note these three radio limits were also published in CHIME/FRB Collaboration (2020) [8].

4.3.2 Analysis of High-Energy Emission

In addition to determining an upper limit on the radio emission for the three high-energy bursts detected by *Swift*/BAT, we also determine the X-ray flux for two bursts on 5 November 2019. The *Swift*/BAT burst at 01:54:37 on 4 November was much weaker than the two *Swift*/BAT bursts on 5 November and we could not determine a reliable X-ray flux for this burst.

BAT is part of the *Swift* mission launched in 2004 by NASA [125]. BAT was originally deployed to help identify and study gamma-ray bursts. It has a large, 1.4 steradian FOV and as such can monitor a large part of the sky. Within minutes of a burst in its FOV, BAT can determine the position of the source to within four arcminutes [125]. Depending on the merits of the burst, BAT will then trigger a slew of *Swift* to the source so it can be followed up by the two other instruments onboard *Swift*: the X-ray Telescope (XRT) and the Ultraviolet/Optical Telescope (UVOT).

Data products for the bursts on 5 November 2019 at UTC 00:08:58 and UTC 01:36:25 were both pre-processed by the *Swift* team using the *batgrbproduct* code¹¹ with the final products publicly available online. The program *batgrbproduct*, added to the BAT software package in 2006, performs basic GRB analysis using standard BAT calibration tools and the Tracking and Data Relay Satellite System (TDRSS) burst position message. It produces light curves, spectra, detector images, sky images, and some auxiliary files for a given burst.

To confirm the two bursts, we examine the pre-slew sky coordinate images (produced and available online by the *Swift* team using *batgrbproduct*) for both bursts, shown in Figs. 4.2 and 4.3. For the burst on 5 November 2019 at UTC 00:08:58, Ambrosi et al. (2019a) [120] reported the count rate to reach a maximum of 19,000 counts per second while for the burst on 5 November 2019 at UTC 01:36:25, Ambrosi et al. (2019b) [121] reported the count rate to reach a maximum of 130,000 counts per second. However, the X-ray flux for both bursts is comparable. The maximum count rate for each burst is likely limited by the location of SGR 1935+2154 within BAT's FOV e.g. the burst at UTC 00:08:58, shown in Fig. 4.2, is located at the edge of BAT's FOV while the burst at UTC 01:36:25, shown in Fig. 4.3, is located near the centre of BAT's FOV.

We analyze the processed BAT data for 5 November 2019 using Version 12.10.1f of HEASARC's XSPEC program [126]. To generate a spectrum, we use the spectra and response files as already processed by the *Swift* team using *batgrbproduct* for the entire

¹¹See [this link](#) for details on the *batgrbproduct* code.

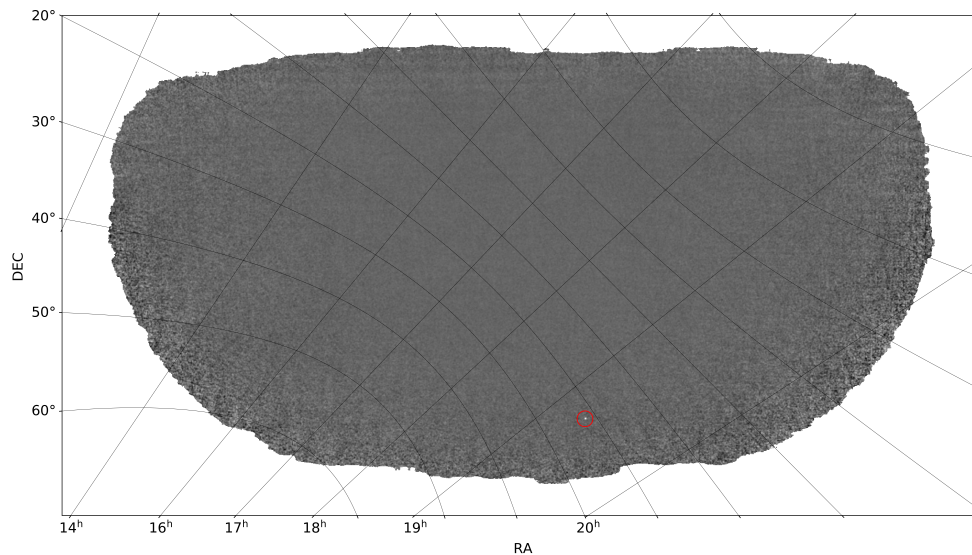


Figure 4.2: Sky image of BAT’s FOV during a burst from SGR 1935+2154 at UTC 00:08:58 on 5 November 2019. The burst is located towards the lower, central edge of BAT’s FOV and is circled in red. BAT was pointed at $(RA, DEC) = (260.4^\circ, 11.6^\circ)$ during the time of the burst. The sky image is shown in the world coordinate system with arcs tracing out lines of constant right ascension and declination. The colour scale is linearly proportional to the sky flux with a white pixel having a higher flux than a black pixel.

burst duration. *Swift*/BAT is sensitive to photons in the range of 15 to 150 keV so we fit the data between 15 and 150 keV using three different models: 1. a single blackbody (BB), 2. a BB plus power-law (PL) (no PL cutoff), and 3. two BBs. For all three models, we fix the equivalent neutral hydrogen absorption column density N_H to $1.6 \times 10^{22} \text{ cm}^{-2}$, although at these energies the N_H does not contribute significantly to our analysis¹².

The burst on 5 November 2019 at UTC 00:08:58 is best fit using two BB components

¹²This N_H value is chosen based on the results of the spectral analysis performed by Israel et al. (2016) [106].

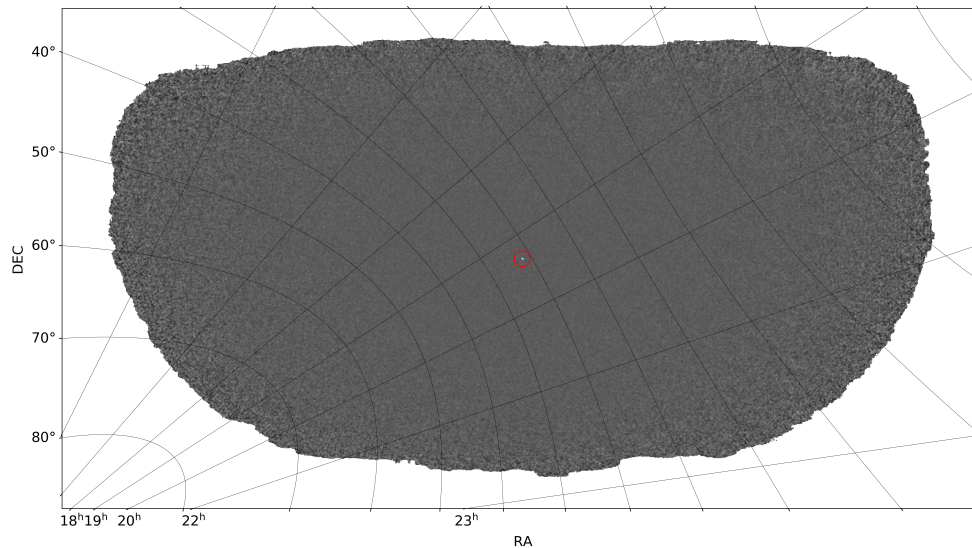


Figure 4.3: Sky image of BAT’s FOV during a burst from SGR 1935+2154 at UTC 01:36:25 on 5 November 2019. The burst is located towards the lower left centre of BAT’s FOV and is circled in red. BAT was pointed at $(\text{RA}, \text{DEC}) = (293.8^\circ, 21.9^\circ)$. The sky image is shown in the world coordinate system with arcs tracing out lines of constant right ascension and declination. The colour scale is linearly proportional to the sky flux with a white pixel having a higher flux than a black pixel.

with temperatures of 9.4 ± 0.7 and 3.7 ± 0.8 keV. The data, model, and residuals are shown in Fig. 4.4 with fit parameters given in Table 4.2. We find a reduced χ^2 of 1.01 for this model with a 15 to 150 keV flux of $8.6_{-0.7}^{+0.4} \times 10^{-7} \text{ erg cm}^{-2} \text{ s}^{-1}$ (68% confidence region). We also use our model to extrapolate the spectrum to 20 to 200 keV so we can compare the flux with that of the 28 April 2020 detection by *Konus-Wind*. We find a 20 to 200 keV flux of $6.6_{-0.6}^{+0.3} \times 10^{-7} \text{ erg cm}^{-2} \text{ s}^{-1}$. We also try a single BB and a BB plus PL. Both fits perform slightly worse with the BB yielding a reduced χ^2 of 1.3 and the BB plus PL model yielding

Date (UTC, geocentric)	Model	BB ₁ (keV)	Norm ₁	BB ₂ (keV)	Norm ₂	χ^2	Flux (15-150 keV) (erg cm ⁻² s ⁻¹)	Flux (20-200 keV) (erg cm ⁻² s ⁻¹)
5 Nov. 2019 at 00:08:58	2 BB	9.4 ± 0.7	7.7 ± 1.4	3.7 ± 0.8	8.7 ± 2.3	1.05	8.6 ^{+0.3} _{-0.7} × 10 ⁻⁷	6.6 ^{+0.4} _{-0.4} × 10 ⁻⁷
5 Nov. 2019 at 01:36:25	2 BB	13.8 ± 1.8	5.1 ± 1.4	6.6 ± 0.6	9.1 ± 1.2	0.79	9.8 ^{+0.2} _{-0.3} × 10 ⁻⁷	8.4 ^{+0.2} _{-0.3} × 10 ⁻⁷

Table 4.2: High-energy emission fit parameters for two bursts from SGR 1935+2154 detected by *Swift*/BAT on 5 November 2019 at UTC 00:08:58 and UTC 01:36:25. We present the model used (BB = blackbody), the BB temperatures, BB normalizations, the χ^2 for the model, and both the 15 to 150 keV and 20 to 200 keV fluxes. All listed errors are 1σ .

a reduced χ^2 of 1.4.

The burst on 5 November 2019 at UTC 01:36:25 is also fit using two BBs with temperatures of 13.8 ± 1.7 and 6.6 ± 0.6 keV. The data, model, and residuals are shown in Fig. 4.5 with fit parameters given in Table 4.2. The reduced χ^2 for this fit is 0.79 with a 15 to 150 keV flux of $9.8^{+0.2}_{-0.3} \times 10^{-7}$ erg cm⁻² s⁻¹ which can be extrapolated to a 20 to 200 keV flux of $8.4^{+0.2}_{-0.3} \times 10^{-7}$ erg cm⁻² s⁻¹. The data are also well fit by a BB plus PL with a reduced χ^2 of 0.75 for a BB with a temperature of 8.6 ± 0.4 keV and a PL with a photon index of 2.5 ± 0.2 . However, the 15 to 150 keV flux is not contained within its 68% confidence range so we do not use this model for our final, reported values. As noted on the HEASARC website, this can occur if the parameter space for the fit (the BB and PL parameters in this case) is very complicated as the estimates used to obtain the flux may no longer be valid¹³. We also fit the burst using just a single BB but the fit is worse with a reduced χ^2 of 1.5.

¹³See this [link](#) for further details on this problem.

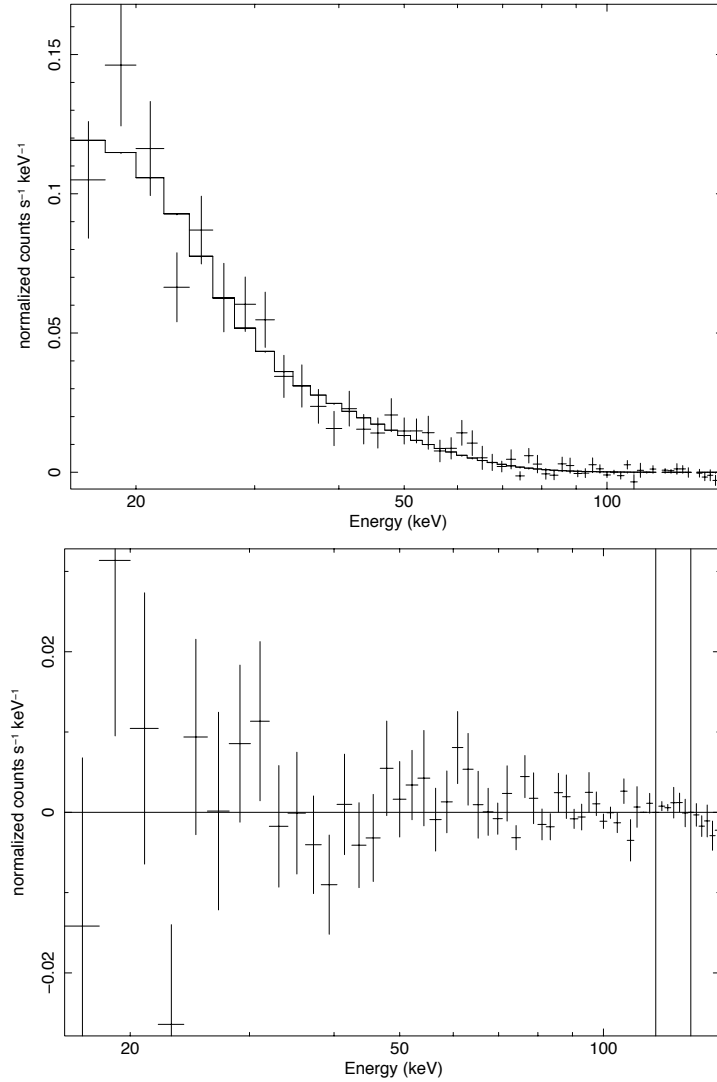


Figure 4.4: Burst by SGR 1935+2154 on 5 November 2019 at UTC 00:08:58 detected by *Swift*/BAT [121]. In the top panel, the normalized counts per second and per channel is shown as function of channel number with channels 5 through 40 corresponding to energies 15 through 100 keV. The best fit model using two BBs with temperatures of 9.8 and 3.9 keV is also shown in the top panel. The residuals between the model and the data are shown in the bottom panel.

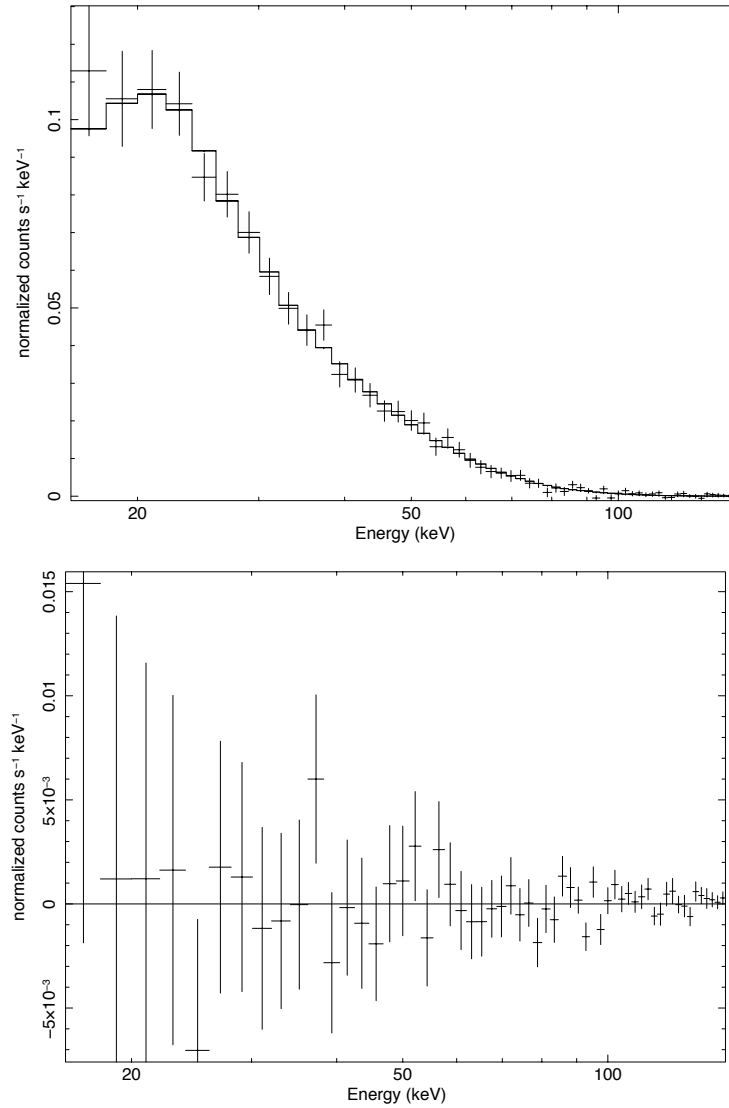


Figure 4.5: Burst by SGR 1935+2154 on 5 November 2019 at UTC 01:36:25 detected by *Swift*/BAT [121]. In the top panel, the normalized counts per second and per channel is shown as function of channel number with channels 5 through 40 corresponding to energies 15 through 100 keV. The best fit model using two BBs with temperatures of 12.0 and 6.0 keV is also shown in the top panel. The residuals between the model and the data are shown in the bottom panel.

4.3.3 Comparison of Bursts

The spectral features for the two bursts on 5 November 2019 are similar to those of past detections of SGR 1935+2154 with *Fermi*/GBM and *Swift*/BAT. Lin et al. (2020a) [127] analyzed 127 bursts detected by *Fermi*/GBM and *Swift*/BAT from SGR 1935+2154 from its four active periods between 2014 and 2016. Of the 127 bursts, they were able to fit 80 using two BBs. They fit the distribution of cold and hot BB temperatures with two Gaussians for a mean cold BB temperature of 4.4 ± 0.1 keV and a mean hot BB temperature of 11.3 ± 0.4 keV. These results are similar to the findings of van der Horst et al. (2021) [128] and Lin et al. (2011) [129] for two other magnetars.

The spectral properties of the two 5 November 2019 bursts are not consistent with those from the 28 April 2020 burst. The 28 April 2020 burst as detected by CHIME/FRB was also detected by *Integral* and *Konus-Wind*. Both *Integral* and *Konus-Wind* reported cold BB temperatures of ~ 11 keV and hot BB temperatures of ~ 30 keV, three times higher than those from the 5 November 2019 bursts, for energy bands of 32 to 300 keV and 20 to 200 keV, respectively [118], [116]. Additionally, the burst on 28 April 2020 was significantly harder than the earlier bursts from this source with peak energies of 65 keV for *Integral* and 85 keV for *Konus-Wind*, respectively. As discussed in Lin et al. (2020a) [127], the 127 bursts from SGR 1935+2154 during its active periods between 2014 and 2016 had a mean peak energy of 30.4 keV, significantly lower than the 28 April 2020 bursts.

The 5 November 2019 bursts at UTC 00:08:58 and UTC 01:36:25 had X-ray fluxes in the

Date (UTC, geocentric)	Hour Angle ($^{\circ}$)	Upper Limit on Radio Emission (kJy)	High-energy Flux ($\text{erg cm}^{-2} \text{s}^{-1}$)	Radio to high-energy Flux Ratio ($\text{kJy erg}^{-1} \text{cm}^2 \text{s}$)
4 Nov. 2019 at 01:54:37	18.1	2.3	n/a	n/a
5 Nov. 2019 at 00:08:58	-7.3	0.6	$6.7^{+0.3}_{-0.6} \times 10^{-7}$	$9.0^{+0.4}_{-0.8} \times 10^5$
5 Nov. 2019 at 01:36:25	14.5	1.4	$8.3^{+0.2}_{-0.2} \times 10^{-7}$	$8.4^{+0.2}_{-0.2} \times 10^5$

Table 4.3: Hour angle (8.6 second DM delay at 400 MHz accounted for), upper limit on radio emission, X-ray flux (if data available and accessible), and radio to X-ray flux ratio for each burst from SGR 1935+2154 within CHIME/FRB FOV's from *Swift*/BAT from October 2019 until 28 April 2020. All upper limits on the radio emission are reported at the 99% confidence level. The errors on the X-ray fluxes and the radio to high-energy flux ratios are 1σ .

20 to 200 keV range that were 14 and 11 times, respectively, smaller than the flux reported by *Konus-Wind* on 28 April 2020 of $9.1 \times 10^{-6} \text{ erg cm}^{-2} \text{ s}^{-1}$. However, the upper limits on the radio fluxes for the 5 November 2019 bursts were approximately 220 and 90 times smaller than the flux of the burst detected by CHIME/FRB on 28 April 2020. Thus, the radio to X-ray flux ratios for these 5 November 2019 events were at least 15 and 8 times smaller, respectively, than for the 28 April 2020 event (see Table 4.3).

4.4 Non-detections by CHIME/FRB of SGR 1935+2154 Bursts Detected by *Fermi*/GBM

4.4.1 *Fermi*/GBM Telescope

In addition to the recent bursts detected by *Swift*/BAT, over one hundred bursts from SGR 1935+2154 were detected by *Fermi*/GBM in 2019 and 2020. *Fermi* is a low-orbit space

telescope detecting gamma-rays in the energy range of 10 keV to 300 GeV. *Fermi*'s main instrument is the Large Area Telescope (LAT) which has a FOV of 2.4 steradians and can detect gamma-rays in the energy range of 20 MeV to 300 GeV (see Atwood et al. (2009) [130] for more details on the LAT). *Fermi* also consists of a Gamma-ray Burst Monitor (GBM) which operates in a lower energy range of ~ 8 keV to 40 MeV and has a much larger FOV than the LAT, viewing the entire unocculted sky [131]. *Fermi*/GBM's main science goals are to detect lower energy emission from events detected by LAT and to re-orient *Fermi* upon detection of bright bursts so the LAT can detect any delayed high-energy emission [131]. On average, *Fermi*/GBM detects ~ 250 GRBs per year.

Between 4 October 2019 and 10 May 2020, *Fermi*/GBM detected 181 triggered and untriggered bursts from SGR 1935+2154¹⁴. Having detected coincident radio and high-energy emission in the past from SGR 1935+2154 (e.g. 28 April 2020 burst), we look for any FRBs coincident with the 181 detections by *Fermi*/GBM. Below, we detail an investigation into first searching the CHIME/FRB database for all 181 bursts and then calculating upper limits on the radio emission for bursts above CHIME/FRB's FOV in a manner similar to that done in Section 4.3.1.

¹⁴After detection of a burst, *Fermi*/GBM has ~ 10 minutes before it can trigger on another burst. Untriggered bursts refer to events not originally triggered on, but later detected in other search algorithms.

4.4.2 Searching the CHIME/FRB Database for Radio Counterparts

We search the entire CHIME/FRB L4 database including known sources, RFI, and unknown sources, for radio counterparts to the 181 *Fermi*/GBM detections of SGR 1935+2154. The event times are provided with reference to the *Fermi* satellite location, but as the *Fermi* satellite is in a low-Earth orbit, the time offset when converting from the *Fermi* satellite time to topocentric time at CHIME is small so we perform all calculations using the arrival times of the bursts at the *Fermi* satellite. We do, however, add an additional 8.6 second delay to all arrival times to account for the maximum DM delay in the 400 to 800 MHz band at CHIME for SGR 1935+2154 (assuming a DM of 332.7 pc cm^{-3} as given by CHIME/FRB Collaboration (2020) [8]).

We search within the CHIME/FRB database for any possible radio detections within a 60 second time window around the dispersion-corrected arrival times at the *Fermi* satellite (30 seconds before and 30 seconds after the arrival time). We also search within a 20 pc cm^{-3} DM range from SGR 1935+2154's DM of 332.7 pc cm^{-3} . We then compare the locations of any events within the CHIME/FRB database that fit these criteria to that of SGR 1935+2154 to determine if any of the detections might be due to this source. We note that for 180 of the 181 bursts, the *Fermi*/GBM burst durations are less than two seconds so the sixty second window is much larger than the burst duration. However, for one burst from *Fermi*/GBM, the duration is approximately eleven seconds and so we set the time window to 70 seconds

around the arrival time of this burst.

We perform our time and DM search in the CHIME/FRB database for two types of events:

1. all events not classified as RFI and
2. all events classified as RFI.

After identifying all possible events that fit the time and DM criteria, we compare the location of these events to the arc that SGR 1935+2154 traces on the sky as it transits above CHIME. In the top panel of Fig. 4.6 we plot the arc of SGR 1935+2154 for a maximum E-W zenith angle (relative to CHIME's meridian) of 30° along with all events from the L4 database (not classified as RFI) within the DM and time range specified above in blue. No events are coincident with the arc of SGR 1935+2154. In the bottom panel of Fig. 4.6 we perform the same analysis but instead focus on events classified as RFI. There are, again, no events coincident with the arc of SGR 1935+2154.

In addition to searching for all events within the CHIME/FRB database that occurred within the specified DM and time range, we also investigate all events within the database coincident with the arc of SGR 1935+2154 in case an event occurred just outside the minute time frame of our search. We investigate all events along the arc of SGR 1935+2154 with a DM range of $332.7 \pm 20 \text{ pc cm}^{-3}$. 13 such events fit the criteria, all with $S/N < 8$ except for the burst on 28 April 2020 published in CHIME/FRB Collaboration (2020) [8]. However, there is a high chance probability of having 13 coincident non-SGR events with $S/N < 8$ so it is probable that none of these are bursts from SGR 1935+2154. Nonetheless, we manually compare the arrival times of these 13 events to those of the *Fermi*/GBM

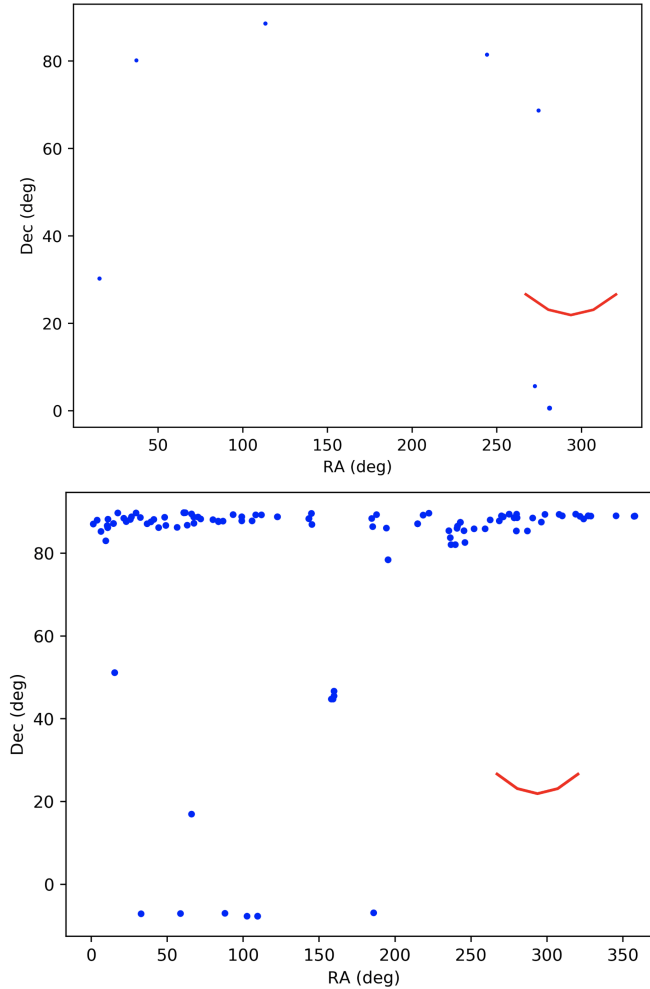


Figure 4.6: All CHIME/FRB events that occurred within 60 seconds of the 181 *Fermi*/GBM detections of SGR 1935+2154 between 10 October 2019 and 10 May 2020. Non-RFI events are shown in the top panel while RFI events are shown in the bottom panel. All event DMs are between 312.7 and 352.7 pc cm^{-3} . All CHIME/FRB events are shown in blue with the marker size proportional to the S/N of the burst. We set a minimum value for the marker size that corresponds to a S/N of 6. Note that the scaling between marker size and S/N is different for RFI and non-RFI events. The arc traced by SGR 1935+2154 as it transits above CHIME/FRB is shown in red.

events. Two of the 13 events occur on the same day as a *Fermi*/GBM event. However, both events occur approximately two hours after the *Fermi*/GBM burst. We conclude that there are no simultaneous detections of SGR 1935+2154 between CHIME/FRB and *Fermi*/GBM between 4 October 2019 and 10 May 2020.

4.4.3 Upper Limits on Radio Emission

Next, we determine upper limits on the radio emission for all high-energy *Fermi*/GBM bursts within CHIME’s FOV. We correct the initial *Fermi* satellite times for DM delays but do not account for the time delay between the *Fermi* satellite time and topocentric time as it is negligible for this analysis. Of the 181 bursts, four are within the FOV of CHIME at their *Fermi*/GBM burst start time: bursts at 01:20:24, 23:16:49, and 23:48:01 UTC on 4 November 2019 along with a burst at 00:30:46 UTC on 14 November 2019 (with the times referenced to the *Fermi* satellite). For the analysis below, we add an 8.6 second DM delay to the arrival times to account for the delay between the high-energy detection times and the time at which the bursts would have been detected by CHIME/FRB. We note that an upper limit on the radio counterpart to the burst at 01:20:24 UTC was published in CHIME/FRB Collaboration (2020) [8].

The bursts are at hour angles of 9.5° , -21.3° , -13.5° , and 7.7° , respectively (see Table 4.4 for burst hour angles within the CHIME FOV). We perform an analysis similar to that explained in Section 4.3.1 to calculate upper limits on the radio emission associated with these

<i>Fermi</i> /GBM Date (UTC)	Hour Angle ($^{\circ}$)	Flux to S/N Ratio for FRB	Primary Beam Response Ratio	Formed Beam Response Ratio	System Sensitivity Ratio	Upper Limit Radio Emission (kJy) (1σ)
4 Nov. 2019 at 01:20:24	9.5	0.11 ± 0.03	90 ± 20	8	0.99 ± 0.04	0.8 ± 0.3
4 Nov. 2019 at 23:16:49	-21.3	0.11 ± 0.03	240 ± 50	9	0.96 ± 0.05	2.3 ± 0.8
4 Nov. 2019 at 23:48:01	-13.5	0.11 ± 0.03	70 ± 10	9	0.96 ± 0.05	0.7 ± 0.2
14 Nov. 2019 at 00:30:46	7.7	0.11 ± 0.03	90 ± 20	4	0.95 ± 0.5	0.4 ± 0.2

Table 4.4: Parameters for calculating radio emission upper limits for four high-energy bursts from SGR 1935+2154 detected by *Fermi*/GBM. We list the hour angle, flux to S/N ratio, primary beam ratio, formed beam ratio, system sensitivity ratio, and upper limit on a radio counterpart for each burst. The *Fermi*/GBM date does not account for the 8.6 second time delay but is instead the original arrival time at the *Fermi* satellite. The hour angle is calculated using the predicted arrival time of the burst at CHIME/FRB assuming an 8.6 second DM delay at 400 MHz. We present the flux to S/N ratio for FRB 20190320C. The primary beam and formed beam ratios are between the responses at the spatial locations of the calibrator FRB and SGR 1935+2154 at the time of the high-energy burst. Note there is no error on the formed beam ratios as these are analytically determined. The system sensitivity is a ratio between the sensitivity of the system on the day the FRB was detected with that for the days of the SGR 1935+2154 bursts.

high-energy bursts. We use the ratio between the magnitude of the primary beam response, formed beam response, and system sensitivity at the locations of our calibrator FRBs (the same as those used in Section 4.3.1) with those for the locations of SGR 1935+2154 during the high-energy outbursts. We list these ratios in Table 4.4. We determine conservative upper limits on the radio burst flux densities in the 400 to 800 MHz range of < 1.7 kJy, < 4.7 kJy, < 1.3 kJy, and < 1.0 kJy for the four events at the 99% confidence level (see Table 4.4). These limits are the same order of magnitude as the radio limits for the *Swift*/BAT bursts presented in Table 4.1.

The high-energy analysis of these bursts is performed by Lin et al. (2020b) [132]. They analyze 148 *Fermi*/GBM bursts from SGR 1935+2154 between 2019 and 2020. They do not analyze a forest of bursts from 27 April 2020 as this was the first forest of bursts ever detected from SGR 1935+2154 and so warrants its own analysis. For the bursts on 4 November at UTC 01:20:24, 23:16:49, 23:48:01 and the burst on 14 November at UTC 00:30:46, the high-energy fluences in the 8 to 200 keV range are $1.05 \pm 0.06 \times 10^{-7}$ erg cm⁻², $0.25 \pm 0.03 \times 10^{-7}$ erg cm⁻², $3.07 \pm 0.11 \times 10^{-7}$ erg cm⁻², and $0.24 \pm 0.04 \times 10^{-7}$ erg cm⁻², respectively. Unfortunately, *Fermi*/GBM did not detect bursts from SGR 1935+2154 on 28 April 2020. Thus, we cannot make a comparison between the radio to gamma-ray energy for the 28 April 2020 with the bursts from 4 November and 15 November 2019.

Lin et al. (2020b) [132] does, however, comment on the BB temperatures and peak energies of the *Fermi*/GBM bursts from SGR 1935+2154 during the 2019 and 2020 outbursts as compared to the earlier outbursts presented in Lin et al. (2020a) [127] (which we referred to in Section 4.3.3). 90 of the 148 bursts are well fit with a double BB with low and high temperatures of 4.5 ± 0.1 keV and 10.7 ± 1.3 keV, consistent with the results from the 2014 to 2016 bursting period. The remaining 56 bursts¹⁵ are fit using an exponentially cutoff PL model (called COMPT¹⁶). The mean photon index for these bursts is $\Gamma = -0.06$ with a peak energy of 27 keV. This is within one sigma of the peak energy of 30 to 35 keV from the 2014 to 2016 bursting period. Lin et al. (2020b) [132] does note a slight decrease in the

¹⁵Two bursts are not well fit by either model.

¹⁶See Lin et al. (2020b) [132] for details on this model.

peak energy (assuming a distance of 9 kpc to SGR 1935+2154) along with an increase in the burst durations between the 2014 to 2016 outbursts and the 2019 and 2020 outbursts.

While *Fermi*/GBM did not detect a burst from SGR 1935+2154 coincident with the 28 April 2020 radio detection, Lin et al. (2020b) [132] still provides a comparison between the hard X-ray burst detected by *Insight*-HMXT on 28 April 2020 and their sample of 148 bursts [115]. The burst detected by *Insight*-HMXT has a peak energy of 37 keV, 10 keV greater than the average for the 2019 and 2020 bursts. The spectrum for the FRB associated X-ray burst is also significantly steeper at $\Gamma = -1.5$ while the 2019 and 2020 bursts have $\Gamma = -0.06$ ¹⁷. The higher peak energy and steeper spectrum suggest a different environment for the production of the hard X-ray associated with the FRB and the other bursts from SGR 1935+2154. The authors of Lin et al. (2020b) [132] suggest a thermal region with a high plasma density for the high-energy bursts not associated with FRB-like emission. This region would not be conducive to radio emission.

4.5 Summarizing Non-Detections by CHIME/FRB of X-ray and High-energy SGR 1935+2154 Bursts

On 28 April 2020, SGR 1935+2154 emitted an extremely bright radio burst consisting of two sub-bursts with fluxes of 110 and 150 kJy. Here, we examine whether past X-ray and

¹⁷In the COMPT model, the flux is proportional to the energy raised to the Γ rather than the energy to the negative Γ .

high-energy bursts from SGR 1935+2154 emitted similar radio bursts. More specifically, we look at past bursts detected by *Swift*/BAT and *Fermi*/GBM. We do not find any coincident, CHIME/FRB radio emission with any of the examined bursts. However, there are seven bursts which are above the horizon at CHIME/FRB at the time of either their X-ray or high-energy emission, allowing us to place constraints on the accompanying radio emission. For all seven bursts, the radio flux constraints are less than a few kJy, which is ~ 100 times less than the radio fluxes of the 28 April 2020 sub-bursts.

We also examine in detail two of the X-ray bursts detected by *Swift*/BAT from 5 November 2019. Their X-ray fluxes in the 20 to 200 keV range are 14 and 11 times smaller than the flux reported by *Konus-Wind* for the 28 April 2020 burst. Thus, after combining these with their radio emission limits, the radio to X-ray emission ratios for these two *Swift*/BAT bursts are ~ 5 and 8 times smaller than that for the 28 April 2020 event. The black body temperatures of these bursts are also approximately three times lower than the temperatures reported by *Integral* and *Konus-Wind* for the 28 April 2020 burst.

For the *Fermi*/GBM bursts, the high-energy analysis is performed by Lin et al. (2020b) [132]. Lin et al. (2020b) [132] found that the 28 April 2020 burst has a significantly steeper spectrum, and peaks at a higher energy than past SGR 1935+2154 bursts detected in 2019 and 2020.

It is clear that the burst on 28 April 2020 from SGR 1935+2154 is different from the previous *Swift*/BAT and *Fermi*/GBM bursts during its 2014 to 2016 and 2019 to 2020 active

period. As derived from both this analysis and the previous analysis of others, the 28 April 2020 bursts has higher BB temperatures for approximately the same energy band, a larger peak energy, a steeper spectrum, and a larger radio to X-ray flux ratio.

Chapter 5

Conclusion

In this thesis, we discuss two projects relating to CHIME/FRB. First, we present a new pipeline, *rfi-scout*, for recording RFI metrics for the CHIME/FRB project on a four second cadence. Querying on such a short timescale, however, results in a significant increase in the total data storage required. We overcome this by downsampling the data in frequency, downsampling over the E-W CHIME columns, and fitting a polynomial to the data. CHIME/FRB RFI metrics have only once been incorporated into scientific projects (e.g. Josephy et al. (2021) [62] uses metrics produced through this thesis to estimate CHIME/FRB's bandwidth), but no other rate or repetition statistics have yet to incorporate the RFI statistics. This is largely due to inconsistent recordings of the RFI metrics and inaccessibility to these metrics. *rfi-scout* will be an automatic process running 24/7 with the end products easily accessible by all CHIME/FRB users. This new pipeline

and its resulting metrics will have large implications not only for monitoring CHIME/FRB's system sensitivity but also for multiple CHIME/FRB science projects.

We also present upper limits on possible radio emission accompanying high-energy bursts from SGR 1935+2154, a magnetar well-known for producing an FRB-like burst on 28 April 2020. We can constrain the radio emission for seven high-energy bursts from SGR 1935+2154 to less than a few kJy. Three of the bursts are detected by *Swift*/BAT while four are detected by *Fermi*/GBM. For two of the three bursts detected by *Swift*/BAT, we also calculate radio to X-ray flux ratios and find they are 15 and 8 times smaller than the ratio of the radio to X-ray emission from the FRB-like burst. This suggests that not all X-ray bursts are accompanied by extremely luminous radio emission. The X-ray burst from SGR 1935+2154 which had a contemporaneous radio counterpart was also distinct from previous X-ray bursts from the source with higher BB temperatures, steeper spectra, and larger peak energies. Thus, it appears that only certain, distinct X-ray bursts are capable of having accompanying radio emission. Why this is the case, and what is responsible for the different X-ray bursts, remains an open question.

Appendix A

Testing the *rfi-scout* Pipeline

Below, we further detail the *rfi-scout* pipeline. We discuss some of the more technical aspects of *rfi-scout* along with tests we perform for each of the different pipeline components. To evaluate each part of the pipeline, we use two different metrics: the total operational time of an action and the total data reduction achieved. We also use six different data sets for the tests: two where the metrics are collected at a 60 second cadence and four where the metrics are collected at a 10 second cadence. These data sets, and the different tests they are used for, are listed in Table A.1.

A.1 Querying from L1

A query of L1 for the RFI statistics returns an array response with various metrics e.g. the timestamp range of the query, the total number of masked samples, the total number of

L1 RFI Sampling Rate	Total Length	Date of Metrics	Tests
60 seconds	10 days	2020-05-10 to 2020-05-20	Polynomial outlier cutoff Fitting polynomials over multiple days
10 seconds	6 hours	2021-05-14	E-W averaging (per timestamp, per freq)
10 seconds	6 hours	2021-05-18	E-W averaging (per timestamp, per freq)
10 seconds	6 hours	2021-05-20	E-W averaging (per timestamp, per freq)
10 seconds	24 hours	2021-05-19 to 2021-05-20	E-W averaging (averaged over time and freq); Length of time of polynomial; Degree of polynomial; Number of fits for polynomial

Table A.1: Different data sets used to test *rfi-scout*. We list the cadence at which the L1 RFI metrics are sampled, the length of time over which they are sampled, the date on which they are sampled, and the tests that use them.

samples, the total number of unmasked samples, etc. However, for the purposes of monitoring rfi metrics, only the beam and the normalized mask per frequency channel are relevant. Thus, we extract these metrics¹ before storing the mask per frequency and per beam in a python dictionary². We do not downsample these data prior to their initial storage so that we may maintain a full resolution copy of the RFI metrics for a period of time. Additionally, rather than storing a unique timestamp for every beam, we ensure all beams are accessed at the same timestamp, reducing the cardinality of our data set by storing one timestamp for all beams. For beams which are offline, we set the masking fraction for all frequencies to None.

Querying the metrics from L1 takes ~ 1 second. Depending on the network speed, this

¹This is also referred to as “decoding.”

²For more details on python dictionaries, see the *Data Structure* chapter of docs.python.org.

query can take up to ~ 5 to 15 seconds. We query on exact multiples of 4 seconds, so if the previous query takes longer than 4 seconds, the following query will happen at the 8 second mark (or 16 second mark if the query takes 15 seconds). The decoding of the metrics can take up to ~ 2 seconds.

A.2 Initial Data Storage

Previously, the RFI metrics were stored in an SQL database. Writing and querying from SQL databases are straightforward, but not always the most efficient. When querying based on a time variable, SQL databases are slow as compared with time series databases³. As such, we explore using the time series database influxDB v2.0⁴ to initially store our RFI metrics⁵.

InfluxDB is structured to handle high volumes of reads and writes. Since we are attempting to write one million data points (1024 frequencies for 1024 beams) every four seconds, and then query these data from the database every six hours for further analysis, a high read and write ability is necessary. We can write all one million points to the influxDB in ~ 1 second which is within our time budget. However, we suffer major time losses when attempting to then query these data from the database for further analysis.

³Time series databases are designed specifically for the writing and querying of time-based data. For further details on this, we refer the reader to the [InfluxDB comparison with SQL databases](#).

⁴For details on influxDB, see [influxdata.com](#).

⁵There are two relevant databases for *rfi-scout*: 1. the initial database that the full resolution metrics are stored in and 2. the database that the final, downsampled data is stored in. The two are different.

The query time for 100 time stamps for 256 beams and 256 frequencies from the influxDB is 29 seconds. If we scale this to 1024 beams, 1024 frequencies, and a sampling rate of four seconds, then this query time is a fourth of the time spanned by the data.

To address this inefficiency, we test storing the data in two additional formats: npy files and npz files using python’s NumPy data package. We find that querying from npz files is 97.8% faster than querying from the influxDB. Even further, querying from npy files is 95% faster than querying from npz files. To achieve the smallest query time, we store our full resolution metrics in npy files. The final query time for all 1024 beams and 1024 frequencies over a 6 hour period from npy files is ~ 70 seconds.

We write the RFI metrics to the npy files every 5 minutes. At each write, the entire data array is written so the file is not corrupted if the *rfi-scout* pipeline breaks or the network goes down. However, writing the entire array can take significant time so we limit each file to only 30 minutes.

A.3 Downsampling in Frequency

After we query our data, we downsample it from 1024 frequency channels to 256 frequency channels, achieving a data reduction of 75%. Downsampling in frequency does, however, slightly decrease the total data reduction achieved in later processing steps. For example, for the same data set, we achieve an 81% data reduction during polynomial fitting if we do not downsample but only a 69% reduction if we downsample to 256 frequency channels. While

this is non-negligible, the 75% reduction achieved through this downsampling outweighs the 11% difference in the data reduction during polynomial fitting.

A.4 Downsampling Across E-W columns

As CHIME is oriented in the N-S direction, the E-W coverage is much smaller with less variation in the RFI across the four E-W columns as compared to the N-S columns, so we selectively downsample across the E-W CHIME columns. To selectively downsample a N-S row, we compare the RFI metrics for each E-W beam with the average across all four beams. We perform iterative fits where we remove beams for which more than a third of the timestamps are outliers. As our RFI metrics naturally fluctuate on the scale of 1 to 2%, we define an outlier in this part of the analysis chain as anything deviating from the average by more than 1%. We eliminate one beam at a time and recalculate the average until we either have no more outlier beams or until we have only one beam left in which case we store the metrics for all four beams independently.

As an initial test of downsampling across the E-W columns, we average the L1 RFI masking fraction over all frequencies and all time samples for an entire day and compare the average masking fraction across all E-W beams with the non-averaged E-W data. We repeat this process for different days. As seen in Fig. 3.6, the E-W average is a fairly strong fit to the data, with most residuals under 1% and only a few as large as 2%.

However, the data in Fig. 3.6 are averaged over all frequencies and time stamps. To test

Beams	Data Reduction
32 - 49	50%
96-112	65%
128-144	66%
160-176	66.5%
224-240	44%

Table A.2: Data reduction achieved for different N-S beam groupings after doing selective E-W downsampling. Each grouping takes the average over 16 different beams and three different six hour periods. The data are downsampled to 256 frequency channels prior to E-W downsampling. The E-W downsampling removes time stamps per beam and per frequency not within 1% of the average.

this on a per frequency basis and on a 10 second timescale, we analyze metrics from three different days: 14 May 2021, 18 May 2021, and 20 May 2021. All three days have nominal RFI masking. First, we split the beams into 16 different groups and test the data reduction achieved per group. As seen in table A.2, the fit is worse for edge N-S beams and better for central beams. This is not surprising as the RFI in the edge N-S beams is more scattered e.g. see Fig. 3.9.

Next, we take the average over all beam groups and all three days. We find a reduction in our total data⁶ of 57%. If instead we automatically assume the average accurately represents all beams in a row, then we would achieve a reduction of 75%. However, while better in terms of data reduction, this type of downsampling does not capture outliers from the average. We consider our selective downsampling to be a strong solution as we still achieve a reduction $> 50\%$ and we ensure that we can reconstruct the RFI masking per beam to within 1%.

⁶This is the reduction achieved on the already frequency-downsampled data.

Selectively downsampling 6 hours of RFI metrics on one 2.2 GHz core takes ~ 3000 seconds. However, we can greatly reduce this by performing this analysis on multiple cores. If we deploy *rfi-scout* over 16 different cores with each core operating on 16 N-S beams, then it only takes ~ 200 seconds to perform E-W downsampling. Analyzing 16 beams per core also reduces the frequency downsampling time to ~ 2 seconds.

A.5 Polynomial Fit

We also fit the RFI masking fraction per beam (selectively downsampled in the E-W direction) and per frequency bin (downsampled to 256 frequency bins) with a polynomial to further decrease our final data storage. We perform four tests of this polynomial fit: 1. the period over which the fit is applied, 2. the order of the polynomial, 3. the cutoff for residuals, and 4. the number of fitting rounds performed. Note we downsample in both frequency and over the E-W columns before performing these tests. Some tests are performed with data sampled at a 60 second scale (to reduce computational costs) while some are performed with data sampled at a 10 second scale. See Table A.1 for details on when each is used.

First, we investigate the time over which to apply the polynomial. We test three, six, and twelve hours of data. We do not test fitting a polynomial over 24 hours of data as it is too computationally expensive. The data reduction achieved for all three time spans are within a percent of each other. The only difference between the three is the time to perform the fit

and the number of fits generated over a 24 hour period (e.g. two for twelve hour periods and eight for three hour periods). As a compromise between the two, we fit our polynomial over a six hour timescale. The total time required to fit a polynomial over 6 hours of data for 16 beams (256 frequencies) ranges from 25 to 40 minutes depending on the beam grouping and the complexity of the RFI.

We also test the degree of our polynomial. We test polynomials of degree five, 10, 15, and 20. While the fit visually improves for higher order polynomials, there are a high number of numerical errors when fitting a 20 degree polynomial. We decide to perform all analysis using a 15 degree polynomial for which the numerical errors are reasonable. In the future, we may want to explore a custom polynomial fit that can avoid the high number of numerical errors.

We perform multiple rounds of fitting before settling on our final polynomial where in each round we eliminate extreme outliers from the fit. This requires both figuring out the best cutoff to use and the number of rounds of fitting to perform. Starting with our residual cutoff, we investigate four options:

1. a consistent 5σ limit for residuals where a new standard deviation is calculated after every round of fitting
2. a consistent 1σ limit for residuals where a new standard deviation is calculated after every round of fitting
3. a dynamic cutoff for each fit where the cutoff is determined by the round of fitting

along with the spread of the data

4. the same as in round three but with limitations on the minimum and final cutoff.

We find that options one and two result in significantly worse final fits than options three and four. Option three also results in less data reduction than option four. As the purpose of the polynomial fits is to achieve the greatest data reduction while still accurately reflecting the data, we implement option four. The final dynamic cutoff we implement is given by the round of fitting along with the spread in the data points through the equation:

$$\sigma = (n_fits - round + 1) * (max(rfi) - min(rfi))/n_fits. \quad (A.1)$$

where n_fits is the total number of fits we perform, $round$ is the current round of fitting we are on, rfi are the RFI metrics, and σ is the cutoff. We limit the cutoff to values above 2% with the cutoff automatically set to 2% for the final round. While the outliers are accumulated through the different fitting rounds, only the final polynomial is recorded.

We also test the number of fits to perform. Using the above definition for a cutoff, we test three, five, and ten rounds of fitting. As expected, as we increase the number of rounds, the time required to perform the polynomial fitting increases e.g. 10 rounds of fitting takes 60 minutes while five rounds of fitting takes 27 minutes for 16 beams over six hours of data. While 10 rounds of fitting performs better, the difference is not significant, with a 67% data reduction for 10 rounds of fitting and a 63% data reduction for five rounds of fitting. The

computational cost outweighs the data reduction benefit so we perform five rounds of fitting.

In addition to exploring various components of our polynomial fit, we also test how the RFI masking for a beam varies from day to day. This is fueled by the hypothesis that we might be able to fit every day (for a given beam and frequency bin) by the same polynomial and just record outliers from this polynomial. We compare polynomial fits for ten different 24 hour periods from 10 May 2020 through 20 May 2020. As seen in Fig. A.1, the masking fraction greatly varies over the course of multiple days. Thus, we cannot use the same polynomial to describe multiple days.

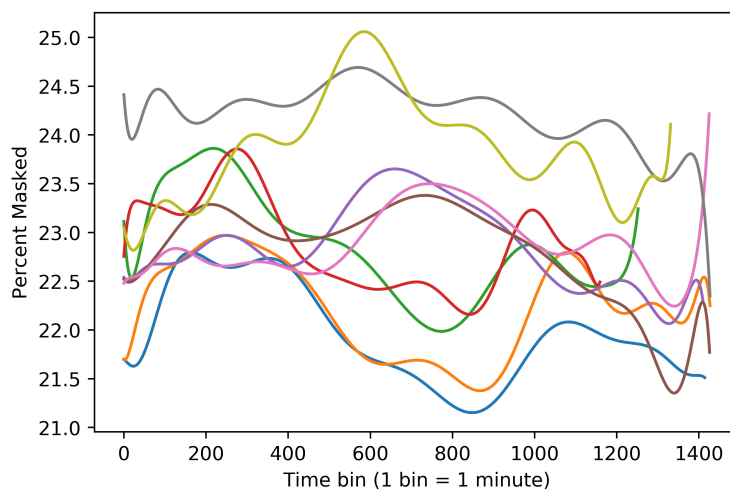


Figure A.1: Masking percent as a function of time for beam 100 from 10 May 2020 to 20 May 2020. To distinguish the different days, we only plot the polynomial fit for the masking percent instead of the individual data points. Each coloured curve represents a polynomial fit for a different day.

The result of each polynomial fit is a dictionary containing the beam, frequency bin, frequency resolution, polynomial fit, outlier values from the polynomial, corresponding

outlier times, and the time range (start and end times) over which the polynomial is valid. The dictionary also contains information on whether the beam represents an average over all E-W columns, or whether it was an outlier when performing the E-W averaging e.g. Fig. A.2.

```
rfi_dict = {}
rfi_dict["beam"] = beam
rfi_dict["freq"] = freq_chan
rfi_dict["num_freq_chan"] = self.num_freq_chan
rfi_dict["poly"] = p
rfi_dict["ew_outliar"] = is_ew_outliar
rfi_dict["outliar_values"] = polyfit_outliar_vals
rfi_dict["outliar_times"] = polyfit_outliar_times
rfi_dict["start_time"] = start_time
rfi_dict["stop_time"] = stop_time
```

Figure A.2: Example of the final dictionary that the downsampled RFI metrics produced by *rfi-scout* are stored in. There are nine different dictionary key, value pairs.

In addition to a dictionary per beam and per frequency for all beams and frequencies, we store one dictionary (total) containing the time range along with the specific timestamps over which the data are fit. We need not store this per beam and per frequency as all beams contain metrics for the same timestamps.

It takes ~ 25 to 40 minutes to perform the above polynomial fitting over 16 different cores after frequency downsampling and E-W downsampling. The time required to fit a polynomial is highly dependent on the specific beams being analyzed along with the variability of the RFI.

A.6 Final Data Storage

The data are finally stored in a mongoDB. MongoDB is a NoSQL database⁷, storing the data in dictionaries rather than in tables⁸. The L1 RFI metrics are stored in collections, similar to folders, on a per month basis to ease the access and re-creation of data e.g. the polynomial fits for the RFI metrics for August 2021 are stored separately from those for Sept 2021. The RFI at any point in time can then be easily reconstructed using the polynomial and outliers stored in the mongoDB.

A.7 Computational Cost of *rfi-scout*

The *rfi-scout* pipeline is slightly more computationally expensive than the previous RFI pipeline. Querying the RFI metrics from L1, writing them to npy files, and then loading them from these files takes ~ 75 seconds when performed on a single CPU core operating at 2.2 GHz. Downsampling in frequency, downsampling over the E-W columns, and fitting a polynomial takes significantly longer and requires multiple cores. Thus, we assume that we will deploy *rfi-scout* over 16 cores, where each core processes 16 different N-S rows. Using these cores, it takes ~ 30 to 45 minutes to downsample and polynomial fit 6 hours of RFI metrics. While more computationally expensive than the previous RFI pipeline⁹, this is still

⁷A NoSQL database is a non-relational database. Unlike an SQL database, a NoSQL database does not require there to be a relation between different data products within it.

⁸For further details on mongoDB and NoSQL databases, we refer the reader to [mongodb.com](https://www.mongodb.com)

⁹Previously, it took ~ 30 minutes to process 24 hours of data on a single CPU.

within the resource budget of CHIME/FRB. The increase in computational cost of *rfi-scout* is also greatly outweighed by the data reduction benefit it achieves (see Table 3.1 for details on this).

Bibliography

- [1] CHIME/FRB Collaboration, M. Amiri, K. Bandura, P. Berger, M. Bhardwaj, M. M. Boyce, P. J. Boyle, C. Brar, M. Burhanpurkar, P. Chawla, J. Chowdhury, J. F. Cliche, M. D. Cranmer, D. Cubranic, M. Deng, N. Denman, M. Dobbs, M. Fandino, E. Fonseca, B. M. Gaensler, U. Giri, A. J. Gilbert, D. C. Good, S. Guliani, M. Halpern, G. Hinshaw, C. Höfer, A. Josephy, V. M. Kaspi, T. L. Landecker, D. Lang, H. Liao, K. W. Masui, J. Mena-Parra, A. Naidu, L. B. Newburgh, C. Ng, C. Patel, U. L. Pen, T. Pinsonneault-Marotte, Z. Pleunis, M. Rafiei Ravandi, S. M. Ransom, A. Renard, P. Scholz, K. Sigurdson, S. R. Siegel, K. M. Smith, I. H. Stairs, S. P. Tendulkar, K. Vanderlinde, and D. V. Wiebe, “The CHIME Fast Radio Burst Project: System Overview,” , vol. 863, p. 48, Aug. 2018.
- [2] F. Collaboration, M. Amiri, B. C. Andersen, K. Bandura, S. Berger, M. Bhardwaj, M. M. Boyce, P. J. Boyle, C. Brar, D. Breitman, T. Cassanelli, P. Chawla, T. Chen, J. F. Cliche, A. Cook, D. Cubranic, A. P. Curtin, M. Deng, M. Dobbs, Fengqiu, Dong, G. Eadie, M. Fandino, E. Fonseca, B. M. Gaensler, U. Giri, D. C. Good, M. Halpern,

- A. S. Hill, G. Hinshaw, A. Josephy, J. F. Kaczmarek, Z. Kader, J. W. Kania, V. M. Kaspi, T. L. Landecker, D. Lang, C. Leung, D. Li, H.-H. Lin, K. W. Masui, R. Mckinven, J. Mena-Parra, M. Merryfield, B. W. Meyers, D. Michilli, N. Milutinovic, A. Mirhosseini, M. Münchmeyer, A. Naidu, L. Newburgh, C. Ng, C. Patel, U.-L. Pen, E. Petroff, T. Pinsonneault-Marotte, Z. Pleunis, M. Rafiei-Ravandi, M. Rahman, S. M. Ransom, A. Renard, P. Sanghavi, P. Scholz, J. R. Shaw, K. Shin, S. R. Siegel, A. E. Sikora, S. Singh, K. M. Smith, I. Stairs, C. M. Tan, S. P. Tendulkar, K. Vanderlinde, H. Wang, D. Wulf, and A. V. Zwaniga, “The first chime/frb fast radio burst catalog,” 2021.
- [3] A. Hewish, S. J. Bell, J. D. H. Pilkington, P. F. Scott, and R. A. Collins, “Observation of a Rapidly Pulsating Radio Source,” , vol. 217, pp. 709–713, Feb. 1968.
- [4] E. P. Mazets, S. V. Golentskii, V. N. Ilinskii, R. L. Aptekar, and I. A. Guryan, “Observations of a flaring X-ray pulsar in Dorado,” , vol. 282, pp. 587–589, Dec. 1979.
- [5] E. P. Mazets, S. V. Golenetskij, and Y. A. Guryan, “Soft gamma-ray bursts from the source B1900+14,” *Soviet Astronomy Letters*, vol. 5, p. 343, Dec. 1979.
- [6] S. V. Golenetskij, E. P. Mazets, V. N. Ilinskij, and Y. A. Guryan, “Recurrent gamma-ray bursts from the flaring source FXP 0520 - 66,” *Soviet Astronomy Letters*, vol. 5, pp. 340–342, Dec. 1979.

- [7] D. R. Lorimer, M. Bailes, M. A. McLaughlin, D. J. Narkevic, and F. Crawford, “A Bright Millisecond Radio Burst of Extragalactic Origin,” *Science*, vol. 318, p. 777, Nov. 2007.
- [8] CHIME/FRB Collaboration, B. C. Andersen, K. M. Bandura, M. Bhardwaj, A. Bij, M. M. Boyce, P. J. Boyle, C. Brar, T. Cassanelli, P. Chawla, T. Chen, J. F. Cliche, A. Cook, D. Cubranic, A. P. Curtin, N. T. Denman, M. Dobbs, F. Q. Dong, M. Fandino, E. Fonseca, B. M. Gaensler, U. Giri, D. C. Good, M. Halpern, A. S. Hill, G. F. Hinshaw, C. Höfer, A. Josephy, J. W. Kania, V. M. Kaspi, T. L. Landecker, C. Leung, D. Z. Li, H. H. Lin, K. W. Masui, R. McKinven, J. Mena-Parra, M. Merryfield, B. W. Meyers, D. Michilli, N. Milutinovic, A. Mirhosseini, M. Münchmeyer, A. Naidu, L. B. Newburgh, C. Ng, C. Patel, U. L. Pen, T. Pinsonneault-Marotte, Z. Pleunis, B. M. Quine, M. Rafei-Ravandi, M. Rahman, S. M. Ransom, A. Renard, P. Sanghavi, P. Scholz, J. R. Shaw, K. Shin, S. R. Siegel, S. Singh, R. J. Smegal, K. M. Smith, I. H. Stairs, C. M. Tan, S. P. Tendulkar, I. Tretyakov, K. Vanderlinde, H. Wang, D. Wulf, and A. V. Zwaniga, “A bright millisecond-duration radio burst from a Galactic magnetar,” , vol. 587, pp. 54–58, Nov. 2020.
- [9] R. F. Archibald, V. M. Kaspi, S. P. Tendulkar, and P. Scholz, “A magnetar-like outburst from a high-b radio pulsar,” *The Astrophysical Journal*, vol. 829, p. L21, Sep 2016.

-
- [10] V. M. Kaspi, M. S. E. Roberts, and A. K. Harding, *Isolated neutron stars*, vol. 39, pp. 279–339. 2006.
- [11] P. A. Caraveo, “Gamma-ray pulsar revolution,” *Annual Review of Astronomy and Astrophysics*, vol. 52, p. 211–250, Aug 2014.
- [12] R. N. Manchester, G. B. Hobbs, A. Teoh, and M. Hobbs, “The Australia Telescope National Facility Pulsar Catalogue,” , vol. 129, pp. 1993–2006, Apr. 2005.
- [13] V. M. Kaspi and M. Kramer, “Radio pulsars: The neutron star population fundamental physics,” in *Proc. 26th Solvay Conf. Phys. Astrophys. Cosmol., Brussels, Belgium*, pp. 22–61, 2015.
- [14] K. Bansal, G. B. Taylor, K. Stovall, and J. Dowell, “Scattering study of pulsars below 100 mhz using lwa1,” *The Astrophysical Journal*, vol. 875, p. 146, Apr 2019.
- [15] R. Narayan, “The Physics of Pulsar Scintillation,” *Philosophical Transactions of the Royal Society of London Series A*, vol. 341, pp. 151–165, Oct. 1992.
- [16] J. J. Condon and S. M. Ransom, *Essential Radio Astronomy*. 2016.
- [17] J. L. Han, R. N. Manchester, W. van Straten, and P. Demorest, “Pulsar rotation measures and large-scale magnetic field reversals in the galactic disk,” *The Astrophysical Journal Supplement Series*, vol. 234, p. 11, Jan 2018.

-
- [18] J. M. Weisberg, J. M. Cordes, B. Kuan, K. E. Devine, J. T. Green, and D. C. Backer, “Arecibo 430 MHz Pulsar Polarimetry: Faraday Rotation Measures and Morphological Classifications,” , vol. 150, pp. 317–341, Jan. 2004.
- [19] J. M. Yao, R. N. Manchester, and N. Wang, “A new electron-density model for estimation of pulsar and frb distances,” *The Astrophysical Journal*, vol. 835, p. 29, Jan 2017.
- [20] J. M. Weisberg, J. H. Taylor, and L. A. Fowler, “Gravitational waves from an orbiting pulsar,” *Scientific American*, vol. 245, pp. 74–82, Oct. 1981.
- [21] F. Jenet, L. S. Finn, J. Lazio, A. Lommen, M. McLaughlin, I. Stairs, D. Stinebring, J. Verbiest, A. Archibald, Z. Arzoumanian, D. Backer, J. Cordes, P. Demorest, R. Ferdman, P. Freire, M. Gonzalez, V. Kaspi, V. Kondratiev, D. Lorimer, R. Lynch, D. Nice, S. Ransom, R. Shannon, and X. Siemens, “The North American Nanohertz Observatory for Gravitational Waves,” *arXiv e-prints*, p. arXiv:0909.1058, Sept. 2009.
- [22] F. Camilo, S. M. Ransom, J. P. Halpern, and J. Reynolds, “1E 1547.0-5408: A Radio-emitting Magnetar with a Rotation Period of 2 Seconds,” , vol. 666, pp. L93–L96, Sept. 2007.
- [23] R. Dib and V. M. Kaspi, “16 yr of RXTE Monitoring of Five Anomalous X-Ray Pulsars,” , vol. 784, p. 37, Mar. 2014.

- [24] P. M. Woods and C. Thompson, *Soft gamma repeaters and anomalous X-ray pulsars: magnetar candidates*, p. 547. 2010.
- [25] V. M. Kaspi and A. M. Beloborodov, “Magnetars,” *Annual Review of Astronomy and Astrophysics*, vol. 55, p. 261–301, Aug 2017.
- [26] R. C. Duncan and C. Thompson, “Formation of Very Strongly Magnetized Neutron Stars: Implications for Gamma-Ray Bursts,” , vol. 392, p. L9, June 1992.
- [27] C. Thompson and R. C. Duncan, “The Soft Gamma Repeaters as Very Strongly Magnetized Neutron Stars. II. Quiescent Neutrino, X-Ray, and Alfvén Wave Emission,” , vol. 473, p. 322, Dec. 1996.
- [28] F. P. Gavriil, V. M. Kaspi, and P. M. Woods, “Magnetar-like X-ray bursts from an anomalous X-ray pulsar,” , vol. 419, pp. 142–144, Sept. 2002.
- [29] V. M. Kaspi, F. P. Gavriil, P. M. Woods, J. B. Jensen, M. S. E. Roberts, and D. Chakrabarty, “A Major Soft Gamma Repeater-like Outburst and Rotation Glitch in the No-longer-so-anomalous X-Ray Pulsar 1E 2259+586,” , vol. 588, pp. L93–L96, May 2003.
- [30] R. F. Archibald, V. M. Kaspi, P. Scholz, A. P. Beardmore, N. Gehrels, and J. A. Kennea, “Swift observations of two outbursts from the magnetar 4u 0142+61,” *The Astrophysical Journal*, vol. 834, p. 163, Jan 2017.

- [31] M. Lyutikov and F. P. Gavriil, “Resonant cyclotron scattering and Comptonization in neutron star magnetospheres,” , vol. 368, pp. 690–706, May 2006.
- [32] N. Rea, R. Turolla, S. Zane, A. Tramacere, L. Stella, G. L. Israel, and R. Campana, “Spectral Modeling of the High-Energy Emission of the Magnetar 4U 0142+614,” , vol. 661, pp. L65–L68, May 2007.
- [33] N. Rea, S. Zane, M. Lyutikov, and R. Turolla, “Our distorted view of magnetars: application of the resonant cyclotron scattering model,” , vol. 308, pp. 61–65, Apr. 2007.
- [34] R. Turolla, S. Zane, and A. L. Watts, “Magnetars: the physics behind observations. a review,” *Reports on Progress in Physics*, vol. 78, p. 116901, Oct 2015.
- [35] K. Hurley, S. E. Boggs, D. M. Smith, R. C. Duncan, R. Lin, A. Zoglauer, S. Krucker, G. Hurford, H. Hudson, C. Wigger, W. Hajdas, C. Thompson, I. Mitrofanov, A. Sanin, W. Boynton, C. Fellows, A. von Kienlin, G. Lichti, A. Rau, and T. Cline, “An exceptionally bright flare from SGR 1806-20 and the origins of short-duration γ -ray bursts,” , vol. 434, pp. 1098–1103, Apr. 2005.
- [36] K. Hurley, T. Cline, E. Mazets, S. Barthelmy, P. Butterworth, F. Marshall, D. Palmer, R. Aptekar, S. Golenetskii, V. Il’Inskii, D. Frederiks, J. McTiernan, R. Gold, and J. Trombka, “A giant periodic flare from the soft γ -ray repeater SGR1900+14,” , vol. 397, pp. 41–43, Jan. 1999.

- [37] D. M. Palmer, S. Barthelmy, N. Gehrels, R. M. Kippen, T. Cayton, C. Kouveliotou, D. Eichler, R. A. M. J. Wijers, P. M. Woods, J. Granot, Y. E. Lyubarsky, E. Ramirez-Ruiz, L. Barbier, M. Chester, J. Cummings, E. E. Fenimore, M. H. Finger, B. M. Gaensler, D. Hullinger, H. Krimm, C. B. Markwardt, J. A. Nousek, A. Parsons, S. Patel, T. Sakamoto, G. Sato, M. Suzuki, and J. Tueller, “A giant γ -ray flare from the magnetar SGR 1806 - 20,” , vol. 434, pp. 1107–1109, Apr. 2005.
- [38] A. M. Archibald, V. M. Kaspi, M. A. Livingstone, and M. A. McLaughlin, “No detectable radio emission from the magnetar-like pulsar in kes 75,” *The Astrophysical Journal*, vol. 688, p. 550–554, Nov 2008.
- [39] S. A. Olausen and V. M. Kaspi, “The mcgill magnetar catalog,” *The Astrophysical Journal Supplement Series*, vol. 212, p. 6, Apr 2014.
- [40] D. M. Palmer, P. A. Evans, N. P. M. Kuin, K. L. Page, and Swift Team, “Swift Detection of probable new Swift SGR J1555.2-5402,” *GRB Coordinates Network*, vol. 30120, p. 1, June 2021.
- [41] A. G. Mannings, W. fai Fong, S. Simha, J. X. Prochaska, M. Rafelski, C. D. Kilpatrick, N. Tejos, K. E. Heintz, S. Bhandari, C. K. Day, A. T. Deller, S. D. Ryder, R. M. Shannon, and S. P. Tendulkar, “A high-resolution view of fast radio burst host environments,” 2021.

- [42] S. P. Tendulkar, C. G. Bassa, J. M. Cordes, G. C. Bower, C. J. Law, S. Chatterjee, E. A. K. Adams, S. Bogdanov, S. Burke-Spolaor, B. J. Butler, P. Demorest, J. W. T. Hessels, V. M. Kaspi, T. J. W. Lazio, N. Maddox, B. Marcote, M. A. McLaughlin, Z. Paragi, S. M. Ransom, P. Scholz, A. Seymour, L. G. Spitler, H. J. van Langevelde, and R. S. Wharton, “The Host Galaxy and Redshift of the Repeating Fast Radio Burst FRB 121102,” , vol. 834, p. L7, Jan. 2017.
- [43] M. Bhardwaj, B. M. Gaensler, V. M. Kaspi, T. L. Landecker, R. Mckinven, D. Michilli, Z. Pleunis, S. P. Tendulkar, B. C. Andersen, P. J. Boyle, and et al., “A nearby repeating fast radio burst in the direction of m81,” *The Astrophysical Journal Letters*, vol. 910, p. L18, Mar 2021.
- [44] F. Kirsten, B. Marcote, K. Nimmo, J. W. T. Hessels, M. Bhardwaj, S. P. Tendulkar, A. Keimpema, J. Yang, M. P. Snelders, P. Scholz, A. B. Pearlman, C. J. Law, W. M. Peters, M. Giroletti, D. M. Hewitt, U. Bach, V. Bezukovs, M. Burgay, S. T. Buttaccio, J. E. Conway, A. Corongiu, R. Feiler, O. Forssén, M. P. Gawroński, R. Karuppusamy, M. A. Kharinov, M. Lindqvist, G. Maccaferri, A. Melnikov, O. S. Ould-Boukattine, Z. Paragi, A. Possenti, G. Surcis, N. Wang, J. Yuan, K. Aggarwal, R. Anna-Thomas, G. C. Bower, R. Blaauw, S. Burke-Spolaor, T. Cassanelli, T. E. Clarke, E. Fonseca, B. M. Gaensler, A. Gopinath, V. M. Kaspi, N. Kassim, T. J. W. Lazio, C. Leung, D. Li, H. H. Lin, K. W. Masui, R. Mckinven, D. Michilli, A. Mikhailov, C. Ng, A. Orbidans,

- U. L. Pen, E. Petroff, M. Rahman, S. M. Ransom, K. Shin, K. M. Smith, I. H. Stairs, and W. Vlemmings, “A repeating fast radio burst source in a globular cluster,” 2021.
- [45] Chime/Frb Collaboration, M. Amiri, B. C. Andersen, K. M. Bandura, M. Bhardwaj, P. J. Boyle, C. Brar, P. Chawla, T. Chen, J. F. Cliche, D. Cubranic, M. Deng, N. T. Denman, M. Dobbs, F. Q. Dong, M. Fandino, E. Fonseca, B. M. Gaensler, U. Giri, D. C. Good, M. Halpern, J. W. T. Hessels, A. S. Hill, C. Höfer, A. Josephy, J. W. Kania, R. Karuppusamy, V. M. Kaspi, A. Keimpema, F. Kirsten, T. L. Landecker, D. A. Lang, C. Leung, D. Z. Li, H. H. Lin, B. Marcote, K. W. Masui, R. McKinven, J. Mena-Parra, M. Merryfield, D. Michilli, N. Milutinovic, A. Mirhosseini, A. Naidu, L. B. Newburgh, C. Ng, K. Nimmo, Z. Paragi, C. Patel, U. L. Pen, T. Pinsonneault-Marotte, Z. Pleunis, M. Rafiei-Ravandi, M. Rahman, S. M. Ransom, A. Renard, P. Sanghavi, P. Scholz, J. R. Shaw, K. Shin, S. R. Siegel, S. Singh, R. J. Smegal, K. M. Smith, I. H. Stairs, S. P. Tendulkar, I. Tretyakov, K. Vanderlinde, H. Wang, X. Wang, D. Wulf, P. Yadav, and A. V. Zwaniga, “Periodic activity from a fast radio burst source,” , vol. 582, pp. 351–355, June 2020.
- [46] K. M. Rajwade, M. B. Mickaliger, B. W. Stappers, V. Morello, D. Agarwal, C. G. Bassa, R. P. Breton, M. Caleb, A. Karastergiou, E. F. Keane, and et al., “Possible periodic activity in the repeating frb 121102,” *Monthly Notices of the Royal Astronomical Society*, vol. 495, p. 3551–3558, May 2020.

- [47] M. Cruces, L. G. Spitler, P. Scholz, R. Lynch, A. Seymour, J. W. T. Hessels, C. Gouiffés, G. H. Hilmarsson, M. Kramer, and S. Munjal, “Repeating behaviour of FRB 121102: periodicity, waiting times, and energy distribution,” , vol. 500, pp. 448–463, Jan. 2021.
- [48] P. Kumar, W. Lu, and M. Bhattacharya, “Fast radio burst source properties and curvature radiation model,” , vol. 468, pp. 2726–2739, July 2017.
- [49] B. D. Metzger, B. Margalit, and L. Sironi, “Fast radio bursts as synchrotron maser emission from decelerating relativistic blast waves,” *Monthly Notices of the Royal Astronomical Society*, vol. 485, p. 4091–4106, Mar 2019.
- [50] B. Zhang, “A “cosmic comb” model of fast radio bursts,” *The Astrophysical Journal*, vol. 836, p. L32, Feb 2017.
- [51] Z. G. Dai, J. S. Wang, X. F. Wu, and Y. F. Huang, “Repeating fast radio bursts from highly magnetized pulsars traveling through asteroid belts,” *The Astrophysical Journal*, vol. 829, p. 27, Sep 2016.
- [52] K. Ioka, “Fast Radio Burst Breakouts from Magnetar Burst Fireballs,” , vol. 904, p. L15, Dec. 2020.
- [53] S. Hagstotz, R. Reichke, and R. Lilow, “A new measurement of the hubble constant using fast radio bursts,” 2021.

- [54] J. P. Macquart, J. X. Prochaska, M. McQuinn, K. W. Bannister, S. Bhandari, C. K. Day, A. T. Deller, R. D. Ekers, C. W. James, L. Marnoch, S. Osłowski, C. Phillips, S. D. Ryder, D. R. Scott, R. M. Shannon, and N. Tejos, “A census of baryons in the Universe from localized fast radio bursts,” , vol. 581, pp. 391–395, May 2020.
- [55] M. Pagano and H. Fronenberg, “Constraining the epoch of reionization with highly dispersed fast radio bursts,” *Monthly Notices of the Royal Astronomical Society*, vol. 505, p. 2195–2206, May 2021.
- [56] J. B. Muñoz, E. D. Kovetz, L. Dai, and M. Kamionkowski, “Lensing of fast radio bursts as a probe of compact dark matter,” *Physical Review Letters*, vol. 117, Aug 2016.
- [57] “A fast radio burst associated with a galactic magnetar,” *Nature*, vol. 587, no. 7832.
- [58] E. Petroff, E. D. Barr, A. Jameson, E. F. Keane, M. Bailes, M. Kramer, V. Morello, D. Tabbara, and W. van Straten, “FRBCAT: The Fast Radio Burst Catalogue,” , vol. 33, p. e045, Sept. 2016.
- [59] CHIME/FRB Collaboration, M. Amiri, K. Bandura, M. Bhardwaj, P. Boubel, M. M. Boyce, P. J. Boyle, C. . Brar, M. Burhanpurkar, T. Cassanelli, P. Chawla, J. F. Cliche, D. Cubranic, M. Deng, N. Denman, M. Dobbs, M. Fandino, E. Fonseca, B. M. Gaensler, A. J. Gilbert, A. Gill, U. Giri, D. C. Good, M. Halpern, D. S. Hanna, A. S. Hill, G. Hinshaw, C. Höfer, A. Josephy, V. M. Kaspi, T. L. Landecker, D. A. Lang, H. H. Lin, K. W. Masui, R. Mckinven, J. Mena-Parra, M. Merryfield, D. Michilli,

- N. Milutinovic, C. Moatti, A. Naidu, L. B. Newburgh, C. Ng, C. Patel, U. Pen, T. Pinsonneault-Marotte, Z. Pleunis, M. Rafei-Ravandi, M. Rahman, S. M. Ransom, A. Renard, P. Scholz, J. R. Shaw, S. R. Siegel, K. M. Smith, I. H. Stairs, S. P. Tendulkar, I. Tretyakov, K. Vanderlinde, and P. Yadav, “A second source of repeating fast radio bursts,” , vol. 566, pp. 235–238, Jan. 2019.
- [60] CHIME/FRB Collaboration, B. C. Andersen, K. Bandura, M. Bhardwaj, P. Boubel, M. M. Boyce, P. J. Boyle, C. Brar, T. Cassanelli, P. Chawla, D. Cubranic, M. Deng, M. Dobbs, M. Fandino, E. Fonseca, B. M. Gaensler, A. J. Gilbert, U. Giri, D. C. Good, M. Halpern, A. S. Hill, G. Hinshaw, C. Höfer, A. Josephy, V. M. Kaspi, R. Kothes, T. L. Landecker, D. A. Lang, D. Z. Li, H. H. Lin, K. W. Masui, J. Mena-Parra, M. Merryfield, R. Mckinven, D. Michilli, N. Milutinovic, A. Naidu, L. B. Newburgh, C. Ng, C. Patel, U. Pen, T. Pinsonneault-Marotte, Z. Pleunis, M. Rafei-Ravandi, M. Rahman, S. M. Ransom, A. Renard, P. Scholz, S. R. Siegel, S. Singh, K. M. Smith, I. H. Stairs, S. P. Tendulkar, I. Tretyakov, K. Vanderlinde, P. Yadav, and A. V. Zwaniga, “CHIME/FRB Discovery of Eight New Repeating Fast Radio Burst Sources,” , vol. 885, p. L24, Nov. 2019.
- [61] E. Fonseca, B. C. Andersen, M. Bhardwaj, P. Chawla, D. C. Good, A. Josephy, V. M. Kaspi, K. W. Masui, R. Mckinven, D. Michilli, Z. Pleunis, K. Shin, S. P. Tendulkar, K. M. Bandura, P. J. Boyle, C. Brar, T. Cassanelli, D. Cubranic, M. Dobbs, F. Q. Dong, B. M. Gaensler, G. Hinshaw, T. L. Landecker, C. Leung, D. Z. Li, H. H. Lin,

- J. Mena-Parra, M. Merryfield, A. Naidu, C. Ng, C. Patel, U. Pen, M. Rafei-Ravandi, M. Rahman, S. M. Ransom, P. Scholz, K. M. Smith, I. H. Stairs, K. Vanderlinde, P. Yadav, and A. V. Zwaniga, “Nine New Repeating Fast Radio Burst Sources from CHIME/FRB,” , vol. 891, p. L6, Mar. 2020.
- [62] A. Josephy, P. Chawla, A. P. Curtin, V. M. Kaspi, M. Bhardwaj, P. J. Boyle, C. Brar, T. Cassanelli, E. Fonseca, B. M. Gaensler, C. Leung, H. H. Lin, K. W. Masui, R. McKinven, J. Mena-Parra, D. Michilli, C. Ng, Z. Pleunis, M. Rafei-Ravandi, M. Rahman, P. Sanghavi, P. Scholz, K. M. Smith, I. H. Stairs, S. P. Tendulkar, and A. V. Zwaniga, “No evidence for galactic latitude dependence of the fast radio burst sky distribution,” 2021.
- [63] Z. Pleunis, D. C. Good, V. M. Kaspi, R. Mckinven, S. M. Ransom, P. Scholz, K. Bandura, M. Bhardwaj, P. J. Boyle, C. Brar, T. Cassanelli, P. Chawla, Fengqiu, Dong, E. Fonseca, B. M. Gaensler, A. Josephy, J. F. Kaczmarek, C. Leung, H.-H. Lin, K. W. Masui, J. Mena-Parra, D. Michilli, C. Ng, C. Patel, M. Rafei-Ravandi, M. Rahman, P. Sanghavi, K. Shin, K. M. Smith, I. H. Stairs, and S. P. Tendulkar, “Fast radio burst morphology in the first chime/frb catalog,” 2021.
- [64] M. Rafei-Ravandi, K. M. Smith, D. Li, K. W. Masui, A. Josephy, M. Dobbs, D. Lang, M. Bhardwaj, C. Patel, K. Bandura, S. Berger, P. J. Boyle, C. Brar, T. Cassanelli, P. Chawla, F. A. Dong, E. Fonseca, B. M. Gaensler, U. Giri, D. C. Good, M. Halpern,

- J. Kaczmarek, V. M. Kaspi, C. Leung, H.-H. Lin, J. Mena-Parra, B. W. Meyers, D. Michilli, M. Münchmeyer, C. Ng, E. Petroff, Z. Pleunis, M. Rahman, P. Sanghavi, P. Scholz, K. Shin, I. H. Stairs, S. P. Tendulkar, K. Vanderlinde, and A. Zwaniga, “Chime/frb catalog 1 results: statistical cross-correlations with large-scale structure,” 2021.
- [65] P. Chawla, V. M. Kaspi, S. M. Ransom, M. Bhardwaj, P. J. Boyle, D. Breitman, T. Cassanelli, D. Cubranic, F. Q. Dong, E. Fonseca, B. M. Gaensler, U. Giri, A. Josephy, J. F. Kaczmarek, C. Leung, K. W. Masui, J. Mena-Parra, M. Merryfield, D. Michilli, M. Münchmeyer, C. Ng, C. Patel, A. B. Pearlman, E. Petroff, Z. Pleunis, M. Rahman, P. Sanghavi, K. Shin, K. M. Smith, I. Stairs, and S. P. Tendulkar, “Modeling fast radio burst dispersion and scattering properties in the first chime/frb catalog,” 2021.
- [66] L. Connor, M. C. Miller, and D. W. Gardenier, “Beaming as an explanation of the repetition/width relation in frbs,” *Monthly Notices of the Royal Astronomical Society*, vol. 497, p. 3076–3082, Jul 2020.
- [67] J. M. Cordes, I. Wasserman, J. W. T. Hessels, T. J. W. Lazio, S. Chatterjee, and R. S. Wharton, “Lensing of Fast Radio Bursts by Plasma Structures in Host Galaxies,” , vol. 842, p. 35, June 2017.

- [68] M. Caleb, B. W. Stappers, T. D. Abbott, E. D. Barr, M. C. Bezuidenhout, S. J. Buchner, M. Burgay, W. Chen, I. Cognard, L. N. Driessen, R. Fender, G. H. Hilmarsson, J. Hoang, D. M. Horn, F. Jankowski, M. Kramer, D. R. Lorimer, M. Malenta, V. Morello, M. Pilia, E. Platts, A. Possenti, K. M. Rajwade, A. Ridolfi, L. Rhodes, S. Sanidas, M. Serylak, L. G. Spitler, L. J. Townsend, A. Weltman, P. A. Woudt, and J. Wu, “Simultaneous multi-telescope observations of FRB 121102,” , vol. 496, pp. 4565–4573, Aug. 2020.
- [69] E. Parent, P. Chawla, V. M. Kaspi, G. Y. Agazie, H. Blumer, M. DeCesar, W. Fiore, E. Fonseca, J. W. T. Hessels, D. L. Kaplan, and et al., “First discovery of a fast radio burst at 350 mhz by the gbnc survey,” *The Astrophysical Journal*, vol. 904, p. 92, Nov 2020.
- [70] S. Bhandari, E. F. Keane, E. D. Barr, A. Jameson, E. Petroff, S. Johnston, M. Bailes, N. D. R. Bhat, M. Burgay, S. Burke-Spolaor, M. Caleb, R. P. Eatough, C. Flynn, J. A. Green, F. Jankowski, M. Kramer, V. V. Krishnan, V. Morello, A. Possenti, B. Stappers, C. Tiburzi, W. van Straten, I. Andreoni, T. Butterley, P. Chandra, J. Cooke, A. Corongiu, D. M. Coward, V. S. Dhillon, R. Dodson, L. K. Hardy, E. J. Howell, P. Jaroenjittichai, A. Klotz, S. P. Littlefair, T. R. Marsh, M. Mickaliger, T. Muxlow, D. Perrodin, T. Pritchard, U. Sawangwit, T. Terai, N. Tominaga, P. Torne, T. Totani, A. Trois, D. Turpin, Y. Niino, R. W. Wilson, A. Albert, M. André, M. Anghinolfi, G. Anton, M. Ardid, J. J. Aubert, T. Avgitas, B. Baret, J. Barrios-Martí, S. Basa,

B. Belhorma, V. Bertin, S. Biagi, R. Bormuth, S. Bourret, M. C. Bouwhuis, H. Brânzăș, R. Bruijn, J. Brunner, J. Busto, A. Capone, L. Caramete, J. Carr, S. Celli, R. C. E. Moursli, T. Chiarusi, M. Circella, J. A. B. Coelho, A. Coleiro, R. Coniglione, H. Costantini, P. Coyle, A. Creusot, A. F. Díaz, A. Deschamps, G. De Bonis, C. Distefano, I. D. Palma, A. Domi, C. Donzaud, D. Dornic, D. Drouhin, T. Eberl, I. E. Bojaddaini, N. E. Khayati, D. Elsässer, A. Enzenhöfer, A. Ettahiri, F. Fassi, I. Felis, L. A. Fusco, P. Gay, V. Giordano, H. Glotin, T. Gregoire, R. Gracia-Ruiz, K. Graf, S. Hallmann, H. van Haren, A. J. Heijboer, Y. Hello, J. J. Hernández-Rey, J. Höbl, J. Hofestädt, C. Hugon, G. Illuminati, C. W. James, M. de Jong, M. Jongen, M. Kadler, O. Kalekin, U. Katz, D. Kießling, A. Kouchner, M. Kreter, I. Kreykenbohm, V. Kulikovskiy, C. Lachaud, R. Lahmann, D. Lefèvre, E. Leonora, S. Loucatos, M. Marcelin, A. Margiotta, A. Marinelli, J. A. Martínez-Mora, R. Mele, K. Melis, T. Michael, P. Migliozzi, A. Moussa, S. Navas, E. Nezri, M. Organokov, G. E. Păvălaș, C. Pellegrino, C. Perrina, P. Piattelli, V. Popa, T. Pradier, L. Quinn, C. Racca, G. Riccobene, A. Sánchez-Losa, M. Saldaña, I. Salvadori, D. F. E. Samtleben, M. Sanguineti, P. Sapienza, F. Schüssler, C. Sieger, M. Spurio, T. Stolarczyk, M. Taiuti, Y. Tayalati, A. Trovato, D. Turpin, C. Tönnis, B. Vallage, V. Van Elewyck, F. Versari, D. Vivolo, A. Vizzocca, J. Wilms, J. D. Zornoza, and J. Zúñiga, “The SURvey for Pulsars and Extragalactic Radio Bursts - II. New FRB discoveries and their follow-up,” , vol. 475, pp. 1427–1446, Apr. 2018.

- [71] R. M. Shannon, J. P. Macquart, K. W. Bannister, R. D. Ekers, C. W. James, S. Osłowski, H. Qiu, M. Sammons, A. W. Hotan, M. A. Voronkov, R. J. Beresford, M. Brothers, A. J. Brown, J. D. Bunton, A. P. Chippendale, C. Haskins, M. Leach, M. Marquarding, D. McConnell, M. A. Pilawa, E. M. Sadler, E. R. Troup, J. Tuthill, M. T. Whiting, J. R. Allison, C. S. Anderson, M. E. Bell, J. D. Collier, G. Gürkan, G. Heald, and C. J. Riseley, “The dispersion-brightness relation for fast radio bursts from a wide-field survey,” , vol. 562, pp. 386–390, Oct. 2018.
- [72] W. Farah, C. Flynn, M. Bailes, A. Jameson, T. Bateman, D. Campbell-Wilson, C. K. Day, A. T. Deller, A. J. Green, V. Gupta, and et al., “Five new real-time detections of fast radio bursts with utmost,” *Monthly Notices of the Royal Astronomical Society*, vol. 488, p. 2989–3002, Jul 2019.
- [73] E. Petroff, W. van Straten, S. Johnston, M. Bailes, E. D. Barr, S. D. Bates, N. D. R. Bhat, M. Burgay, S. Burke-Spolaor, D. Champion, and et al., “An absence of fast radio bursts at intermediate galactic latitudes,” *The Astrophysical Journal*, vol. 789, p. L26, Jun 2014.
- [74] D. J. Champion, E. Petroff, M. Kramer, M. J. Keith, M. Bailes, E. D. Barr, S. D. Bates, N. D. R. Bhat, M. Burgay, S. Burke-Spolaor, C. M. L. Flynn, A. Jameson, S. Johnston, C. Ng, L. Levin, A. Possenti, B. W. Stappers, W. van Straten, D. Thornton, C. Tiburzi,

- and A. G. Lyne, “Five new fast radio bursts from the HTRU high-latitude survey at Parkes: first evidence for two-component bursts,” , vol. 460, pp. L30–L34, July 2016.
- [75] C. D. Bochenek, V. Ravi, and D. Dong, “Localized Fast Radio Bursts Are Consistent with Magnetar Progenitors Formed in Core-collapse Supernovae,” , vol. 907, p. L31, Feb. 2021.
- [76] L. Marnoch, S. D. Ryder, K. W. Bannister, S. Bhandari, C. K. Day, A. T. Deller, J.-P. Macquart, R. M. McDermid, J. Xavier Prochaska, H. Qiu, and et al., “A search for supernova-like optical counterparts to askap-localised fast radio bursts,” *Astronomy Astrophysics*, vol. 639, p. A119, Jul 2020.
- [77] L. G. Spitler, J. M. Cordes, J. W. T. Hessels, D. R. Lorimer, M. A. McLaughlin, S. Chatterjee, F. Crawford, J. S. Deneva, V. M. Kaspi, R. S. Wharton, B. Allen, S. Bogdanov, A. Brazier, F. Camilo, P. C. C. Freire, F. A. Jenet, C. Karako-Argaman, B. Knispel, P. Lazarus, K. J. Lee, J. van Leeuwen, R. Lynch, S. M. Ransom, P. Scholz, X. Siemens, I. H. Stairs, K. Stovall, J. K. Swiggum, A. Venkataraman, W. W. Zhu, C. Aulbert, and H. Fehrmann, “Fast Radio Burst Discovered in the Arecibo Pulsar ALFA Survey,” , vol. 790, p. 101, Aug. 2014.
- [78] L. G. Spitler, P. Scholz, J. W. T. Hessels, S. Bogdanov, A. Brazier, F. Camilo, S. Chatterjee, J. M. Cordes, F. Crawford, J. Deneva, R. D. Ferdman, P. C. C. Freire, V. M. Kaspi, P. Lazarus, R. Lynch, E. C. Madsen, M. A. McLaughlin, C. Patel, S. M.

- Ransom, A. Seymour, I. H. Stairs, B. W. Stappers, J. van Leeuwen, and W. W. Zhu, “A repeating fast radio burst,” , vol. 531, pp. 202–205, Mar. 2016.
- [79] Y. Li, B. Zhang, K. Nagamine, and J. Shi, “The FRB 121102 Host Is Atypical among Nearby Fast Radio Bursts,” , vol. 884, p. L26, Oct. 2019.
- [80] S. Chatterjee, C. J. Law, R. S. Wharton, S. Burke-Spolaor, J. W. T. Hessels, G. C. Bower, J. M. Cordes, S. P. Tendulkar, C. G. Bassa, P. Demorest, B. J. Butler, A. Seymour, P. Scholz, M. W. Abruzzo, S. Bogdanov, V. M. Kaspi, A. Keimpema, T. J. W. Lazio, B. Marcote, M. A. McLaughlin, Z. Paragi, S. M. Ransom, M. Rupen, L. G. Spitler, and H. J. van Langevelde, “A direct localization of a fast radio burst and its host,” , vol. 541, pp. 58–61, Jan. 2017.
- [81] B. Marcote, Z. Paragi, J. W. T. Hessels, A. Keimpema, H. J. van Langevelde, Y. Huang, C. G. Bassa, S. Bogdanov, G. C. Bower, S. Burke-Spolaor, B. J. Butler, R. M. Campbell, S. Chatterjee, J. M. Cordes, P. Demorest, M. A. Garrett, T. Ghosh, V. M. Kaspi, C. J. Law, T. J. W. Lazio, M. A. McLaughlin, S. M. Ransom, C. J. Salter, P. Scholz, A. Seymour, A. Siemion, L. G. Spitler, S. P. Tendulkar, and R. S. Wharton, “The Repeating Fast Radio Burst FRB 121102 as Seen on Milliarsecond Angular Scales,” , vol. 834, p. L8, Jan. 2017.
- [82] D. Michilli, A. Seymour, J. W. T. Hessels, L. G. Spitler, V. Gajjar, A. M. Archibald, G. C. Bower, S. Chatterjee, J. M. Cordes, K. Gourdji, G. H. Heald, V. M. Kaspi,

- C. J. Law, C. Sobey, E. A. K. Adams, C. G. Bassa, S. Bogdanov, C. Brinkman, P. Demorest, F. Fernandez, G. Hellbourg, T. J. W. Lazio, R. S. Lynch, N. Maddox, B. Marcote, M. A. McLaughlin, Z. Paragi, S. M. Ransom, P. Scholz, A. P. V. Siemion, S. P. Tendulkar, P. van Rooy, R. S. Wharton, and D. Whitlow, “An extreme magnetospheric environment associated with the fast radio burst source FRB 121102,” , vol. 553, pp. 182–185, Jan. 2018.
- [83] A. Josephy, P. Chawla, E. Fonseca, C. Ng, C. Patel, Z. Pleunis, P. Scholz, B. C. Andersen, K. Bandura, M. Bhardwaj, M. M. Boyce, P. J. Boyle, C. Brar, D. Cubranic, M. Dobbs, B. M. Gaensler, A. Gill, U. Giri, D. C. Good, M. Halpern, G. Hinshaw, V. M. Kaspi, T. L. Landecker, D. A. Lang, H. H. Lin, K. W. Masui, R. Mckinven, J. Menaparra, M. Merryfield, D. Michilli, N. Milutinovic, A. Naidu, U. Pen, M. Rafiei-Ravandi, M. Rahman, S. M. Ransom, A. Renard, S. R. Siegel, K. M. Smith, I. H. Stairs, S. P. Tendulkar, K. Vanderlinde, P. Yadav, and A. V. Zwaniga, “CHIME/FRB Detection of the Original Repeating Fast Radio Burst Source FRB 121102,” , vol. 882, p. L18, Sept. 2019.
- [84] Z. Pleunis, D. Michilli, C. G. Bassa, J. W. T. Hessels, A. Naidu, B. C. Andersen, P. Chawla, E. Fonseca, A. Gopinath, V. M. Kaspi, and et al., “Lofar detection of 110–188 mhz emission and frequency-dependent activity from frb 20180916b,” *The Astrophysical Journal Letters*, vol. 911, p. L3, Apr 2021.

- [85] E. Petroff, J. W. T. Hessels, and D. R. Lorimer, “Fast radio bursts at the dawn of the 2020s,” 2021.
- [86] J. M. Cordes and I. Wasserman, “Supergiant pulses from extragalactic neutron stars,” , vol. 457, pp. 232–257, Mar. 2016.
- [87] L. Connor, J. Sievers, and U.-L. Pen, “Non-cosmological FRBs from young supernova remnant pulsars,” , vol. 458, pp. L19–L23, May 2016.
- [88] M. Lyutikov, L. Burzawa, and S. B. Popov, “Fast radio bursts as giant pulses from young rapidly rotating pulsars,” , vol. 462, pp. 941–950, Oct. 2016.
- [89] W. Lu and P. Kumar, “On the radiation mechanism of repeating fast radio bursts,” , vol. 477, pp. 2470–2493, June 2018.
- [90] Y. Lyubarsky, “A model for fast extragalactic radio bursts,” *Monthly Notices of the Royal Astronomical Society: Letters*, vol. 442, p. L9–L13, Apr 2014.
- [91] A. M. Beloborodov, “A Flaring Magnetar in FRB 121102?,” , vol. 843, p. L26, July 2017.
- [92] D. C. Good, B. C. Andersen, P. Chawla, K. Crowter, F. Q. Dong, E. Fonseca, B. W. Meyers, C. Ng, Z. Pleunis, S. M. Ransom, I. H. Stairs, C. M. Tan, M. Bhardwaj, P. J. Boyle, M. Dobbs, B. M. Gaensler, V. M. Kaspi, K. W. Masui, A. Naidu, M. Rafiei-

- Ravandi, P. Scholz, K. M. Smith, and S. P. Tendulkar, “First discovery of new pulsars and rrats with chime/frb,” 2020.
- [93] C. Ng, K. Vanderlinde, A. Paradise, P. Klages, K. Masui, K. Smith, K. Bandura, P. J. Boyle, M. Dobbs, V. Kaspi, and et al., “Chime frb: An application of fft beamforming for a radio telescope,” *2017 XXXIInd General Assembly and Scientific Symposium of the International Union of Radio Science (URSI GASS)*, Aug 2017.
- [94] L. B. Newburgh, G. E. Addison, M. Amiri, K. Bandura, J. R. Bond, L. Connor, J.-F. Cliche, G. Davis, M. Deng, N. Denman, M. Dobbs, M. Fandino, H. Fong, K. Gibbs, A. Gilbert, E. Griffin, M. Halpern, D. Hanna, A. D. Hincks, G. Hinshaw, C. Höfer, P. Klages, T. Landecker, K. Masui, J. M. Parra, U.-L. Pen, J. Peterson, A. Recnik, J. R. Shaw, K. Sigurdson, M. Sitwell, G. Smecher, R. Smegal, K. Vanderlinde, and D. Wiebe, “Calibrating CHIME: a new radio interferometer to probe dark energy,” in *Ground-based and Airborne Telescopes V* (L. M. Stepp, R. Gilmozzi, and H. J. Hall, eds.), vol. 9145 of *Society of Photo-Optical Instrumentation Engineers (SPIE) Conference Series*, p. 91454V, July 2014.
- [95] K. W. Masui, J. R. Shaw, C. Ng, K. M. Smith, K. Vanderlinde, and A. Paradise, “Algorithms for FFT Beamforming Radio Interferometers,” , vol. 879, p. 16, July 2019.

- [96] M. Amiri, K. M. Bandura, P. J. Boyle, C. Brar, J.-F. Cliche, K. Crowter, D. Cubranic, P. B. Demorest, N. T. Denman, M. Dobbs, and et al., “The chime pulsar project: System overview,” *The Astrophysical Journal Supplement Series*, vol. 255, p. 5, Jun 2021.
- [97] L. B. Newburgh, G. E. Addison, M. Amiri, K. Bandura, J. R. Bond, L. Connor, J.-F. Cliche, G. Davis, M. Deng, N. Denman, and et al., “Calibrating chime: a new radio interferometer to probe dark energy,” *Ground-based and Airborne Telescopes V*, Jul 2014.
- [98] B. Zackay and E. O. Ofek, “An accurate and efficient algorithm for detection of radio bursts with an unknown dispersion measure, for single-dish telescopes and interferometers,” *The Astrophysical Journal*, vol. 835, p. 11, Jan 2017.
- [99] A. Josephy, *Radio transient classification algorithms for CHIME/FRB*. PhD thesis, McGill University, 2018.
- [100] B. T. Indermuehle, L. Harvey-Smith, C. Wilson, and K. Chow, “The askap rfi environment as seen through beta,” in *2016 Radio Frequency Interference (RFI)*, pp. 43–48, 2016.
- [101] M. Sokolowski, R. B. Wayth, and T. Ellement, “The statistics of radio frequency interference propagating from long distances to the murchison radio-astronomy observatory,” in *2016 Radio Frequency Interference (RFI)*, pp. 105–110, 2016.

- [102] S. J. Tingay, M. Sokolowski, R. Wayth, and D. Ung, “A survey of spatially and temporally resolved radio frequency interference in the fm band at the murchison radio-astronomy observatory,” *Publications of the Astronomical Society of Australia*, vol. 37, 2020.
- [103] L. E. Frenzel, “Chapter 8 - cell phones: It is now possible to do anything wirelessly: Talk, text, email, web browse, games, whatever,” in *Electronics Explained (Second Edition)* (L. E. Frenzel, ed.), pp. 195–216, Newnes, second edition ed., 2018.
- [104] B. J. NELSON, *REMOTE PROCEDURE CALL*. PhD thesis, 1981. Copyright - Database copyright ProQuest LLC; ProQuest does not claim copyright in the individual underlying works; Last updated - 2021-05-24.
- [105] M. Stamatikos, D. Malesani, K. L. Page, and T. Sakamoto, “GRB 140705A: Swift detection of a short burst.,” *GRB Coordinates Network*, vol. 16520, p. 1, Jan. 2014.
- [106] G. L. Israel, P. Esposito, N. Rea, F. Coti Zelati, A. Tiengo, S. Campana, S. Mereghetti, G. A. Rodriguez Castillo, D. Götz, M. Burgay, A. Possenti, S. Zane, R. Turolla, R. Perna, G. Cannizzaro, and J. Pons, “The discovery, monitoring and environment of SGR J1935+2154,” , vol. 457, pp. 3448–3456, Apr. 2016.
- [107] G. Younes, C. Kouveliotou, A. Jaodand, M. G. Baring, A. J. van der Horst, A. K. Harding, J. W. T. Hessels, N. Gehrels, R. Gill, D. Huppenkothen, and et al., “X-ray

- and radio observations of the magnetar sgr j1935+2154 during its 2014, 2015, and 2016 outbursts,” *The Astrophysical Journal*, vol. 847, p. 85, Sep 2017.
- [108] B. M. Gaensler, “GRB 140705A / SGR 1935+2154: Probable association with supernova remnant G57.2+0.8,” *GRB Coordinates Network*, vol. 16533, p. 1, Jan. 2014.
- [109] R. Kothes, X. Sun, B. Gaensler, and W. Reich, “A Radio Continuum and Polarization Study of SNR G57.2+0.8 Associated with Magnetar SGR 1935+2154,” , vol. 852, p. 54, Jan. 2018.
- [110] P. Zhou, X. Zhou, Y. Chen, J.-S. Wang, J. Vink, and Y. Wang, “Revisiting the distance, environment, and supernova properties of snr g57.2+0.8 that hosts sgr 1935+2154,” *The Astrophysical Journal*, vol. 905, p. 99, Dec 2020.
- [111] S.-Q. Zhong, Z.-G. Dai, H.-M. Zhang, and C.-M. Deng, “On the distance of sgr 1935+2154 associated with frb 200428 and hosted in snr g57.2+0.8,” *The Astrophysical Journal*, vol. 898, p. L5, Jul 2020.
- [112] M. Bailes, C. G. Bassa, G. Bernardi, S. Buchner, M. Burgay, M. Caleb, A. J. Cooper, G. Desvignes, P. J. Groot, I. Heywood, and et al., “Multifrequency observations of sgrj1935+2154,” *Monthly Notices of the Royal Astronomical Society*, vol. 503, p. 5367–5384, Mar 2021.

- [113] J. Wood, E. Bissaldi, and Fermi GBM Team, “Fermi/GBM observation of a bright burst from magnetar SGR 1935+2154,” *GRB Coordinates Network*, vol. 25975, p. 1, Oct. 2019.
- [114] P. Scholz and Chime/Frb Collaboration, “A bright millisecond-timescale radio burst from the direction of the Galactic magnetar SGR 1935+2154,” *The Astronomer’s Telegram*, vol. 13681, p. 1, Apr. 2020.
- [115] C. K. Li, L. Lin, S. L. Xiong, M. Y. Ge, X. B. Li, T. P. Li, F. J. Lu, S. N. Zhang, Y. L. Tuo, Y. Nang, and et al., “Hxmt identification of a non-thermal x-ray burst from sgr j1935+2154 and with frb 200428,” *Nature Astronomy*, vol. 5, p. 378–384, Feb 2021.
- [116] A. Ridnaia, D. Svinkin, D. Frederiks, A. Bykov, S. Popov, R. Aptekar, S. Golenetskii, A. Lysenko, A. Tsvetkova, M. Ulanov, and et al., “A peculiar hard x-ray counterpart of a galactic fast radio burst,” *Nature Astronomy*, vol. 5, p. 372–377, Feb 2021.
- [117] M. Tavani, A. Ursi, F. Verrecchia, C. Casentini, C. Pittori, M. Pilia, M. Cardillo, G. Piano, A. Bulgarelli, V. Fioretti, N. Parmiggiani, F. Lucarelli, I. Donnarumma, S. Vercellone, F. Gianotti, M. Trifoglio, A. Giuliani, S. Mereghetti, P. Caraveo, F. Perotti, A. Chen, A. Argan, E. Costa, E. Del Monte, Y. Evangelista, M. Feroci, F. Lazzarotto, I. Lapshov, L. Pacciani, P. Soffitta, V. Vittorini, G. Di Cocco, F. Fuschino, M. Galli, C. Labanti, M. Marisaldi, A. Pellizzoni, A. Trois, G. Barbiellini, E. Vallazza, F. Longo, A. Morselli, P. Picozza, M. Prest, P. Lipari, D. Zanello, P. W.

- Cattaneo, A. Rappoldi, A. Ferrari, F. Paoletti, A. Antonelli, P. Giommi, L. Salotti, G. Valentini, and F. D'Amico, "AGILE detection of a hard X-ray burst in temporal coincidence with a radio burst from SGR 1935+2154," *The Astronomer's Telegram*, vol. 13686, p. 1, Apr. 2020.
- [118] S. Mereghetti, V. Savchenko, C. Ferrigno, D. Götz, M. Rigoselli, A. Tiengo, A. Bazzano, E. Bozzo, A. Coleiro, T. J.-L. Courvoisier, and et al., "Integral discovery of a burst with associated radio emission from the magnetar sgr 1935+2154," *The Astrophysical Journal*, vol. 898, p. L29, Jul 2020.
- [119] A. von Kienlin and Fermi Gamma-ray Burst Monitor Team, "Fermi GBM GRBs 191104 A, B, C and triggers 594534420/191104185 and 594563923/191104527 are not GRBs," *GRB Coordinates Network*, vol. 26163, p. 1, Nov. 2019.
- [120] E. Ambrosi, V. D'Elia, J. A. Kennea, D. M. Palmer, and Neil Gehrels Swift Observatory Team, "Trigger 933276: Swift detection of further activity from SGR 1935+2154," *GRB Coordinates Network*, vol. 26169, p. 1, Nov. 2019.
- [121] E. Ambrosi, V. D'Elia, J. A. Kennea, D. M. Palmer, and Neil Gehrels Swift Observatory Team, "Trigger 933285: Swift detection of the brightest burst so far from SGR 1935+2154," *GRB Coordinates Network*, vol. 26171, p. 1, Nov. 2019.
- [122] A. R. Thompson, J. M. Moran, and J. Swenson, George W., *Interferometry and Synthesis in Radio Astronomy, 2nd Edition*. 2001.

- [123] J. W. M. Baars and G. Swenson, “The Paraboloidal Reflector Antenna in Radio Astronomy and Communication: Theory and Practice,” *Physics Today*, vol. 61, p. 53, Jan. 2008.
- [124] P. Berger, L. B. Newburgh, M. Amiri, K. Bandura, J.-F. Cliche, L. Connor, M. Deng, N. Denman, M. Dobbs, M. Fandino, and et al., “Holographic beam mapping of the chime pathfinder array,” *Ground-based and Airborne Telescopes VI*, Aug 2016.
- [125] S. Barthelmy, L. Barbier, J. Cummings, E. Fenimore, N. Gehrels, D. Hullinger, H. Krimm, C. Markwardt, D. Palmer, A. Parsons, G. Sato, M. Suzuki, T. Takahashi, M. Tashiro, and J. Tueller, “The burst alert telescope (bat) on the swift midex mission,” *Space Science Reviews*, vol. 120, pp. 143–164, Dec. 2005.
- [126] K. A. Arnaud, “Xspec,” in *Astronomical Data Analysis Software and Systems V* (G. Jacoby and J. Barnes, eds.), vol. 101, (San Fransisco), p. 17, ASP, 1996.
- [127] L. Lin, E. Göğüş, O. J. Roberts, C. Kouveliotou, Y. Kaneko, A. J. van der Horst, and G. Younes, “Burst properties of the most recurring transient magnetar sgr j1935+2154,” *The Astrophysical Journal*, vol. 893, p. 156, Apr 2020.
- [128] A. J. van der Horst, C. Kouveliotou, N. M. Gorgone, Y. Kaneko, M. G. Baring, S. Guiriec, E. Göğüş, J. Granot, A. L. Watts, L. Lin, and et al., “Sgr j1550–5418 bursts detected with the fermi gamma-ray burst monitor during its most prolific activity,” *The Astrophysical Journal*, vol. 749, p. 122, Mar 2012.

- [129] L. Lin, C. Kouveliotou, M. G. Baring, A. J. van der Horst, S. Guiriec, P. M. Woods, E. Göğüş, Y. Kaneko, J. Scargle, J. Granot, R. Preece, A. von Kienlin, V. Chaplin, A. L. Watts, R. A. M. J. Wijers, S. N. Zhang, N. Bhat, M. H. Finger, N. Gehrels, A. Harding, L. Kaper, V. Kaspi, J. Mcenery, C. A. Meegan, W. S. Paciasas, A. Pe'er, E. Ramirez-Ruiz, M. van der Klis, S. Wachter, and C. Wilson-Hodge, “Fermi/GAMMA-RAY BURST MONITOR OBSERVATIONS OF SGR j05014516 BURSTS,” *The Astrophysical Journal*, vol. 739, p. 87, sep 2011.
- [130] W. B. Atwood, A. A. Abdo, M. Ackermann, W. Althouse, B. Anderson, M. Axelsson, L. Baldini, J. Ballet, D. L. Band, G. Barbiellini, and et al., “The large area telescope on thefermi gamma-ray space telescopemission,” *The Astrophysical Journal*, vol. 697, p. 1071–1102, May 2009.
- [131] C. Meegan, G. Lichti, P. N. Bhat, E. Bissaldi, M. S. Briggs, V. Connaughton, R. Diehl, G. Fishman, J. Greiner, A. S. Hoover, and et al., “Thefermigamma-ray burst monitor,” *The Astrophysical Journal*, vol. 702, p. 791–804, Aug 2009.
- [132] L. Lin, E. Göğüş, O. J. Roberts, M. G. Baring, C. Kouveliotou, Y. Kaneko, A. J. van der Horst, and G. Younes, “Fermi/gbm view of the 2019 and 2020 burst active episodes of sgr j1935+2154,” *The Astrophysical Journal*, vol. 902, p. L43, Oct 2020.